Macro Mars to Micro Mars:
Mapping Minerals and Magnetization

Thesis by

Jennifer Buz

In Partial Fulfillment of the Requirements for the degree of
Doctor of Philosophy

CALIFORNIA INSTITUTE OF TECHNOLOGY
Pasadena, California

2018
(Defended April 20, 2018)

Jennifer Buz
ORCID: 0000-0002-0491-2686

ACKNOWLEDGEMENTS

I would like to thank Bethany Ehlmann and Joe Kirschvink who have each been excellent mentors in their own way. Bethany, my primary advisor, couldn't have been a better role model. I am appreciative of the patience she has shown me, the encouragement she has given me, and the endless opportunities she has presented me with. Joe has been incredibly supportive, always optimistic, and a fountain of interesting projects and ideas. I would also like to thank the rest of the GPS faculty who have taught me so much in terms of book learning, creativity in pursuing projects, and persistence. In particular, I would like to thank Woody Fischer and Mike Lamb who served on my thesis advisory committee, John Grotzinger who I have had the privilege of collaborating with, and George Rossman who has always been helpful and excited.

I definitely could not have gone this far without my family being behind me every step of the way. My parents have made countless sacrifices for our education and their enthusiasm and curiosity has surely fueled our academic careers. I am also grateful to my brother who has bravely done everything before me and shown me the way so casually as to imply it's all so easy! My aunts, uncles, cousins, and grandparents have always been my biggest cheerleaders and I have been so lucky to have them nearby while I was at Caltech.

My friends in and out of GPS have absolutely kept me sane. Whether it was getting a coffee, a beer, or just hanging out, the friendly smiles and welcoming atmosphere all around has been an excellent way to decompress. I've been lucky to have childhood friends and roommates to talk about non-science things with. I was fortunate to have an entertaining and friendly pit, great officemate in Natalia, and helpful and supportive lab mates both in the Ehlmann and Kirschvink labs. I'm also grateful to my past class and lab mates at MIT who have kept in touch and offered support as I embarked on later adventures. In particular I would like to thank Ben Weiss who has always made himself available for scientific, life, or career advice.

The Caltech GPS department could not be such a productive and happy place if it were not for the excellent administrative staff. I have always been greeted kindly even when the paperwork surely seems insurmountable and I am extremely appreciative for that.

I will look back at my time as a PhD student at Caltech fondly and it is because of each person I have interacted with during this time, whether I mentioned you explicitly or not, Thank You!

ABSTRACT

Combination of remote sensing data with *in-situ* measurements provides a fuller understanding of Mars phenomena. This dissertation focuses on integrating macroscopic and microscopic scales of measurement with regard to spectroscopy and magnetization. In the first chapter high resolution orbital spectroscopy (~18 m/px) and imagery (~30 cm/px) are used to identify potential sources for some of the sedimentary rocks investigated by the Curiosity rover and expand the accessible stratigraphy. While we find mineralogies in common outside and inside the crater as well as transport mechanisms, we conclude that additional sedimentary sources and/or modification after transport are required to explain chemical differences and that strata point to multiple episodes of a lake in Gale crater. In the third chapter we conducted a laboratory photometric study on candidate calibration target materials for the Mars-2020 rover. We characterized these target materials for proper calibration and monitoring of the Mastcam-Z instrument to enable mineral identification through reflectance spectroscopy. The fourth and fifth chapters focus on the microscopic magnetizations found within Martian meteorite ALH84001. Chapter four reports on paleomagnetic experiments conducted on isolated carbonate crystals that contain magnetite previously reported to be biogenic. We compare paleomagnetic test results which distinguish between biogenic and abiogenic origin hypotheses and find that the magnetization within the carbonates is most consistent with a shock processes. In chapter five we analyzed the distribution of dipoles within slices of ALH84001 and determined that they lie in a girdle distribution that could be interpreted as resulting from a true polar wander event on Mars. Looking at kilometer scale observations outside of Gale enlightened observations made along the rover transverse path. A high-resolution laboratory analysis of calibration materials will enable future multispectral mineralogical explorations. Microscopic analyses of magnetization inform ancient surface processes on Mars and hint at large-scale global change. In each of these chapters our results were only made possible or greatly enhanced by the combination of data sources and scales.

PUBLISHED CONTENT AND CONTRIBUTIONS

Buz, J., B. L. Ehlmann, L. Pan, and J. P. Grotzinger (2017), Mineralogy and stratigraphy of the Gale crater rim, wall, and floor units, *J. Geophys. Res. Planets*, 122, 1090–1118, doi:10.1002/2016JE005163.

J.B. participated in the conception of the project and led the gathering of mineralogical data, mapping, interpretations, and the writing of the manuscript.

-Adapted for the contents of Chapter 2

TABLE OF CONTENTS

LIST OF ACRONYMS

AF. Alternating Field

ASD. Analytical Spectral Devices

ARM. Anhysteretic Remanent Magnetization

BRDF. Bidirectional Reflectance Distribution Function

CAT. CRISM Analysis Tool

CDR. Calibrated data record

CRISM. Compact Reconnaissance Imaging Spectrometer for Mars

CRM. Chemical Remanent Magnetization

CTX. Context Camera

DCS. Decorrelation Stretch

DEM. Digital Elevation Model

DRM. Detrital Remanent Magnetization

GKS. Gale-Knobel-Sharp

HiRISE. High Resolution Imaging Science Experiment

I/F. Radiance Factor

IRM. Isothermal Remanent Magnetization

MCZ. Mastcam-Z

MOLA. Mars Orbiter Laser Altimeter

MRO. Mars Reconnaissance Orbiter

MSL. Mars Science Laboratory

NRM. Natural Remanent Magnetization

PRM. Pressure Remanent Magnetization

REFF. Reflectance Factor

ROI. Region of Interest

SRM. Shock Remanent Magnetization

SWIR. Short-wave infrared

THEMIS. Thermal Emission Imaging System

TPW. True Polar Wander

TRM. Thermal Remanent Magnetization

VNIR. Visible/near-infrared

Chapter 1

INTRODUCTION

Initial telescopic observations of the surface of Mars showed us that the planet bears many similarities to Earth. Although the intelligently designed 'canals' that Percival Lowell identified [*Lowell*, 1906] did not prove true, the surface of Mars has many other familiar features such as volcanoes, ice caps, and erosionally modified landscapes. We now also know that ancient Mars was once even more Earth-like, hosting areas which were likely habitable [*Grotzinger et al.*, 2014] and having a global magnetic field [*Kirschvink et al.*, 1997; *Acuna et al.*, 1999]. Given Mars' neighborly position in our solar system and the clear comparisons that can be drawn between it and Earth, we look to Mars to learn about our own planet. However, because we are limited to observing Mars through telescopes, satellites, landers, and meteorite samples, it is often difficult to fully understand any given observation. It is necessary to combine data made through various methods in order to gain the fullest understanding.

Telescopic observations of Mars (both on Earth and in space) allow for measurements of phenomena that occur globally and over many years such as changes in the Martianatmosphere [e.g., *Mumma et al.*, 2009]. Satellite observations allow imaging of Mars from the kilometer to sub-meter scale and the inclusion of more specialized instruments such as spectrometers, magnetometers, and cameras (e.g., [*Acuna et al.*, 1998; *Malin et al.*, 2007; *Murchie et al.*, 2007]). Through satellites we have been able to assess the distribution of materials on the surface and have learned that Mars is a basaltic planet with many minerals in common with Earth [*Bibring et al.*, 2005; *Ehlmann and Edwards*, 2014]. We have also been able to map out geological features and landscapes and construct a chronology for surface evolution (e.g., [*Smith et al.*, 1999; *McEwen et al.*, 2007; *Fassett and Head*, 2008; *Tanaka et al.*, 2014]). Variations in the magnetization of the crust have enabled the discovery and characterization of a past core dynamo [*Acuna et al.*, 1998; *Acuna et al.*, 1999; *Connerney et al.*, 1999; *Stevenson*, 2001]. In-situ investigations through the use of landers and rovers have allowed us to see beneath the surface of Mars by direct excavation [e.g., *Arvidson et al.*, 2009], conduct micron scale chemical analyses of rocks and sediments [e.g., *Anderson et al.*, 2015], and determine lithologies we could not have seen from orbit, such as the presence of conglomerates [*Williams et al.*, 2013]. Furthermore, combination of local atmospheric observations [*Martínez et al.*, 2017] with global datasets [*Mumma et al.*, 2009] have shed light on trace gas and aerosol variability and Mars climate models [*Viscardy et al.*, 2016].

Mars sample return through planetary missions will come in the future, but for now we have a suite of Martian samples which has been delivered to us through impact processes: meteorites. Although these samples are not representative of the Martian crust and originate from unknown locations [*Mcsween*, 1994; *Agee et al.*, 2013] we have learned much through the ability to interrogate the samples in state-of-the art facilities on Earth. Isotopic measurements, for example, have enabled the determination of past surface conditions, including chemistry and temperatures [e.g., *Halevy et al.*, 2011]. We have also learned about the strength of a surface magnetic field, likely from a core dynamo [*Kirschvink et al.*, 1997; *Weiss et al.*, 2002].

While observations at each scale shed light on surface composition, atmosphere, geophysics, and landscape evolution on Mars, it is only through consideration of all of them at once that we can fully understand Mars' systems. Thus, the major questions driving this thesis are: (1) What further constraints can remote sensing observations place on in-situ observations (via a rover or hand sample)? (2) How do microscopic observations influence the interpretation of large-scale measurements? In this thesis I present a series of studies that combine information gained through satellite, in-situ, and hand sample measurements. The chapters are summarized below:

Chapter Summaries

Chapter 2

The Mars Science Laboratory (MSL) rover team is studying a sedimentary sequence of rocks on Mt. Sharp, within Gale crater [*Grotzinger et al.*, 2012]. Where these rocks and sediments came from is not fully understood from rover data alone. A major motivation for this study was the discovery of feldspathic and high-Si lithologies as float within Gale [*Sautter et al.*, 2014; *Morris et al.*, 2016], which is unexpected given the abundance of mafic minerals within the region [*Ehlmann and Buz*, 2015]. We used satellite data, both spectroscopy and high resolution imagery, in the greater Gale region to assess the mineralogical diversity and identify processes which may have delivered material to the vicinity of the rover. We found that the walls and rim of Gale crater host a similar mineralogy to that observed along some portions of the traverse, specifically we found a predominantly basaltic bedrock with variable Fe/Mg phyllosilicates. We also observe that though the general mineralogy of the phyllosilicates are the same in and out of Gale, there is the inclusion of Fe, Al phyllosilicates within some layers of Mt. Sharp [*Milliken et al.*, 2010]. We conclude that there is evidence both for transport of material from the Gale rim and wall and also for modification of these materials later. We did not find evidence for felsic material outside of Gale or in its wall rock through our methods; however, we are limited in detection capabilities because the inclusion of mafic minerals such as olivine and pyroxene can overwhelm any felsic signatures in the visible-near infrared. Furthermore, the thermal infrared instrument which is more sensitive to high-Si lithologies has a much larger spatial resolution, perhaps larger than any felsic outcrops, if they exist in the region.

Looking at the stratigraphy of the region from orbit, we identified multiple geologic units which have characteristics of lake sediments (e.g. fracturing, presence of phyllosilicates, layering). By mapping these out we are able to extend the potential lake sediment stratigraphy >250 m below the MSL traverse. Although the contact between the various lacustrine-interpreted units is not always well exposed, this finding points to several episodes of lake Gale that predate the MSL sediments in line with the hypothesis from examination of the levels of multiple delta/fan deposits that Gale may have hosted many lakes [*Palucis et al.*, 2016].

Chapter 3

Mars rovers have been able to identify mineralogies and lithologies through the use of multispectral imagers onboard which allow for discrimination of absorptions in the visible-near infrared wavelength range. These identifications are only possible after careful calibration of data acquired by the Mastcam-Z multispectral imager. In order to fulfill this requirement, the rovers carry a series of calibration targets, materials with known spectral properties that can be imaged by the rover to assess lighting conditions at the time of a scientific observation of surface materials and track the stability of the camera over time. To aid in the future identification of materials with the Mars-2020 rover, we characterized the photometric properties of the candidate calibration targets, 8 color and grey scale commercially available photometric standards. We characterized the spectral properties of each target material in the Mars-2020 relevant wavelength range and how those properties change with viewing geometry. We find that about half of the candidate targets are quasi-isotropic scatterers and the rest are forward-scattering. The targets are increasingly isotropic at longer wavelengths. All have scattering properties that are characterizable and quantifiable. For the calibration purposes of the Mastcam-Z instrument for which they were designed, these calibration materials will be suitable standards for correction of Mars data. Furthermore, they may be of use to other imagers and spectrometers on board the rover.

Chapter 4

Martian meteorite ALH84001 has been well-studied because of the diversity it brought to the Martian meteorite suite through its novel mineralogy and ~4.1 Ga age. However, many of the studies of ALH84001 have focused on what has been interpreted by some as a Martian biosignature: magnetite crystals within carbonate globules which bear striking resemblance to those formed by magnetotactic bacteria on Earth [e.g., *McKay et al.*, 1996; *Thomas-Keprta et al.*, 2000]. The leading abiogenic hypothesis involves the formation of these magnetite crystals through chemical alteration (through heating or a shock process) of the carbonate which hosts them [*Treiman and Essene*, 2011]. These two contradictory formation scenarios can be classified as detrital (i.e., the magnetite formed biogenically and then was deposited or entrained) or chemical (i.e., the magnetite formed in-situ). Paleomagnetics can be used to distinguish between these scenarios in terrestrial samples. These tests could not be conducted on ALH84001 previously because of the microscopic size of the samples. Our study utilized a high-resolution scanning magnetic microscope to apply these tests.

Fuller's test of Natural Remanent Magnetization [*Fuller et al.*, 1988] measures the efficiency of a magnetization process. In a detrital scenario, where magnetic particles are subject to oscillations in an aqueous medium, the magnetization will be less efficient than in a chemical scenario where the particles are able to grow and align with an external magnetic field without external forcing. We found that the magnetization of the carbonates was consistent with a high-efficiency process. This test is calibrated for an Earth-strength field (which is consistent with previous estimates of Mars' field strength [*Kirschvink et al.*, 1997; *Stevenson*, 2001; *Weiss et al.*, 2008]). The anhysteretic remanent magnetization acquisition test [*Cisowski*, 1981] probes the inter-particle interactions within a sample. In a detrital scenario, magnetic particles will be strongly interacting because they naturally clump together whereas in a chemical scenario the particles are formed evenly distributed throughout the protolith and therefore are less interacting. We find that the ALH84001 carbonates are highly interacting. However, to calibrate this test we also measured natural carbonate samples of various states of alteration and found that highly altered carbonates also demonstrate highly-interacting behavior. Lastly, we applied the Lowrie-Fuller Test [*Newell*, 2000] which both distinguishes between single-domain (consistent with biogenic origin) and multi-domain magnetite and allows for comparison between demagnetization of the original remanence with that of laboratory fields. We found that the magnetite within the ALH84001 carbonate is predominantly single-domain; however, we also found that the remanence in the ALH84001 carbonates is mostly carried by low coercivity grains, which is most similar to magnetization via a shock process.

The various tests applied to this sample give additional support for an abiogenic origin for the ALH84001 magnetite. A shock origin for the remanence in the ALH84001 carbonates is most consistent with the cumulative data. However, none of these tests have been able to rule out a biogenic origin. More complicated scenarios exist which may allow for a biogenic origin such as the magnetite may be formed biogenically, deposited, and then shocked.

Chapter 5

Magnetization found within two pyroxene grains in ALH84001 was the first evidence for an ancient core dynamo on Mars [*Kirschvink et al.*, 1997], and was subsequently confirmed by data from orbiting magnetometers [*Acuna et al.*, 1998]. A later study using magnetic microscopy found that a heterogeneous magnetization exists within the sample and that magnetization is carried within multiple mineralogies [*Weiss et al.*, 2008]. We were interested in the distribution of dipole directions found within ALH84001 and what these might mean for the ancient core dynamo on Mars. We find that the magnetization direction distribution throughout the bulk rock can be described with a girdle distribution. Given the thermal history of ALH84001, which includes multiple shock events and recrystallization, the rock may have preserved magnetization at several points in its past. One interpretation for this distribution of dipoles is that ALH84001 records true polar wander (TPW), i.e., that the Martian dynamo shifted with respect to the surface of Mars as the magnetization was recorded. Due to the nature of the measurements on the bulk sample, where individual dipoles can be difficult to isolate due to their proximity to other dipoles, the error associated with the dipole fitting is significant. Although a TPW scenario is a possible explanation of the data, this dataset does not conclusively prove TPW. Previous, geophysical studies have also concluded that TPW likely happened on Mars [e.g., *Sprenke et al.*, 2005; *Perron et al.*, 2007].

A key aspect of each of the studies was the necessity to expand the observation range. In the case of MSL, our identification of potential protolith material for the Gale floor phyllosilicates came from looking outside of Gale. We were also able to place constraints on the size of potential, yet-unseen, source regions for silica-rich sediments and K-feldspar-enriched sediments measured by the rover by our lack of their detection. Most importantly, the orbital scale permitted identification of older episodes of Gale lake than accessible to the MSL rover. For Mars-2020, our high resolution spectroscopic laboratory characterization of the calibration targets will be necessary for mineralogical and textural characterizations by the Mastcam-Z instrument on the rover. When studying the microscopic magnetization in ALH84001 carbonates and applying paleomagnetic tests that were calibrated for Earth's magnetic field we needed to incorporate previous geophysical modeling on the field strength of Mars to interpret and validate our results. Similarly, a TPW origin for the magnetization in the bulk of ALH84001 is made more compelling by the geophysical modeling done using satellite data showing that TPW was likely to have occurred on Mars.

References

Acuna, M. H., et al. (1999), Global distribution of crustal magnetization discovered by the mars global surveyor MAG/ER experiment, *Science*, *284*, 790-793, doi:10.1126/science.284.5415.790.

Acuna, M. H., et al. (1998), Magnetic field and plasma observations at Mars: Initial results of the Mars global surveyor mission, *Science*, *279*, 1676-1680, doi:10.1126/science.279.5357.1676.

Agee, C. B., et al. (2013), Unique meteorite from early Amazonian Mars: water-rich basaltic breccia Northwest Africa 7034, *Science*, *339*, 780-785, doi:10.1126/science.1228858.

Anderson, R., et al. (2015), ChemCam results from the Shaler outcrop in Gale crater, Mars, *Icarus*, *249*, 2-21, doi:10.1016/j.icarus.2014.07.025.

Arvidson, R. E., et al. (2009), Results from the Mars Phoenix Lander Robotic Arm experiment, *J Geophys Res-Planet*, *114*, doi:Artn E00e02
10.1029/2009je003408.

Bibring, J. P., et al. (2005), Mars surface diversity as revealed by the OMEGA/Mars Express observations, *Science*, *307*, 1576-1581, doi:10.1126/science.1108806.

Cisowski, S. (1981), Interacting Vs Non-Interacting Single Domain Behavior in Natural and Synthetic Samples, *Phys. Earth Planet. Inter.*, *26*, 56-62, doi:10.1016/0031-9201(81)90097-2.

Connerney, J. E., M. H. Acuna, P. J. Wasilewski, N. F. Ness, H. Reme, C. Mazelle, D. Vignes, R. P. Lin, D. L. Mitchell, and P. A. Cloutier (1999), Magnetic lineations in the ancient crust of mars, *Science*, *284*, 794-798, doi:10.1126/science.284.5415.794.

Ehlmann, B. L., and J. Buz (2015), Mineralogy and fluvial history of the watersheds of Gale, Knobel, and Sharp craters: A regional context for the Mars Science Laboratory Curiosity's exploration, *Geophys. Res. Lett.*, *42*, 264-273, doi:10.1002/2014gl062553.

Ehlmann, B. L., and C. S. Edwards (2014), Mineralogy of the Martian Surface, *Annu Rev Earth Pl Sc*, *42*, 291-315, doi:10.1146/annurev-earth-060313-055024.

Fassett, C. I., and J. W. Head (2008), The timing of martian valley network activity: Constraints from buffered crater counting, *Icarus*, *195*, 61-89, doi:10.1016/j.icarus.2007.12.009.

Fuller, M., S. Cisowski, M. Hart, R. Haston, E. Schmidtke, and R. Jarrard (1988), Nrm-Irm(S) Demagnetization Plots - an Aid to the Interpretation of Natural Remanent Magnetization, *Geophys. Res. Lett.*, *15*, 518-521, doi:10.1029/GL015i005p00518.

Grotzinger, J. P., et al. (2012), Mars Science Laboratory Mission and Science Investigation, *Space Sci. Rev.*, *170*, 5-56, doi:10.1007/s11214-012-9892-2.

Grotzinger, J. P., et al. (2014), A habitable fluvio-lacustrine environment at Yellowknife Bay, Gale crater, Mars, *Science*, *343*, 1242777, doi:10.1126/science.1242777.

Halevy, I., W. W. Fischer, and J. M. Eiler (2011), Carbonates in the martian meteorite Allan Hills 84001 formed at 18±4 C in a near-surface aqueous environment, *Proc. Natl. Acad. Sci*, *108*, 16895-16899.

Kirschvink, J. L., A. T. Maine, and H. Vali (1997), Paleomagnetic evidence of a low-temperature origin of carbonate in the Martian meteorite ALH84001, *Science*, *275*, 1629-1633, doi:10.1126/science.275.5306.1629.

Lowell, P. (1906), *Mars and its Canals*, The Macmillan company; London: Macmillan & co., ltd.

Malin, M. C., et al. (2007), Context Camera Investigation on board the Mars Reconnaissance Orbiter, *J Geophys Res-Planet*, *112*, doi:Artn E05s04
10.1029/2006je002808.

Martínez, G. M., et al. (2017), The Modern Near-Surface Martian Climate: A Review of In-situ Meteorological Data from Viking to Curiosity, *Space Sci. Rev.*, *212*, 295-338, doi:10.1007/s11214-017-0360-x.

McEwen, A. S., et al. (2007), A closer look at water-related geologic activity on Mars, *Science*, *317*, 1706-1709, doi:10.1126/science.1143987.

McKay, D. S., E. K. Gibson, Jr., K. L. Thomas-Keprta, H. Vali, C. S. Romanek, S. J. Clemett, X. D. Chillier, C. R. Maechling, and R. N. Zare (1996), Search for past life on Mars: possible relic biogenic activity in martian meteorite ALH84001, *Science*, *273*, 924-930, doi:10.1126/science.273.5277.924.

Mcsween, H. Y. (1994), What We Have Learned About Mars from Snc Meteorites, *Meteoritics*, *29*, 757-779, doi:10.1111/j.1945-5100.1994.tb01092.x.

Milliken, R. E., J. P. Grotzinger, and B. J. Thomson (2010), Paleoclimate of Mars as captured by the stratigraphic record in Gale Crater, *Geophys. Res. Lett.*, *37*, doi:Artn L04201
10.1029/2009gl041870.

Morris, R. V., et al. (2016), Silicic volcanism on Mars evidenced by tridymite in high-SiO₂ sedimentary rock at Gale crater, *Proc. Natl. Acad. Sci*, *113*, 7071-7076, doi:10.1073/pnas.1607098113.

Mumma, M. J., G. L. Villanueva, R. E. Novak, T. Hewagama, B. P. Bonev, M. A. Disanti, A. M. Mandell, and M. D. Smith (2009), Strong release of methane on Mars in northern summer 2003, *Science*, *323*, 1041-1045, doi:10.1126/science.1165243.

Murchie, S., et al. (2007), Compact reconnaissance Imaging Spectrometer for Mars (CRISM) on Mars Reconnaissance Orbiter (MRO), *J Geophys Res-Planet*, *112*, E05S03, doi:Artn E05s03
10.1029/2006je002682.

Newell, A. J. (2000), The Lowrie–Fuller test: single-domain and micromagnetic theory, *Earth Planet. Sci. Lett.*, *183*, 335-346.

Palucis, M. C., W. E. Dietrich, R. M. E. Williams, A. G. Hayes, T. Parker, D. Y. Sumner, N. Mangold, K. Lewis, and H. Newsom (2016), Sequence and relative timing of large lakes in Gale crater (Mars) after the formation of Mount Sharp, *J Geophys Res-Planet*, *121*, 472-496, doi:10.1002/2015je004905.

Perron, J. T., J. X. Mitrovica, M. Manga, I. Matsuyama, and M. A. Richards (2007), Evidence for an ancient martian ocean in the topography of deformed shorelines, *Nature*, *447*, 840-843, doi:10.1038/nature05873.

Sautter, V., et al. (2014), Igneous mineralogy at Bradbury Rise: The first ChemCam campaign at Gale crater, *J Geophys Res-Planet*, *119*, 30-46, doi:10.1002/2013je004472.

Smith, D. E., et al. (1999), The global topography of Mars and implications for surface evolution, *Science*, *284*, 1495-1503, doi:10.1126/science.284.5419.1495.

Sprenke, K. F., L. L. Baker, and A. F. Williams (2005), Polar wander on Mars: Evidence in the geoid, *Icarus*, *174*, 486-489, doi:10.1016/j.icarus.2004.11.009.

Stevenson, D. J. (2001), Mars' core and magnetism, *Nature*, *412*, 214-219, doi:10.1038/35084155.

Tanaka, K. L., S. J. Robbins, C. M. Fortezzo, J. A. Skinner, and T. M. Hare (2014), The digital global geologic map of Mars: Chronostratigraphic ages, topographic and crater morphologic characteristics, and updated resurfacing history, *Planetary and Space Science*, *95*, 11-24, doi:10.1016/j.pss.2013.03.006.

Thomas-Keprta, K. L., D. A. Bazylinski, J. L. Kirschvink, S. J. Clemett, D. S. McKay, S. J. Wentworth, H. Vali, E. K. Gibson, Jr., and C. S. Romanek (2000), Elongated prismatic magnetite crystals in ALH84001 carbonate globules: potential Martian magnetofossils, *Geochim Cosmochim Acta*, *64*, 4049-4081.

Treiman, A. H., and E. J. Essene (2011), Chemical composition of magnetite in Martian meteorite ALH 84001: Revised appraisal from thermochemistry of phases in Fe-Mg-C-O, *Geochim. Cosmochim. Acta*, *75*, 5324-5335, doi:10.1016/j.gca.2011.06.038.

Viscardy, S., F. Daerden, and L. Neary (2016), Formation of layers of methane in the atmosphere of Mars after surface release, *Geophys. Res. Lett.*, *43*, 1868-1875, doi:10.1002/2015gl067443.

Weiss, B. P., L. E. Fong, H. Vali, E. A. Lima, and F. J. Baudenbacher (2008), Paleointensity of the ancient Martian magnetic field, *Geophys. Res. Lett.*, *35*, doi:Artn L23207
10.1029/2008gl035585.

Weiss, B. P., D. L. Shuster, and S. T. Stewart (2002), Temperatures on Mars from 40Ar/39Ar thermochronology of ALH84001, *Earth Planet. Sci. Lett.*, *201*, 465-472, doi:10.1016/s0012-821x(02)00729-x.

Williams, R. M., et al. (2013), Martian fluvial conglomerates at Gale crater, *Science*, *340*, 1068-1072, doi:10.1126/science.1237317.

Chapter 2

MINERALOGY AND STRATIGRAPHY OF THE GALE CRATER RIM, WALL, AND FLOOR UNITS

Buz, J., B. L. Ehlmann, L. Pan, and J. P. Grotzinger (2017), Mineralogy and stratigraphy of the Gale crater rim, wall, and floor units, *J. Geophys. Res. Planets, 122*, 1090–1118, doi:10.1002/2016JE005163.

Abstract

The Curiosity rover has detected diverse lithologies in float rocks and sedimentary units on the Gale crater floor, interpreted to have been transported from the rim. To understand their provenance, we examine the mineralogy and geology of Gale's rim, walls, and floor, using high resolution imagery and infrared spectra. While no significant differences in bedrock spectral properties were observed within most THEMIS and CRISM scenes, some CRISM scenes of rim and wall rocks showed olivine-bearing bedrock accompanied by Fe/Mg phyllosilicates. Hydrated materials with 2.48-µm absorptions in Gale's eastern walls are spectrally similar to the sulfate unit in Mt. Sharp (Aeolis Mons). Sedimentary strata on the Gale floor southwest of the landing site, likely coeval with the Bradbury units explored by Curiosity, also are hydrated and/or have Fe/Mg phyllosilicates. Spectral properties of these phyllosilicates differ from the Al-substituted nontronite detected by CRISM in Mt. Sharp, suggesting formation by fluids of different composition. Geologic mapping of the crater floor shows the hydrated or hydroxylated materials are typically overlain by spectrally undistinctive, erosionally-resistant, cliff-forming units. Additionally, a 4-km impact crater exposes >250 m of the Gale floor, including finely layered units. No basement rocks are exposed, thus indicating sedimentary deposits ≥250 m beneath strata studied by Curiosity. Collectively, the data indicate substantial sedimentary infill of Gale crater, including some materials derived from the crater rim. Lowermost thin layers are consistent with deposition in a lacustrine environment; interbedded hydrated/hydroxylated units may signify changing environmental conditions, perhaps in a drying or episodically dry lake bed.

1.0 Introduction

The Mars Science Laboratory (MSL) was sent to Gale crater with a goal of assessing past habitability in the region. Gale crater was selected primarily because of a large interior central mound, Aeolis Mons, informally known as Mt. Sharp, made of roughly flat-lying strata which may preserve evidence for sequential changes in the Martian environment [*Grotzinger et al.*, 2012]. Previous remote sensing studies of Gale crater have focused on the formation of Mt. Sharp by exploring its geomorphology, thermophysical properties, and mineralogy [*Malin and Edgett*, 2000; *Pelkey and Jakosky*, 2002; *Pelkey et al.*, 2004; *Rogers and Bandfield*, 2009; *Anderson and Bell*, 2010; *Milliken et al.*, 2010; *Thomson et al.*, 2011; *Grotzinger et al.*, 2012; *Fraeman et al.*, 2013; *Kite et al.*, 2013a; *Kite et al.*, 2013b; *Le Deit et al.*, 2013; *Wray*, 2013; *Milliken et al.*, 2014; *Fraeman et al.*, 2016]. In these works, a wide range of hypotheses have been proposed to explain the Mt. Sharp sedimentary rocks, including formation by deposition in a lacustrine environment, aeolian deposition, fluvial deposition, ice-mediated air fall deposition, ash fall, or some combination of these processes. Curiosity rover data so far support only fluvial, deltaic, lacustrine, and aeolian modes of deposition for basal Mt. Sharp strata of the Bradbury group, interfingering Murray formation, and unconformably overlying Stimson formation [*Grotzinger et al.*, 2014; *Grotzinger et al.*, 2015; *Banham et al.*, 2016]. During the first four years of its mission, Curiosity traversed the northern Gale floor deposits of the Bradbury group and subsequently began its ascent through strata of the underlying Mt. Sharp group [*Grotzinger et al.*, 2014; *Grotzinger et al.*, 2015]. Measurements taken by MSL have thus far shown that the float rocks and strata present on the floor of Gale crater host an unexpectedly wide range of lithologic compositions, including clasts of alkaline basalt and felsic igneous float rocks in strata of the Bradbury group, basaltic mudstones with Fe/Mg phyllosilicates at Yellowknife Bay, and K-feldspar-enriched sandstone at the Kimberley [*Bish et al.*, 2013; *Blake et al.*, 2013; *Stolper et al.*, 2013; *McLennan et al.*, 2014; *Sautter et al.*, 2014; *Schmidt et al.*, 2014; *Vaniman et al.*, 2014; *Treiman et al.*, 2016]. A key question centers around the source of this lithologic diversity: is it related to the bedrock of the Gale crater walls and surrounding watershed? A product of sediment sorting and chemical alteration within the crater? Or sourced from ash fall or another unknown regionally widespread geologic process?

This study builds on previous work within and around Gale crater, focusing on the wall, rim, and floor units of Gale crater. The goal is to elucidate the relationships between the bedrock materials of the wall, rim, and floor with sedimentary units traversed over and analyzed by the MSL Curiosity rover. We seek to determine the provenance for some of the unique mineralogical detections made by MSL, the relative order in which materials were deposited in Gale crater, and how they might have been altered since or during transport, as recorded in the sedimentary rocks on the floor as seen from orbit. We first provide some background on the geology, mineralogy, and chemistry of the study region. We then describe previously and newly reported detections of minerals within the Gale rim, wall, and floor rock; report the results of geologic mapping of floor units extending from the rim to the Murray formation; and summarize the observed stratigraphy of sedimentary fill in Gale crater with a focus on how the observed mineralogy and morphology of units results from changes in the paleoenvironment. Finally, we describe the implications for the source rocks and how they might have changed during transport, deposition, and as part of a changing environment within Gale, as told by the mineralogy.

2.0 Geologic context

Gale is a ~150-km diameter impact crater situated along the Martian crustal dichotomy boundary. Current age estimates for the formation of Gale based on crater counting converge around 3.6-3.8 Ga, the late Noachian-Hesperian boundary [*Cabrol et al.*, 1999; *Thomson et al.*, 2011;

Le Deit et al., 2013]. Reconstruction of the bedrock stratigraphy and dating by crater counting places the formation age of Mt. Sharp soon after formation of the crater [*Thomson et al.*, 2011; *Grant et al.*, 2014; *Palucis et al.*, 2016]. High resolution imagery and spectroscopic data in the last decade have allowed further characterization of the Mt. Sharp group, which comprise the lowermost exposed units of Mt. Sharp [*Grotzinger et al.*, 2015]. Orbital observations of this interval of strata reveal iron smectite clays, iron oxides, silica, and strong hydration signatures with distinctive strata bearing mono- and polyhydrated sulfates [*Pelkey et al.*, 2004; *Milliken et al.*, 2010; *Thomson et al.*, 2011; *Fraeman et al.*, 2013; *Le Deit et al.*, 2013; *Fraeman et al.*, 2016]. Additionally, numerous valleys and canyons have been identified that incise the Mt. Sharp group strata [e.g., *Anderson and Bell*, 2010; *Milliken et al.*, 2014; *Palucis et al.*, 2016]. The presence of hydrated minerals decreases while dust cover increases with elevation on the mound [*Pelkey et al.*, 2004; *Le Deit et al.*, 2013]. Nevertheless, boxwork structures indicating subsurface fluid flow and diagenesis are found at higher elevations [*Siebach and Grotzinger*, 2014], just beneath the unconformity that marks the top of the Mt. Sharp group [*Grotzinger et al.*, 2015].

Measurements taken by MSL thus far have revealed diverse chemistry and mineralogy of float rocks and exposed bedrock in the Bradbury group, the stratigraphically oldest unit explored by Curiosity [*Bish et al.*, 2013; *Blake et al.*, 2013; *Stolper et al.*, 2013; *Sautter et al.*, 2014; *Schmidt et al.*, 2014; *Thompson et al.*, 2015; *Treiman et al.*, 2016]. The Bradbury group includes alluvial fan facies and inferred sediment transport directions that indicate derivation from the northern crater wall and rim [*Williams et al.*, 2013; *Grotzinger et al.*, 2014; *Grotzinger et al.*, 2015; *Szabo et al.*, 2015]. Some of float rocks and conglomerate clasts have high alkalinity and/or abundant feldspars [*Stolper et al.*, 2013; *Sautter et al.*, 2014], which have not been observed from orbit. Additionally, there is high chemical variability locally within the Bradbury, such as between the Sheepbed mudstone and the Gillespie sandstone members of the Yellowknife Bay formation, which both also differ from the Bradbury rise rocks, just ~400 m away [*McLennan et al.*, 2014; *Vaniman et al.*, 2014]. The Sheepbed and Gillespie bulk chemistry is subalkaline basaltic, and they did not have the high feldspar composition of some Bradbury rise rocks [*McLennan et al.*, 2014]. The Kimberley formation, which represents the middle part of the Bradbury group, is highly potassic, containing approximately 21% alkali feldspar by volume [*Treiman et al.*, 2016]. It is hypothesized that the Kimberley formation results from the transport and mixing of sediments from two or three distinct igneous sources, perhaps from the northern Gale rim [*Treiman et al.*, 2016; *Siebach et al.*, 2017]. The overall diversity within the Bradbury group and the inferred diversity of its source rocks was surprising, given that orbital data of units near Gale crater showed broadly similar basaltic compositions to those near the Gusev landing site in thermal infrared and gamma ray spectrometer data [*Rogers and Christensen*, 2007; *Taylor et al.*, 2010].

The regional mineralogy and chronology have been studied for the greater Gale watershed. Gale crater is at the northeast terminal extent of the Gale-Knobel-Sharp (GKS) watershed system which initiates north of Herschel crater [*Ehlmann and Buz*, 2015]. Large scale fluvial activity last occurred in the late Noachian/early Hesperian [*Irwin et al.*, 2005; *Fassett and Head*, 2008], and subsequently became increasingly more localized in the late Hesperian/early Amazonian [*Grant et al.*, 2014; *Ehlmann and Buz*, 2015]. It is possible that erosion during this and subsequent times resulted in material being transported into Gale crater relatively long distances, contributing basin filling sediments [*Ehlmann and Buz*, 2015; *Palucis et al.*, 2016]. Key results from study of the mineralogy with high-resolution visible/shortwave infrared data included widespread detections of olivine (sometimes with pyroxene) in the bedrock; hydrated silicates present in both bedrock and sediments; and regional or temporal differences in water chemistry as evidenced by the presence of chloride salts in the Sharp-Knobel watershed system but sulfate salts found by the rover in Gale crater [*Vaniman et al.*, 2014; *Ehlmann and Buz*, 2015]. Fe/Mg phyllosilicates, kaolin-family minerals, hydrated silica, and other hydrated/hydroxylated phases were detected regionally in a variety of locations including fluvial valley walls and crater rims and floors [*Wray*, 2013; *Carter et al.*, 2015; *Ehlmann and Buz*, 2015]. What is not clear is whether some of the materials that may have contributed to the accumulation of Mt. Sharp strata were derived from long-distances in the GKS watershed vs. locally within the immediate surroundings of Gale crater, including from the northern rim, the presumed source for much of the Bradbury group. We thus use remote sensing data to examine in greater detail the Gale crater basement rocks and northwestern floor rocks near the MSL landing site.

3.0 Methods

3.1 Mineralogy

Because we are interested in the basement bedrock and overlying floor deposits of Gale, we focused our data analysis on scenes along the Gale rim, wall, and floor, including scenes where erosion or small craters have exposed the stratigraphy of floor units. We did not analyze data over Mt. Sharp as prior works have described its mineralogy [e.g., Milliken et al., 2010; Fraeman et al., 2016]. Full and half resolution targeted images from the Compact Reconnaissance Imaging Spectrometer for Mars (CRISM) onboard the Mars Reconnaissance Orbiter (MRO) were examined. CRISM is a push-broom imaging spectrometer which acquires data between 0.36-3.92 μm sampled at ~6.55 nm/channel [*Murchie et al.*, 2007]. At highest spatial resolution CRISM is capable of resolving 15-19 m/pixel. The wavelength range and spectral resolution of CRISM allow for detection of many minerals via diagnostic absorptions including those related to electronic transitions in iron and vibrations associated with H_2O, CO_3, and metal-OH bonds [e.g., Clark et al. [1990]]. In total, 34 targeted images along the rim, wall, and floor of Gale crater were analyzed in this study (Figure 1). Reduced spatial and spectral resolution “mapping” products are also available from CRISM. These were used in regions where targeted CRISM scenes were not available; however, due to their lower spectral and spatial resolution and the relatively small exposures of non-dusted-covered bedrock, no additional mineral identifications were found using the mapping products.

Standard data processing procedures were applied to the CRISM spectral cubes to calibrate and atmospherically and photometrically correct the data. These procedures include a simple *cos i* photometric correction, which assumes isotropic surface scattering, and division by a scaled atmospheric transmission spectrum, derived from a volcano-scan image through the CRISM Analysis Tool (CAT) toolbox [*Morgan et al.*, 2009]. Because many of the CRISM scenes in this region are dusty and/or noisy [*Kreisch et al.*, 2015] (see Murchie et al. [2009] for a review of noise sources for the CRISM detectors), a denoise algorithm was developed to further aid in mineral identification [*Pan et al.*, 2015]. This algorithm excludes noisy pixels and bad spectral channels in a given image, identifies the pixels below a threshold value for several spectral parameters, and then creates "bland" spectra for use as a spectral denominator by using a column-based median of the identified bland pixels. After computing scene-derived denominator spectra for each column, the algorithm calculates the ratio spectrum of each pixel in the scene, thereby accentuating all the possible mineral detections relative to the spectrally bland regions in the same image. By ratioing a region of interest to a spectrally bland region from the same detector columns, we remove column-dependent detector artifacts and spectral signatures from materials found in common between the two areas, so the mineral signatures and spectral differences within the region of interest become more pronounced. Those spectra with possible mineral detections are then compared with the original spectra from the non-noise corrected, unratioed data cube for validation. Additionally, after spectra of interest were acquired, absorption positions were determined using the calibrated data record (CDR) wavelengths of the center pixel of each region of interest so as to properly account for the spectral smile of the CRISM instrument [*Murchie et al.*, 2009]. Many unit identifications were also made through the aid of standard spectral parameter maps [*Pelkey et al.*, 2007; *Wiseman et al.*, 2010; *Viviano-Beck et al.*, 2014].

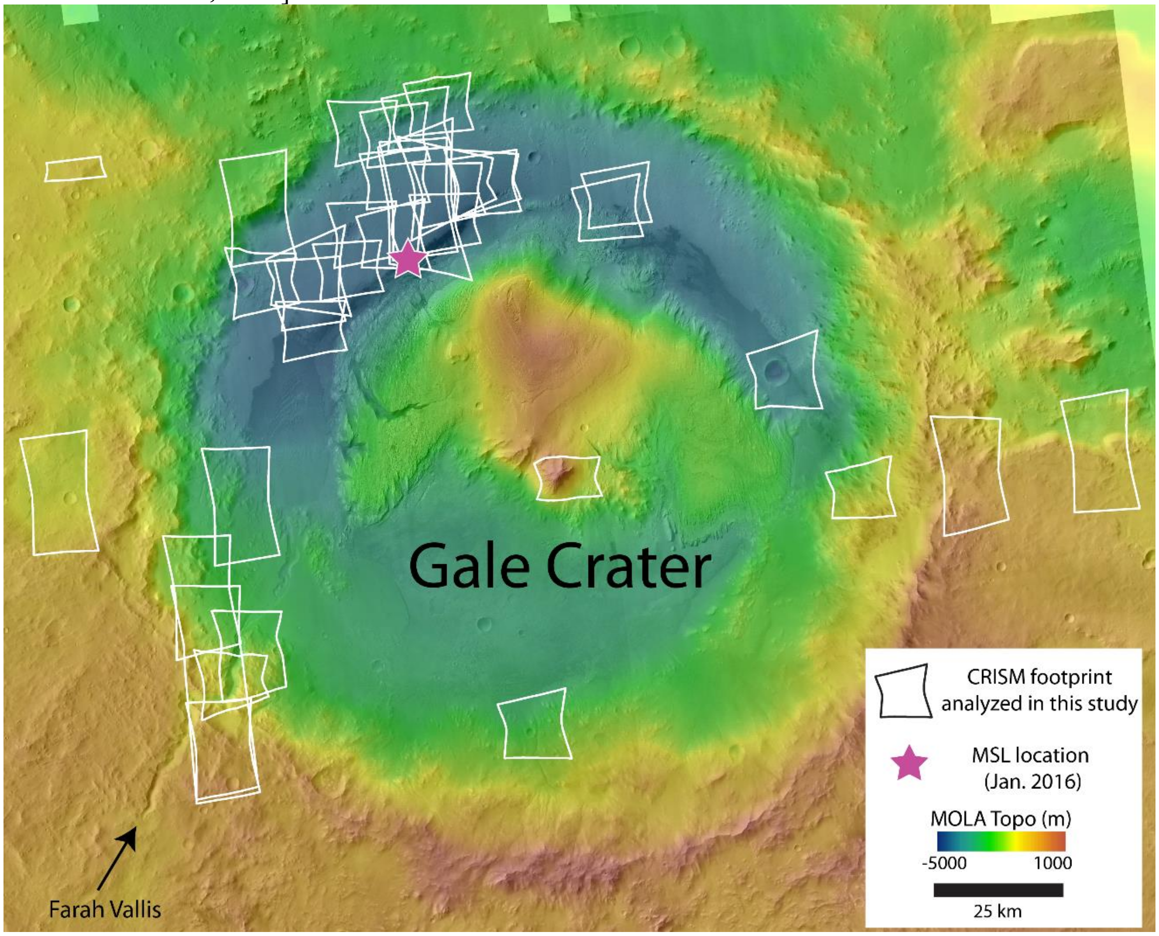

Figure 1: CRISM images analyzed in this study on a CTX mosaic with MOLA topography overlain. There is continuous CRISM coverage over the MSL landing site and traverse regions, but CRISM coverage over the remainder of Gale crater is sparser. Our study focused on all full- and half-resolution, long-wavelength CRISM scenes acquired over the walls, floor, central peak, and smaller craters within Gale (white outlines), which have the potential to reveal mineralogy of the bedrock and floor units. Those where discrete minerals were identified, enhanced above the basaltic background, are shown in Figure 2.

Data from the Thermal Emission Imaging System (THEMIS) instrument on the Mars Odyssey orbiter were also used to examine the composition of the Gale rim. THEMIS contains eight detectors within the 6.8 to 13.6 μm region and captures images at a spatial resolution of approximately 100 m/pixel [*Christensen et al.*, 2004]. CRISM is not capable of distinguishing iron-free high-Si silicates because the characteristic vibrations from the SiO_2 molecule occur at longer wavelengths than those sensed. In contrast, the THEMIS band passes are suited for the examination of the Si-O stretch spectral region, permitting distinctions of mafic and felsic lithologies and variability in constituent materials within these. In order to contrast and identify regions with different silicate compositions, which may be particularly mafic or felsic, we computed decorrelation stretches (DCS) using THEMIS data following Christensen [2005]. DCS enhances color separation and helps identify specific geologic units which appear as different colors correlated with different surface properties in the DCS product. A DCS stretch with THEMIS Bands 8, 7, and 5 (R, G, B, respectively) aids in discrimination of Thermal Emission Spectrometer Type 1 and 2 surfaces [*Bandfield et al.*, 2000] and has been used to identify mafic materials which appear pink/magenta [e.g., *Rogers et al.*, 2005; *Rogers and Fergason*, 2011] and chloride-bearing materials which appear blue [e.g., *Osterloo et al.*, 2010]. DCS stretch 6/4/2 can highlight regions containing high bulk silica [*Bandfield et al.*, 2013] in magenta colors and can also indicate differences in surface roughness and gray body emissivity [*Bandfield*, 2009].

3.2 Stratigraphy and geologic mapping

Following the identification of mineralogical/compositional units, we examined the morphology of exposures and mapped the distinct compositions identified to surface morphology, delineated using high resolution image data. For mapping and stratigraphic studies we used imagery from the Context Camera (CTX) [*Malin et al.*, 2007] and High Resolution Imaging Science Experiment (HiRISE) [*McEwen et al.*, 2007] instruments, both on MRO. We constructed a full coverage CTX mosaic over the Gale region, using images acquired in greyscale visible at a resolution of ~6 m/pixel and in swaths ~30-km wide. At select locations, HiRISE data were available with a resolution ~30 cm/pixel in ~6-km wide long swaths. We also incorporated topographic data from the Mars Orbiter Laser Altimeter (MOLA) instrument and CTX and HiRISE stereo pairs, including red-blue anaglyphs and processed digital elevation models (DEMs), either made as part of this study (using the Ames stereo pipeline) or available as HiRISE team products. We traced unit boundaries where differences in color, albedo, morphology, and texture were apparent. For example, dark, cliff forming units with high crater retention were separated from light-toned hummocky units with few craters. We were sometimes also able to distinguish geologic units based on differences in mineralogy seen with CRISM observations, e.g., phyllosilicate-bearing units versus spectrally bland units.

4.0 Results

In the subsequent section, we describe the minerals detected on the rim, wall and floor of Gale with CRISM and THEMIS (Section 4.1). Section 4.2 gives the context for each detection including the location and material type for each unit (e.g., crater ejecta, bedrock, valley wall). Section 4.3 details the results of geologic mapping, describing the discrete units on the NW crater floor (near the MSL rover) and the stratigraphy determined from topographic data and via direct observations of layering observed in a crater on the Gale floor.

4.1 Mineral detections

4.1.1 CRISM

Near-continuous dust cover of greater than ~100-μm thickness can obscure the composition of the underlying surface lithology as sensed in visible/infrared data. As observed in prior CRISM analyses, Gale crater is very dusty [*Poulet et al.*, 2014]; and, therefore, it is not surprising that mineral detections were only made in 10 of the 34 analyzed CRISM scenes (Figure 2). The minerals were identified in a variety of geologic contexts including as parts of crater ejecta, on valley and crater walls, on ridges, in mass wasting deposits, and beneath cliff-forming units. In common in all of the scenes where minerals were identified, the spectral signatures were mostly present in darker or topographically rougher areas, which are presumably less covered by dust due to recent excavation or high erosion rates.

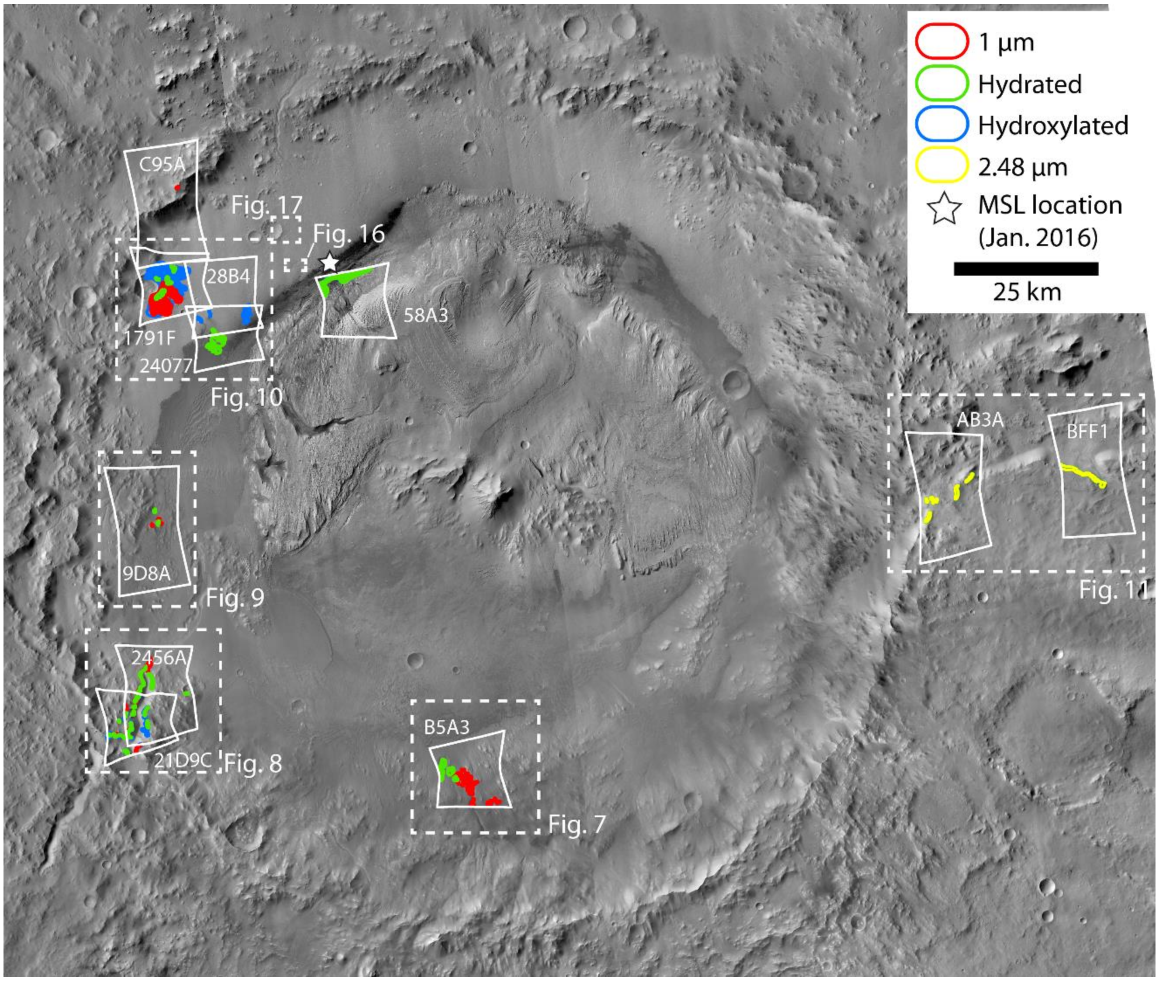

Figure 2: Mafic and hydrated/hydroxylated minerals discovered on the walls and floor of Gale crater. Regions where absorption features are detected in CRISM images are outlined atop the CTX mosaic. Although CRISM coverage of Gale is extensive (Figure 1), the outlined scenes are the only scenes in which mineral absorptions were found above background. Olivine is indicated by an absorption centered near 1 µm. Other minerals range in hydration state, some only exhibiting an H2O- absorption at 1.9 µm (hydrated, green), others exhibiting metal-OH vibrational features at 2.3 and/or 1.4 µm (hydroxylated, blue), and some showing all three absorptions. Hydrated materials with a 2.48 µm absorption were found east of Gale (yellow). Some of the layers within Mt. Sharp also contain hydrated minerals; one example is the units within CRISM scene 58A3.

We observed broad 1-µm absorptions in several locations in the rim and wall rocks, with band centers and widths indicative of the presence of olivine (Figure 3). The broad 1-µm absorption of olivine is the result of three overlapping electronic transition absorptions, which change systematically in position and/or strength with iron content and grain size [*Sunshine and Pieters*, 1998]. Olivine is detected in the rim bedrock in a small knob in C95A on the western wall (CRISM images will be referred to with the image type prefix and leading zeroes removed) as well as within the incised walls of Farah Vallis to the southwest. Additional detections occur on the walls and in craters (discussed further in section 4.2). Though OMEGA data show pyroxene absorptions, associated with the southern rim of Gale [*Anderson and Bell*, 2010], the broad 2-μm feature characteristic of pyroxenes is absent or weak in both ratioed and unratioed CRISM scenes of the Gale rim. This is consistent with work in the greater Gale region where olivine is the dominant mafic signature with pyroxene accompanying it in some but not all CRISM scenes [*Ehlmann and Buz*, 2015]. An exception to the lack of pyroxene is within sand dunes on the Gale crater floor, where pyroxene absorptions are variably strong, consistent with previous studies [*Lane and Christensen*, 2013; *Seelos et al.*, 2014; *Lapotre et al.*, 2017]; however, we do not focus on the dunes in this study.

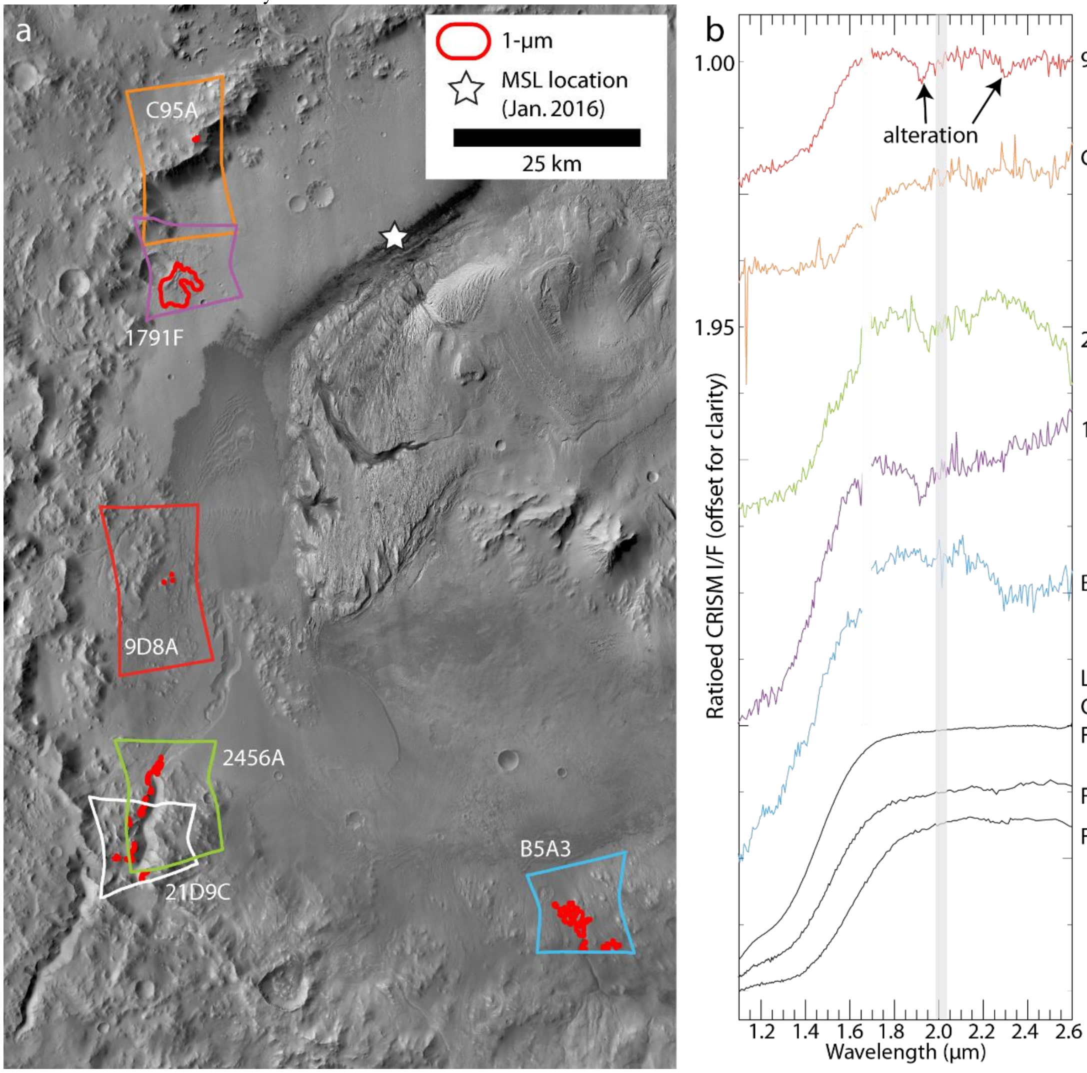

Figure 3: A) Olivine-bearing materials are observed in the wall and rim of Gale crater with CRISM-detected locations mapped on a CTX mosaic. In CRISM scene B5A3 the 1-μm absorption is particularly strong and widespread. In scenes 2456A and 21D9C the detections are in small exposures along the top of the carved channel. Very small areas with mafic detections are also present in scenes 9D8A and C95A. B) A broad absorption feature at 1-μm is due to electronic transitions of iron in the olivine structure. The olivine detected in CRISM scene 9D8A also has absorptions, indicating the presence of a phyllosilicate mineral, either from spatially mixed phyllosilicate-bearing materials or alteration of the olivine. Fo51 and Fo18 spectra are from Clark et al. [2007], and the Fo90 spectrum is from Sunshine and Pieters [1998].

Absorption features associated with hydrated and hydroxylated minerals are relatively widespread, detected in nine localities (Figures 2, 4). The phase detected is most commonly Fe/Mg phyllosilicate, though not all OH/H_2O-bearing minerals detected are Fe/Mg phyllosilicates. Some locations examined exhibit absorptions from both hydration and hydroxylation, consistent with Fe/Mg smectite clays. Other locations only exhibit absorptions associated with metal-OH vibrations (near ~2.3 μm and ~1.4 μm); still other locations only exhibit 1.9-μm vibrational absorptions due to the H_2O molecule in the mineral structure (Figure 4). In the 1.4 μm range both H_2O and metal-OH absorptions can co-occur. The exact wavelengths of the absorptions are determined by the metal octahedral cations present in the mineral, which can be detected and discriminated in Martian spectra of Fe/Mg phyllosilicate-bearing terrains [*Bishop et al.*, 2002; *Bishop et al.*, 2008; *Ehlmann et al.*, 2009; *Michalski et al.*, 2015], including within the Gale region. CRISM spectra examined show that most Fe/Mg phyllosilicates identified by the ~2.3-μm absorption and detected on the rim, wall, and floor of Gale are spectrally distinct from the stratigraphic layer containing nontronite in Mt. Sharp identified by Milliken et al. [2014], as previously reported for a few select locales [*Ehlmann and Buz*, 2015]. The Mt. Sharp spectra are most similar to Al-substituted nontronite due to the absorption shoulder at ~2.24 μm, an Al,Fe-OH vibration [*Milliken et al.*, 2010]. None of the wall, rim, or floor detections have such a pronounced shoulder, although some may have a subtle signature at this wavelength such as scenes 2456A and 21D9C (Figure 4). Many of the detections with metal-OH absorptions present have a 2.3-μm absorption which lies intermediate to the band centers observed for Fe and Mg smectites (Figure 4c; see also section 5.1).

On the eastern rim of Gale crater and nearby bedrock exposures, two CRISM scenes reveal a new discovery: H_2O-bearing materials with strong 1.9-μm absorptions and which sometimes possess a broad absorption at ~2.48 μm (Figure 5). The strength of the 2.48-μm feature typically decreases when the strength of the 1.9-μm feature increases. The relative strengths of the 2.48 μm and 1.9 μm features vary within the scenes. The 2.48-μm absorption is not characteristic of one mineral in particular but may be due to H_2O in a mineral structure [e.g., [*Clark et al.*, 1990]]. We compared the CRISM spectra to a number of sulfate, zeolite, and akaganeite spectra because these minerals all have absorptions in this wavelength range. Akaganeite has been detected in nearby Sharp crater to the west [*Carter et al.*, 2015] while mono- and poly-hydrated sulfates have been detected in Gale crater sedimentary rocks visited by Curiosity (though in low bulk abundance, e.g., Vaniman et al. [2014]) and within the Mt. Sharp group from orbit [*Milliken et al.*, 2010; *Fraeman et al.*, 2016].The wavelength position observed is most similar to bassanite, $CaSO_4{\cdot}0.5H_2O$, though the band centers in the 1.9 μm and 2.4 μm region could belong to a zeolite as well (Figure 5c). Though of generally similar spectral shape and with absorptions at a similar wavelength range, the absorptions appear at a slightly longer wavelength when compared with the Mt. Sharp sulfates from Fraeman et al. [2016]. Ultimately we are not able to definitively assign a unique mineral identification to this hydrated phase as the band centers are not at a wavelength diagnostic of one particular mineral.

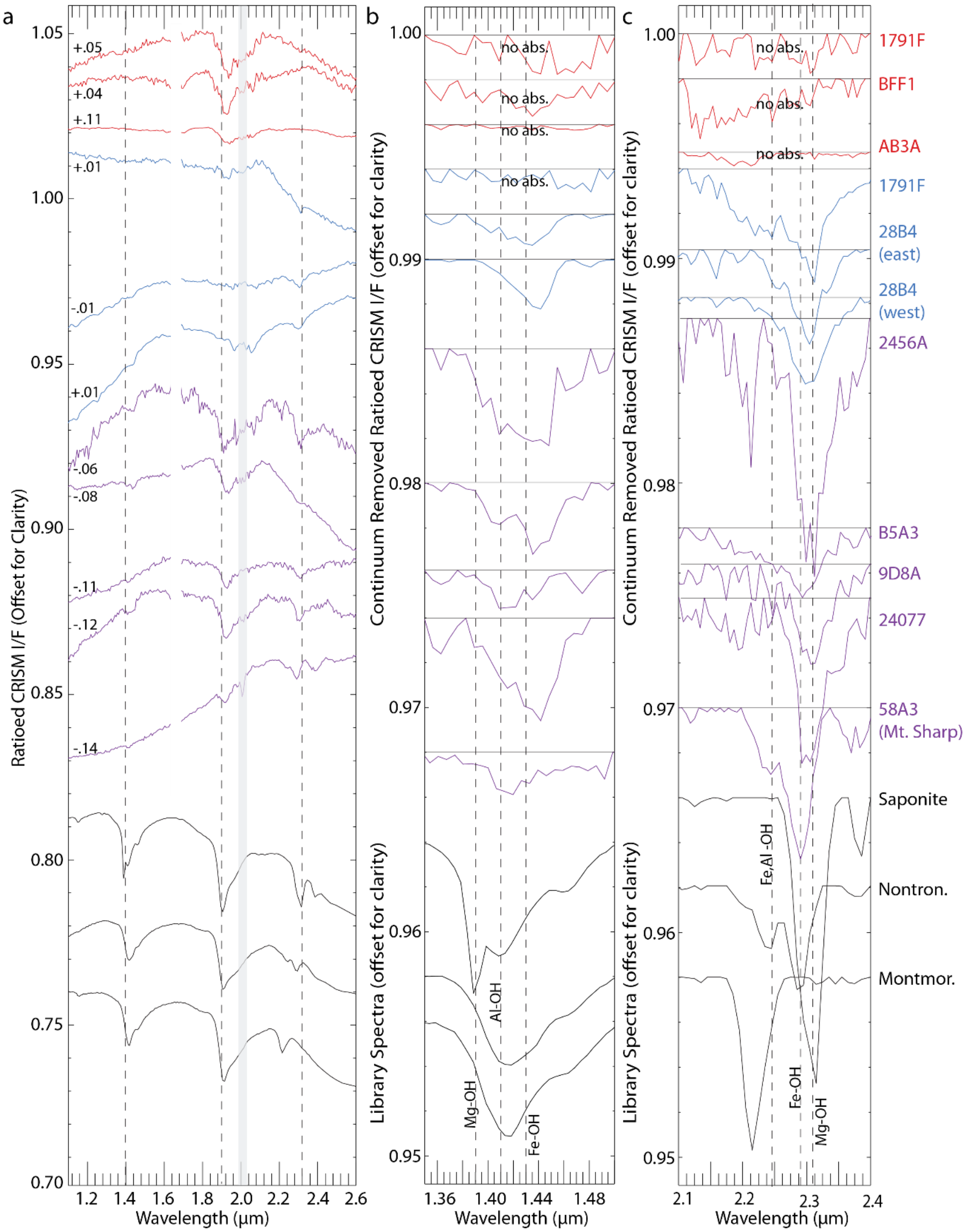

Figure 4: A) CRISM mineral detections compared to library spectra from Clark et al. [2007]. Some noise-removal code processed spectra of hydrated/hydroxylated materials only exhibit the H_2O absorption at 1.9 μm (red), while others exhibit only hydroxylation absorptions at 1.4 and/or 2.3 μm (blue) that permit the phase(s) present to be identified. There are also several materials that exhibit both hydration and hydroxylation (purple). Wavelengths used for the

CRISM spectra are extracted from ancillary data so as to account for the detector dependent spectral smile. B and C) The CRISM spectra are compared to library spectra of phyllosilicate minerals after applying a linear continuum removal over the absorption. The 1.4 and 2.3 μm band positions vary according to the metal ions present in the mineral. Interestingly, absorptions in materials from the wall and rim rocks are typically at longer wavelengths than Mt. Sharp nontronite spectra or library nontronite spectra. Additionally, the 58A3 spectrum from Mt. Sharp also shows a shoulder near 2.24 μm characteristic of Fe,Al-OH which is not present in most spectra from other locations within Gale.

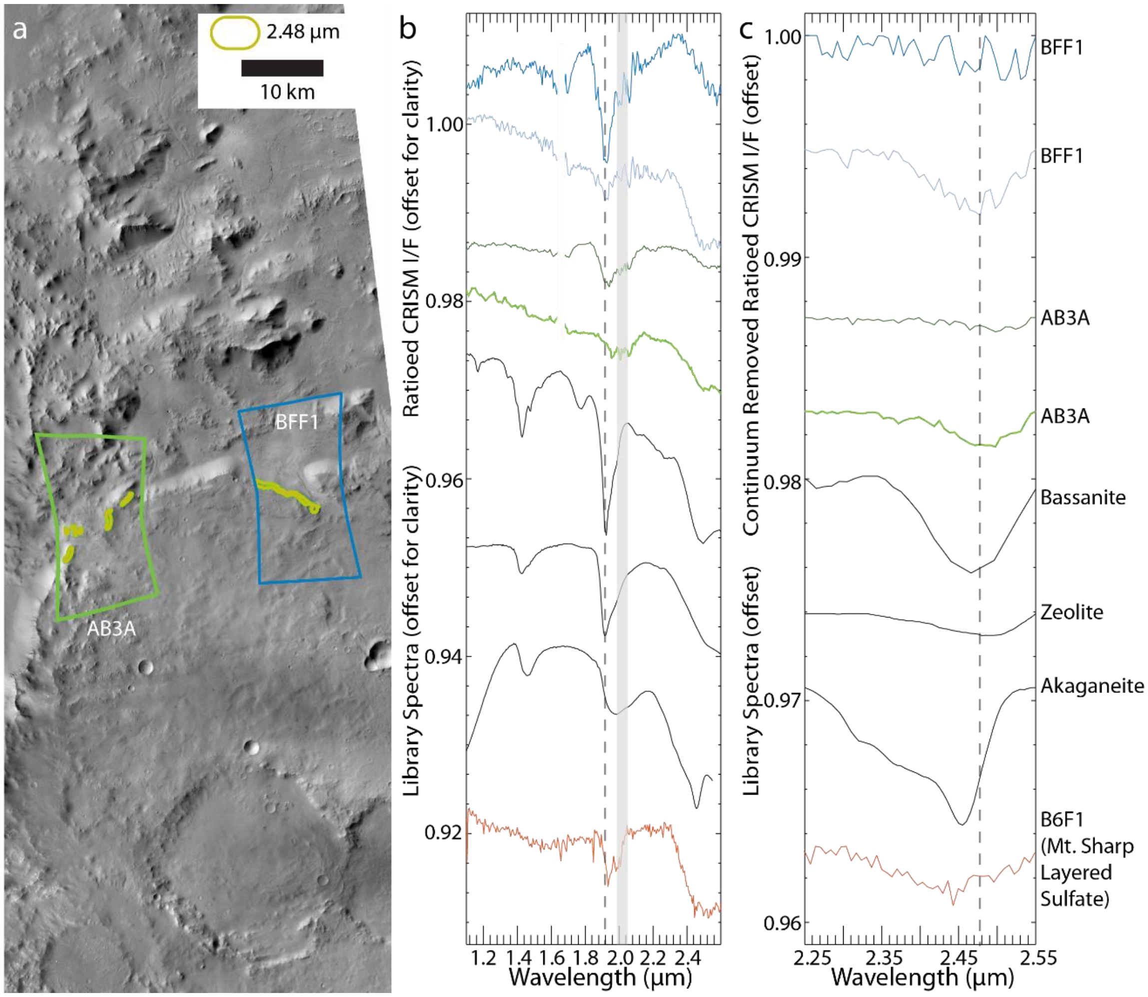

Figure 5: A) Eastern Gale CRISM scenes AB3A and BFF1 show distinct absorptions in the 2.48 μm region not found elsewhere in Gale. These absorptions, mapped on a CTX mosaic, are localized to the plateaus on a valley that cuts through the eastern Gale rim. B) CRISM spectra from scenes AB3A and BFF1 compared with library spectra of bassanite [*Clark et al.*, 2007], zeolite (chabazite, CRISM spectral library sample LAZE17), and akaganeite [*Bishop et al.*, 2015], as well as the layered sulfates from Mt. Sharp from Fraeman et al. (2016). A 1.9 μm feature is found in the regions with the 2.48 μm absorption. Materials with the strongest 2.48 μm absorption have weaker 1.9 μm absorptions. The grayed out wavelengths indicate a spectral region affected by residual atmospheric absorptions. C) Linear continuum removal in the 2.48

μm region shows the absorption is not uniquely characteristic of one single mineral when compared to library spectra.

The characteristic 2.2 μm feature of hydrated silica or Al-phyllosilicates has been found elsewhere on the Gale crater floor [*Seelos et al.*, 2014], in the Murray formation [*Milliken et al.*, 2010; *Fraeman et al.*, 2016], and in the watershed [*Ehlmann and Buz*, 2015]. Its presence in the analyzed scenes in this study is rare to absent; some scenes (2456A and 1791F) may show it subtly at about the level of noise in the data (Figure 4).

Overall, the Gale rim, wall, and floor has mineralogy similar to what has been detected in the greater Gale region [*Ehlmann and Buz*, 2015]. It appears predominantly mafic with the presence of Fe/Mg phyllosilicates. The phyllosilicate absorptions detections are similar between the walls and floor but distinct from Mt. Sharp [*Milliken et al.*, 2010]. Hydrated minerals, possibly similar to sulfates detected within Mt. Sharp [*Fraeman et al.*, 2016], may also be present on the eastern Gale rim. No other hydrated/hydroxylated phases were identified, and iron-bearing feldspar is not found in the CRISM data.

4.1.2 THEMIS

The THEMIS DCS technique did not highlight large regions of distinctive silicate composition on the Gale rim or wall (Figure 6), e.g., from lithologies significantly enriched in feldspars. The most pronounced units in the DCS mosaics are of the active sand dunes, which in both stretch combinations show their enhancement in mafic phases, an expected result based on prior study (e.g., Lane & Christensen [2013]). "Ghosting", an effect caused by band-dependent contributions from stray light in the detector combined with small-scale surface temperature differences, was also present in the scenes, in particular along the Gale rim [*Bandfield et al.*, 2004]. Ghosting appears as color variation within the DCS, down-track from features with temperature variability. The 8/7/5 DCS did, however, reveal small pink regions on the Gale rim and floor with potential olivine (Figure 6). Some of these regions corresponded to regions previously identified to have broad 1 μm absorptions through low resolution CRISM mapping products but are not yet covered by CRISM targeted images.

4.2 Geologic settings of mineral detections

Here we describe the morphologic characteristics of areas in which the spectroscopic detections are made, as seen in HiRISE and CTX data in order to determine the setting of each detection and describe their occurrence/extent.

4.2.1 Southern Gale wall

CRISM image B5A3 with detected olivine and Fe/Mg phyllosilicates is situated on the sloping southern wall of Gale crater, 15-km downslope from the rim (Figure 7; see Figure 1 for MOLA topography). The gentle slope (~7°) of this region in comparison to the steeper slopes seen in northern Gale (~12°) may indicate that there is mantling material atop the crater bedrock wall. A fluvial channel roughly bisects B5A3 and terminates just prior to a set of sand dunes at the base of the southern wall (Figure 7). Olivine is present throughout most of the scene, but olivine-related absorptions are enhanced in certain locales. Localized, more pronounced olivine signatures are seen in the southeastern corner of the CRISM scene, associated with small craters. In the middle of the scene, a 1.5-km crater and its ejecta show enhanced olivine and Fe/Mg phyllosilicates (previously reported by Wray [2013]). A sharply ridged downslope deposit enters

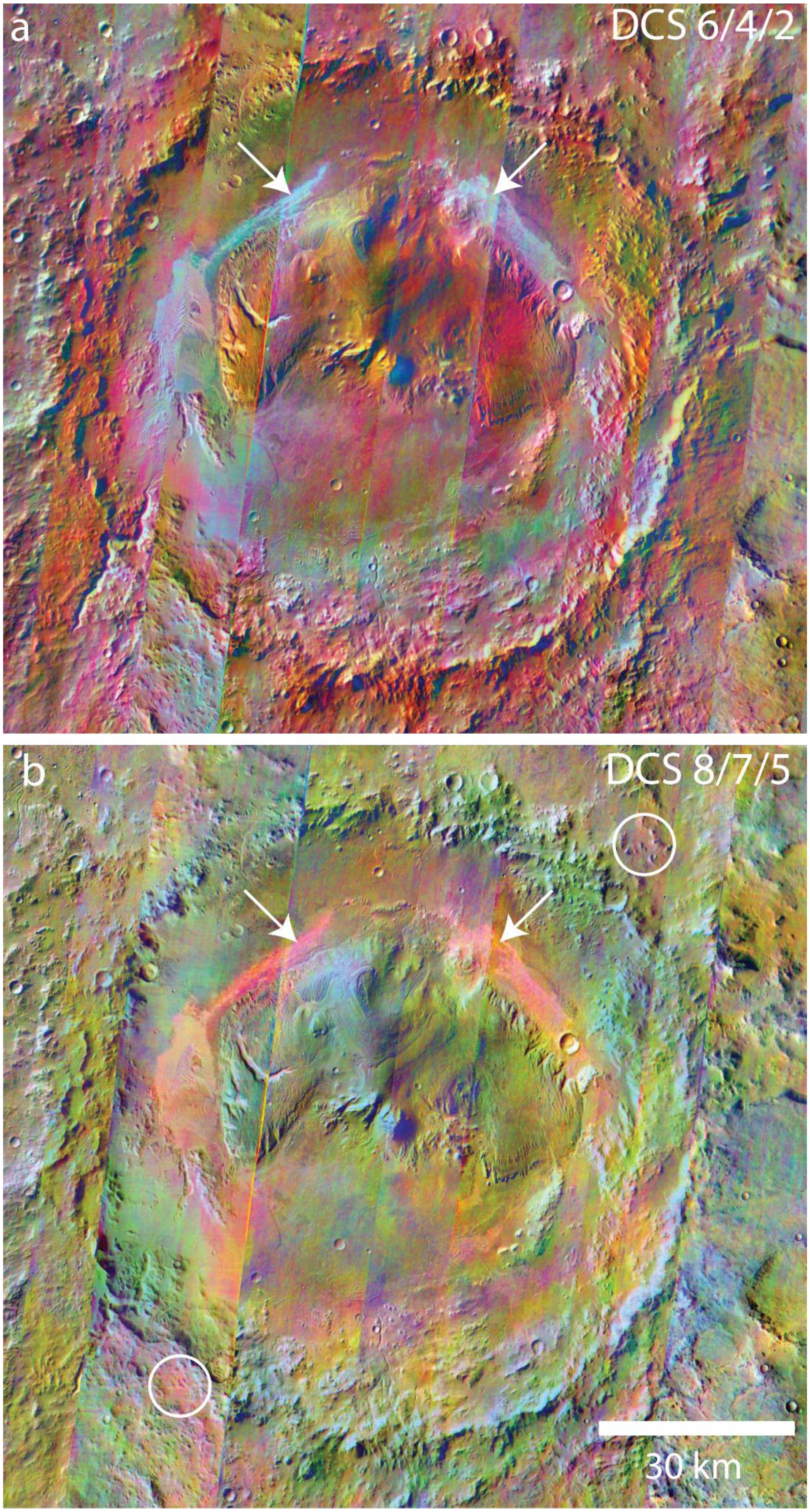
a
DCS 6/4/2
b
DCS 8/7/5
30 km

Figure 6: THEMIS DCS mosaics over the study area. A) Mosaic of DCS 6/4/2 (R/G/B) which highlights the sand dunes at the base of Mt. Sharp in cyan. The majority of the scene is red/pink and the rim and wall do not demonstrate significant heterogeneity aside from ghosting artifacts. B) Mosaic of DCS 8/7/5. Magenta/pink hues on part of the crater floor may indicate mafic mineralogies. The basaltic sand dunes are highlighted most prominently (indicated by arrows). Subtle pink regions (circled) in the rim correspond to a broad 1 μm absorption in CRISM mapping products.

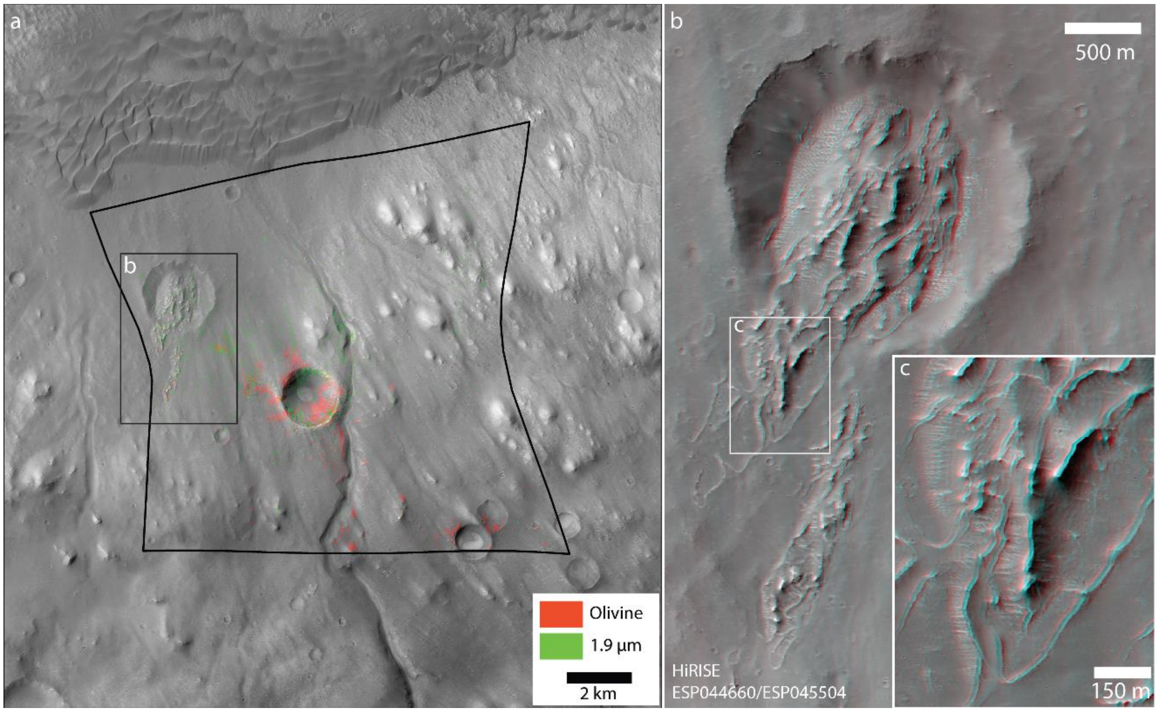

Figure 7: A) CRISM scene B5A3 images the southern wall of Gale crater. This wall is gently sloping, compared to the northern wall, which could mean that the Gale basement rocks in the crater rim are mantled by newer material. Olivine signatures are present in much of the scene; areas with the strongest absorptions highlighted in red. Additional absorptions due to H2O in minerals are present in the vicinity of the central small crater in this scene as well as within a landslide deposit. These hydrated materials are not associated with the channel dissecting the scene. B) A landslide enters and partially fills a small crater in the northwest of this scene. C) Zoom in of the landslide's sharp ridges which are well correlated with 1.9-μm, H2O absorptions in CRISM data.

another crater and probably represents a landslide of materials derived from higher up on the Gale wall (Figure 7b-c). The landslide has been mantled by a thin smooth layer of material, differentially eroded along its edges and obscuring the nature of its initiation (Figure 7b-c). Along the ridges of the landslide deposit are materials with 1.9-μm and 2.29-μm absorptions, consistent with an Fe-smectite like nontronite. There is no correlation between the mineral detections and the channel, which bisects the scene. Of all the phyllosilicate detections made in the Gale rim and wall, the location of the center of the 2.3-μm absorption of this scene best matches that of Mt. Sharp, although the Fe,Al-OH shoulder is absent, thus implying little Al in octahedral sites of the clay mineral.

4.2.2 Southwestern rim-incised valley (Farah Vallis)

A >40-km long valley incises the southwestern Gale rim and is known as Farah Vallis. Two CRISM scenes at the lower terminus, 2456A and 21D9C, exhibit abundant olivine and Fe/Mg phyllosilicate signatures (Figure 8). HiRISE imagery in this area shows that the margins of the valley are dark, rough-textured, and have signs of active modification such as boulder trails. Olivine-related, 1-μm absorptions are strongest along the steep valley rim in light-toned material (Figure 8b), while Fe/Mg phyllosilicates are found immediately below in dark, more recessive material. A ~1-km crater has impacted along the slopes of Farah Vallis (Figure 8c). This crater, has particularly strong absorptions due to Fe/Mg phyllosilicate in the rim and walls. A portion of the rim of this small crater appears to have slumped downhill (Figure 8c). Spectra shown in Figure 4 indicate the possible presence also of an Al-OH absorption near ~2.2 μm, characteristic of Al-phyllosilicates like kaolinite and montmorillonite that are either spatially or intimately mixed within the CRISM pixels over the Fe/Mg phyllosilicate; the Al-OH absorption is very subtle, at about the level of the noise, if indeed present.

4.2.3 Western Gale wall

CRISM half resolution image 9D8A was acquired over the lower portion of the western Gale wall (see Figure 9; Figure 1 for MOLA topography). The northeastern corner of the scene includes olivine-bearing sand dunes. Small detections (several pixels) of altered olivine and phyllosilicate material are made along the tops of small knobs along the lower wall (Figure 9b). HiRISE scene PSP007211 shows that these detections occur on the roughest material, exposed where occasional ~1m boulders are present (Figure 9c).

4.2.4 Northwestern Gale wall and floor

A ~5 km crater has impacted the approximate boundary between the Gale wall and floor. The majority of this crater and its ejecta blanket are captured in CRISM scene 1791F (Figure 10). There is heterogeneous exposure of olivine and Fe/Mg phyllosilicate-bearing materials in the crater ejecta and in its walls. The relative strengths of the H_2O and metal-OH bands are variable within the scene (two spectra, Figure 4). Although olivine is patchily found throughout the ejecta blanket, one particular southeast-extending streamer has an especially pronounced spectral signature.

Half resolution CRISM scene 28B4 captures part of the northwestern Gale floor and samples crater ejecta, sand dunes, inverted channels, and several stratigraphic units. The small exposure of ejecta is the distal extent of the crater ejecta in 1791F and does not display any spectral features in this CRISM scene. The inverted channels are inferred from their long, and branching nature seen in HiRISE/CTX and terminate in similar long and branching depressions. These channels are also spectrally bland. The sand dunes are enriched in olivine and pyroxene but are not further studied.

The stratigraphy imaged by CRISM on the crater floor includes four units: a dark, spectrally bland cliff-forming unit, a large hummocky and partially polygonally fractured unit with associated hydroxyl-related absorptions, a hydroxylated, light-toned material visible in depressions, and a small area of ridged hydrated material, which is more extensively covered in full-resolution scene 24077 (Figure 10). The cliff-forming unit appears to overlay the other units. The hummocky material is exposed to the east of the dark cliff-forming material. HiRISE

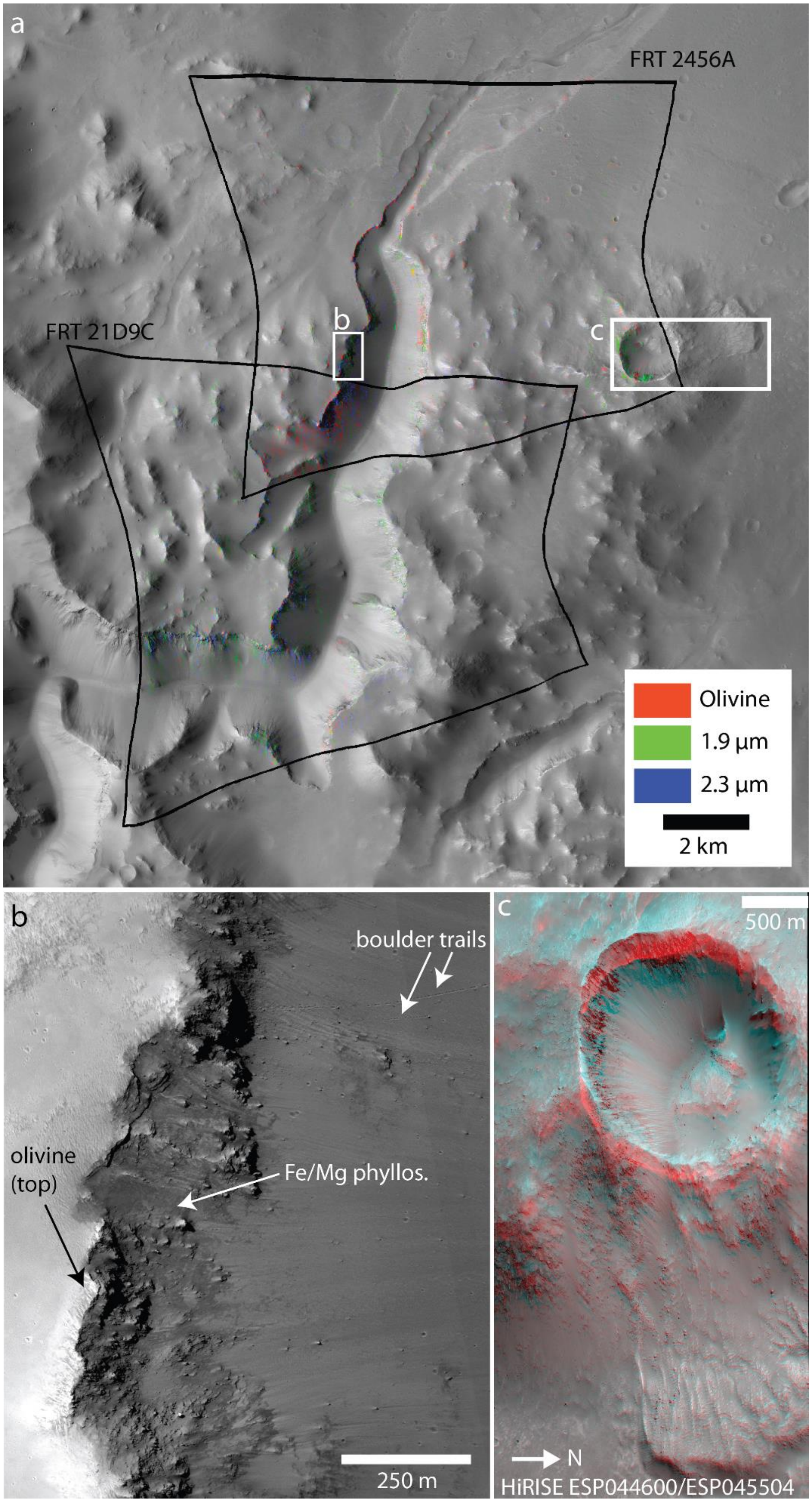
a
FRT 2456A
FRT 21D9C
b
c
Olivine
1.9 µm
2.3 µm
2 km
b
boulder trails
olivine (top)
Fe/Mg phyllos.
250 m
c
500 m
N
HiRISE ESP044600/ESP045504

Figure 8: A) Farah Vallis dissects Gale crater from the southwest. Fe/Mg phyllosilicates are found in the plateaus around the valley as well as in a small nearby crater. A distinct, olivine-bearing unit overlies the phyllosilicates. Although in some regions of the channel, the olivine-bearing material is found coming down the channel walls, it appears to be stratigraphically above the phyllosilicates. A landslide is found to the east of the small phyllosilicate bearing crater. B) The channel walls are freshly exposed as evidenced by the rough textures observed, their low albedo, and boulder trails. C) A HiRISE anaglyph (must be viewed in N-up orientation) of the small phyllosilicate-bearing crater shows that part of the crater wall appears to have slumped downhill and that the impacted material may be susceptible to mass wasting events.

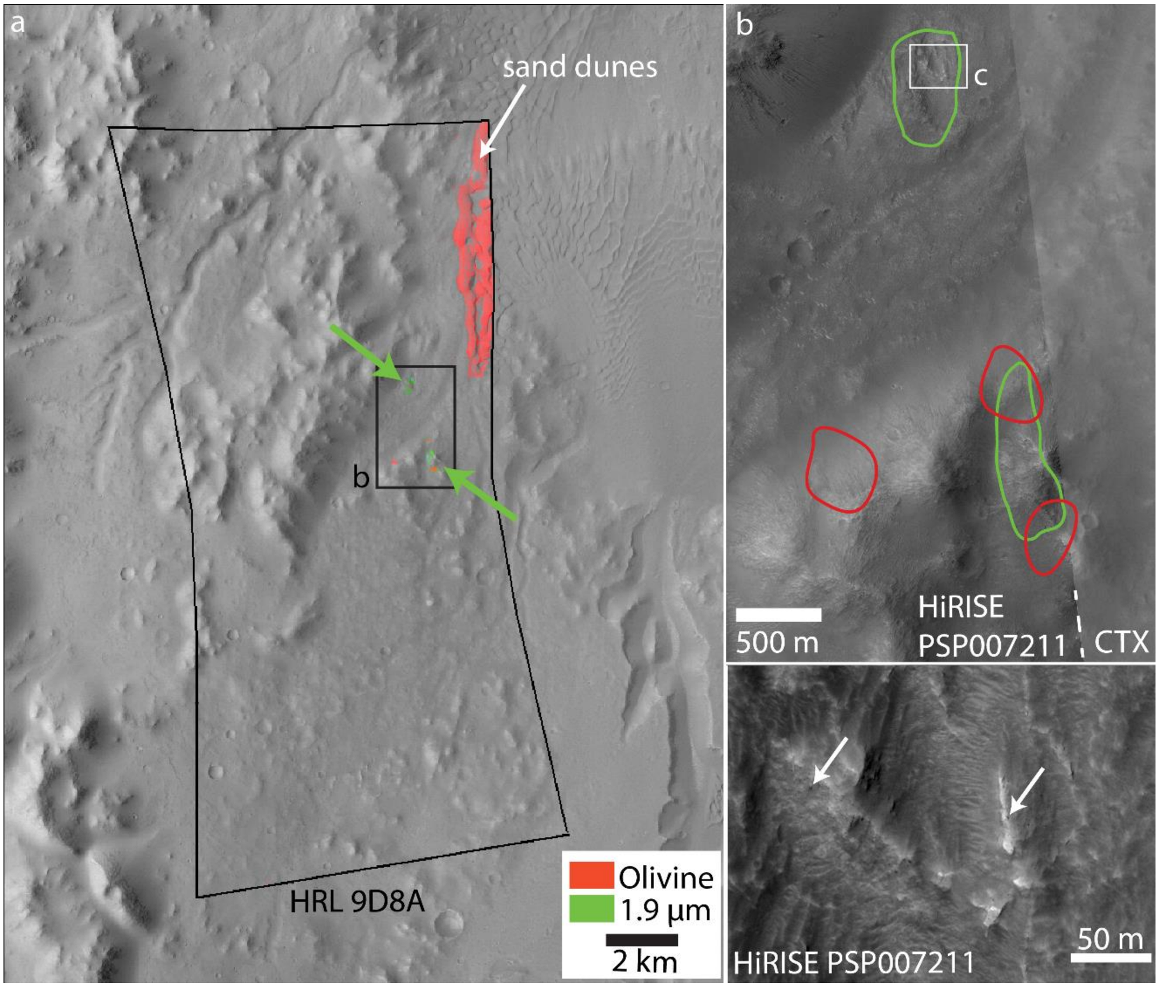

Figure 9: Small phyllosilicate occurrences on the western Gale wall. A) Localized exposures of hydrated and mafic materials are present on the western Gale wall in CRISM scene 9D8A. B) Using high resolution imagery, where available, these features appear to emanate from exposed bedrock rather than filling units. C) At the highest resolution some ~1m boulders are apparent (indicated by the white arrows) along ridges where hydration is found. There is nothing particularly distinct about the regions where the mineral signatures are present except that they are ridges where erosion and removal of dust may facilitate CRISM detections.

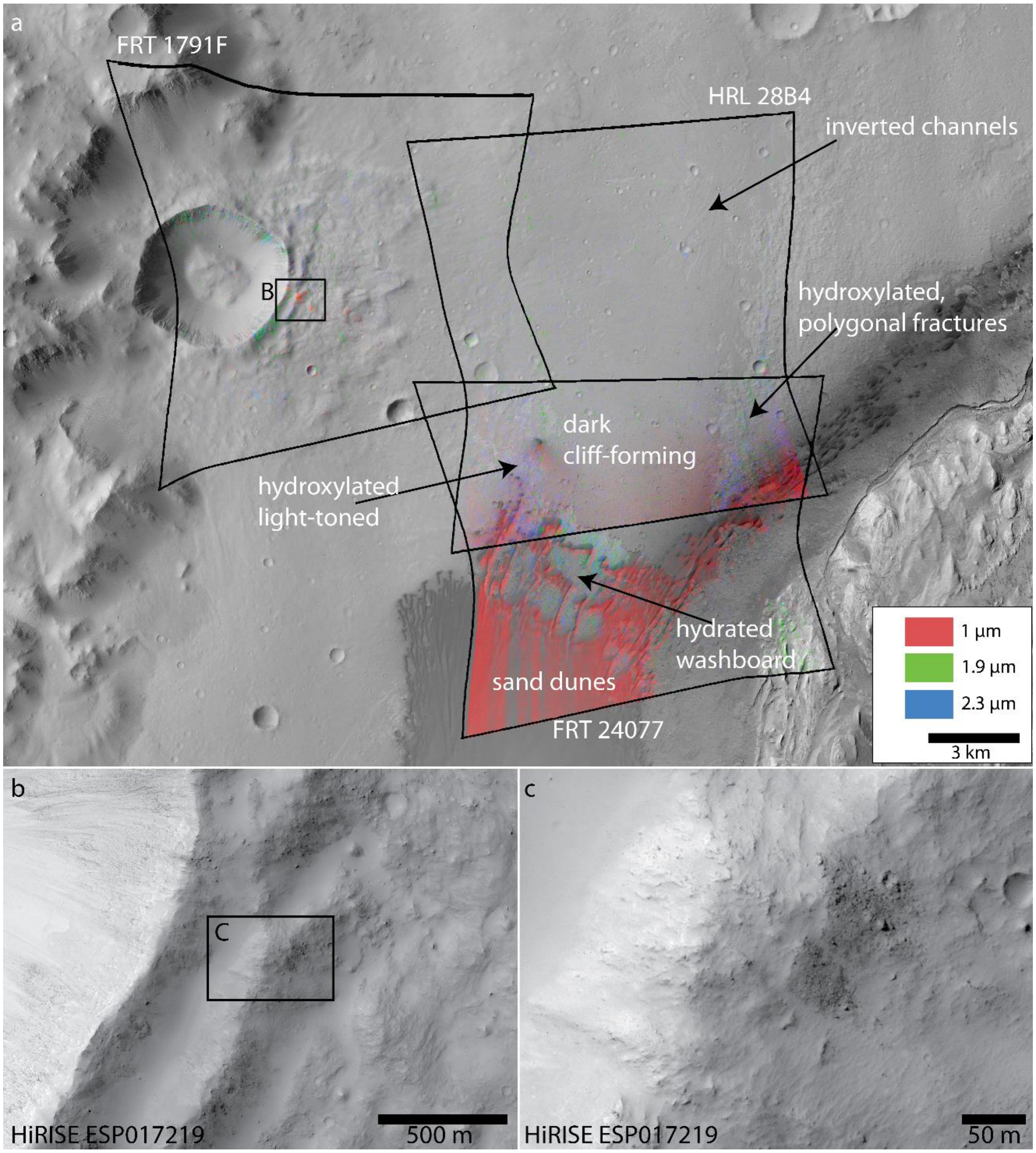

Figure 10: Mineral detections on the wall and floor in Northwest Gale. A) A 5-km diameter crater in CRISM scene 1791F has impacted Gale right at the wall/floor boundary. The crater ejecta blanket is relatively intact and exposes mafic and hydrated/hydroxylated material (previously identified by Wray [2013]). It is unclear if the crater is excavating Gale bedrock or later deposits but depth-diameter scaling suggests that it may sample the Gale basement. CRISM scene 28B4 samples a dark capping unit, polygonal units on either side of this cap (which includes the fine scale polygonal fracturing in the washboard unit), inverted channels, the edge of a previously-identified washboard-textured unit [Milliken et al., 2014], and sand dunes. Both of the polygonal units to the east and west of the capping unit exhibit hydroxylation. Other geologic units within the scene are spectrally bland. In scene 24077, strong hydration and hydroxylation features are seen in the washboard unit, previously identified by [Milliken et al.,

2014]. B) High resolution imagery is available of the crater ejecta. Phyllosilicates and olivine are detected patchily in the crater wall and in ridges of ejecta. C) The strongest mafic signatures appear to be correlated with dark, rough patches of material in the crater ejecta.

correlation with CRISM indicates that although the hummocky topography extends further, the hydroxylation is limited to a region which also bears polygonal fractures. The light toned material is exposed to the west of the dark cliff-forming material and appears recessive and has limited exposure: it is only visible within depressions and as a layer between more competent units. The CRISM hydroxylation associated with it is similarly limited to a small area: multiple patches of several pixels each. The texture and morphology of these hydroxylated units are further discussed and imaged in Section 4.3.2. The two hydroxylated units have absorption band positions at a similar wavelength in the 2.3 μm region, but the absorption positions vary slightly in the 1.4 μm region; the 1.9-μm H_2O absorption is weak to absent in both (Figure 4, '28B4 (west)' from the light-toned material and '28B4 (east)' from the polygonally fractured material). These units also have absorptions in similar position to the phyllosilicates in scenes 2456A and 9D8A (described in Section 4.2.2-3) though are missing the water absorption at 1.9-μm. The ridged material, more extensively covered in scene 24077, was previously studied by Milliken et al. [2014] and found to be of possible aeolian origin, inferred based on the "washboard" appearance of regularly spaced ridges, which may record large-scale cross-stratification. The ridged material also contains Fe/Mg phyllosilicates, perhaps formed by diagenesis [Milliken et al., 2014], is spectrally distinct from the two hydroxylated units, and has polygonal fracturing on the meter-scale.

4.2.5 Eastern Gale

A channel which originates from farther east breaches the eastern Gale rim (Figure 11). The north facing walls of this channel and of other nearby knobs host the hydrated material with a broad 2.48-μm absorption. These materials are not found in the debris or channel floors. HiRISE imagery indicates that some of the material is associated with boulders but otherwise the host units are not clearly defined.

4.3 Geologic mapping and stratigraphy of NW Gale crater floor

Geologic mapping of the floor of the northwestern part of Gale crater using mineralogy and morphology reveals several orbitally-defined units, which we relate to stratigraphic units that have been identified by the Curiosity rover team (Figure 12), and units identified on the walls and rim of Gale. Some of the northwest Gale floor has not been mapped due to it being dusty, debris-covered, and/or spectrally bland. Collectively, the surfaces and units mapped, excluding the crater-exposed stratigraphy and mass wasting surfaces, span a ~150 m elevation range observed in MOLA data (Figure 13). The mapped areas are categorized as either geomorphic surfaces or geologic units. Surfaces, described in section 4.3.1, refer to regions which have distinct boundaries (can be traced) but which do not have any stratigraphic/paleoenvironmental information (e.g., crater ejecta). Geologic units, described in section 4.3.2, refer to regions with distinct composition (from CRISM) or appearance, which may be the result of a different formation environment when compared with their surroundings (e.g., hydrated thinly layered deposits vs. spectrally bland massive exposures).

Topographic and imagery data allow us to determine the stratigraphic relationships between some of the units. Additionally, within a fresh crater on the northwest floor, a series of layers is observed on the well-preserved walls. The lowest units exposed in the crater are below the elevation extent of the surfaces, landforms, and geologic units. We describe the sequence of layers observed in the crater walls and attempt to correlate it with some of the mapped floor units in section 4.3.3.

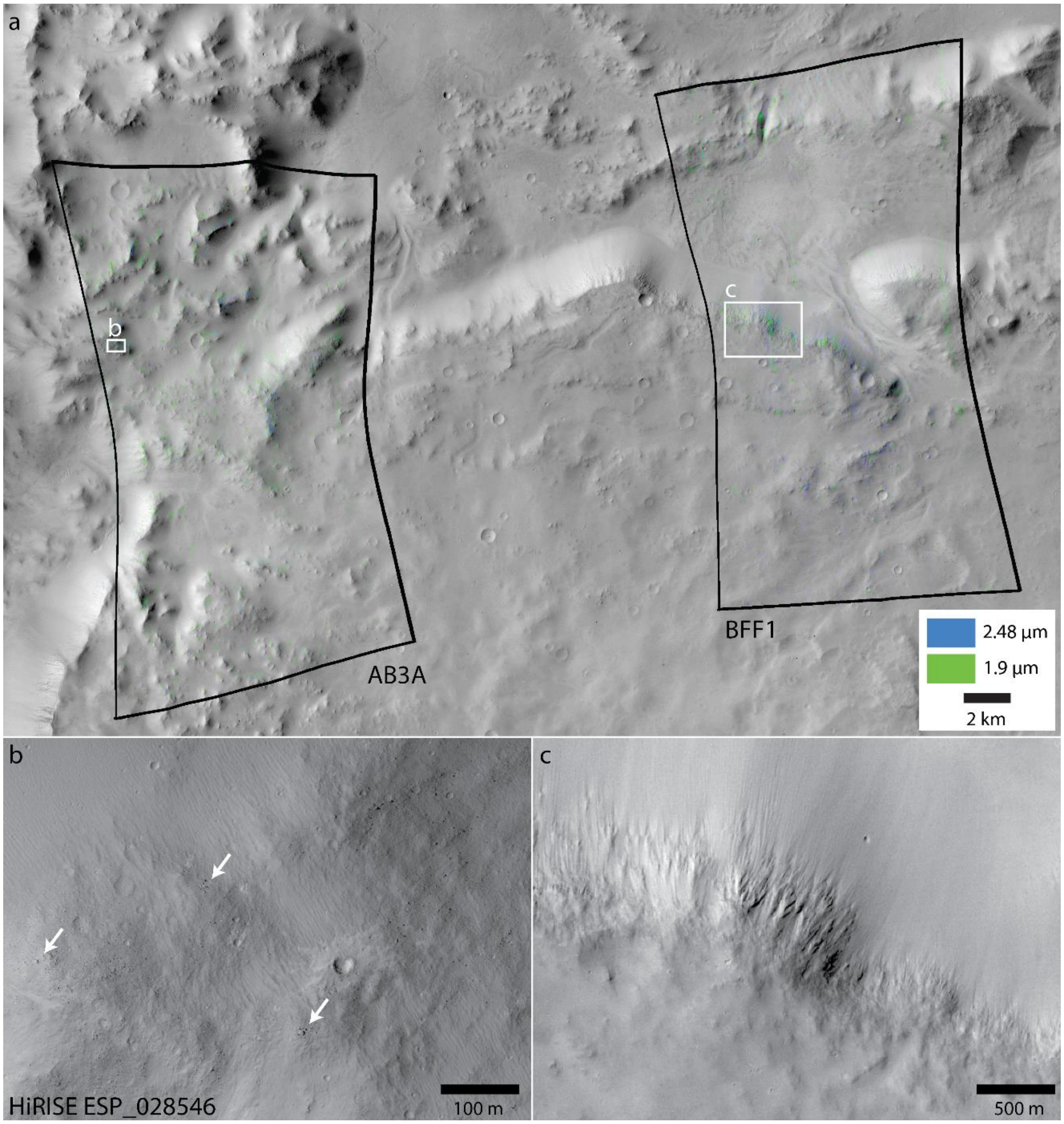

Figure 11 A) The H_2O and 2.48-µm absorption features in AB3A and BFF1 are present along ridges and scarps in Eastern Gale, where an entering valley incised along the dichotomy boundary. B) HiRISE imagery is available for part of CRISM scene AB3A. Highest resolution images show that the mineral detections are associated with darker, fresh surfaces with abundant boulders (indicated by arrows). C) The strongest detections in CRISM scene BFF1 lie along a steep slope.

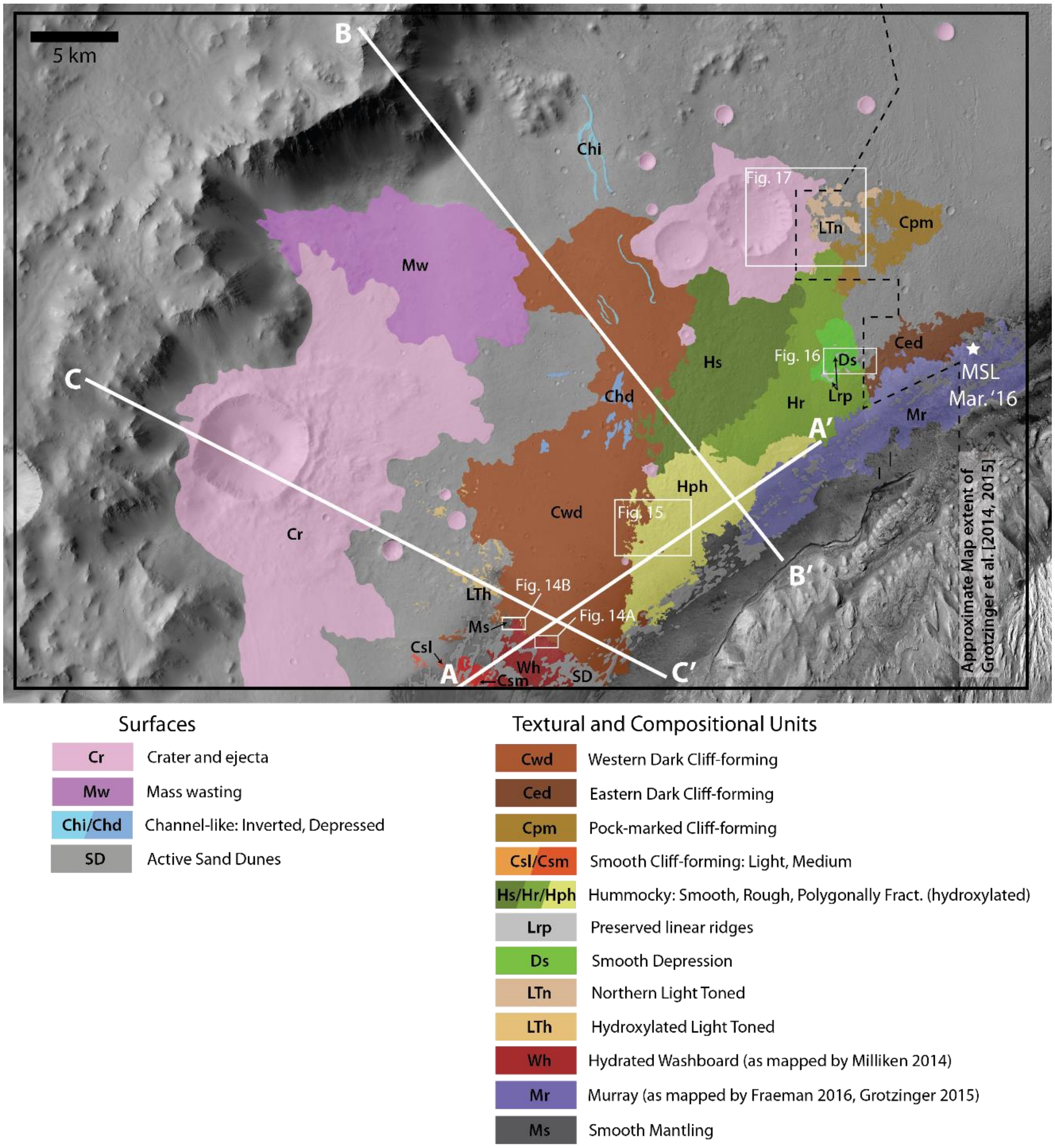

Figure 12 Geologic Map of the NW Gale floor (Top) Using imagery and mineralogical detections, we constructed a geologic map in NW Gale mapping surface landforms and geologic units. The compositional differences seen in CRISM correspond to morphological differences seen in CTX and HiRISE. The boundary for mapping done in Grotzinger [*Grotzinger et al.*, 2014; *Grotzinger et al.*, 2015] is indicated by the dashed line. By extending the geologic units drawn in previous high resolution orbital data maps of this region, we find that Cpm and Ced are likely part of the Bradbury Group [*Grotzinger et al.*, 2014; *Grotzinger et al.*, 2015]. Topographic profiles are shown in Figure 13.

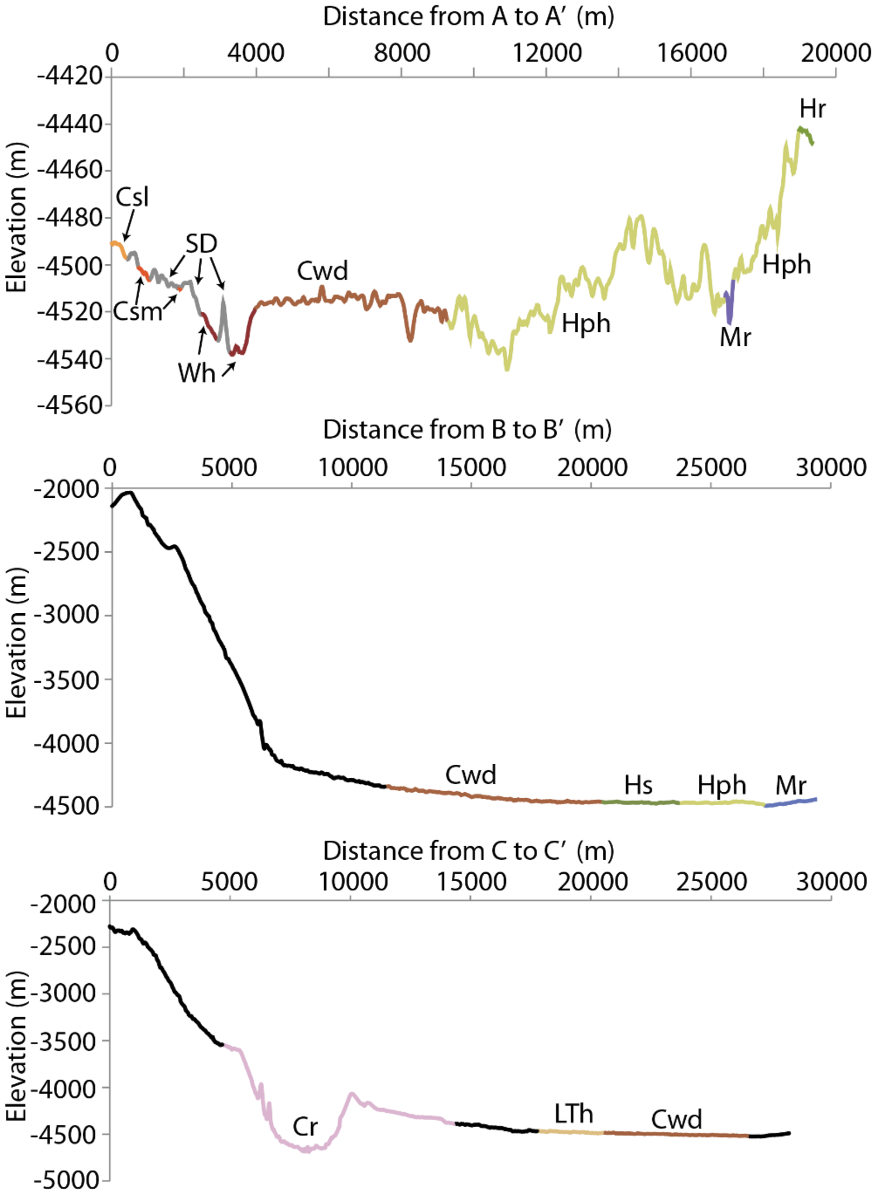

Figure 13: A) A topographic profile crossing many of the floor units near Mt. Sharp. B and C) Topographic profiles of the rim-to-crater floor transition show the generally flat nature of the Gale floor which may indicate significant sediment fill. The crater profiled in C demonstrates that the ejecta from this crater likely excavates both wall and floor materials.

4.3.1 Surfaces and landforms

Surface processes such as landslides and cratering have modified the walls, rim, and floor of Gale and obscured or modified some of the geologic units. Craters and their associated ejecta blankets that do not have any distinguishable layers have been mapped together (labeled Cr). A mass-wasting deposit (Mw) emanating from the northern Gale rim is also mapped. Mw is partially overlain by the ejecta of a ~7 km diameter crater, indicating Mw's older age. The Mw deposits extend approximately 7 km and terminate near their intersection with the dark competent material seen in CRISM scene 28B4 (section 4.2.4), mapped as Western Dark Cliff-forming unit (Cwd, further described later). A series of inverted channels (Chi) can be traced from near the base of the Northern Gale rim. These channels are oriented approximately in a north-south direction. The inverted channels terminate in broader channel depressions (Chd) within Cwd.

4.3.2 Geologic units

Over a dozen distinct sedimentary rock units were identified on the northwestern Gale floor. The mapping of the "washboard" unit (Wh) follows that of Milliken et al. [2010] (Figure 14). Mapping of the Murray formation follows that of Fraeman et al. [2016] and Grotzinger et al. [2015]. The remaining units are newly delineated in this work.

Multiple spectrally bland, competent, heavily cratered, resistant bedrock units were identified with distinctive morphologies that distinguish them from one another. These units are named after their cliff-forming attribute: Western Dark Cliff-forming (Cwd), Pock-marked Cliff-forming (Cpm), and Eastern Dark Cliff-forming (Ced). The cliff-forming units mapped, Cpm and Ced, correspond well with previous mapping done by the MSL team of the "Rugged Terrain" and "Cratered Surface" units, respectively [*Grotzinger et al.*, 2014]. While the Cpm pock-marked unit is somewhat localized, the Ced eastern dark unit is more extensively exposed and extends south and eastward toward the lower Mt. Sharp units being explored by Curiosity, including the Murray formation. The Cwd western dark unit is particularly well-defined due to its low albedo in comparison with the surrounding units (Figure 14). The thickness of this unit is approximately 20 m at its southwestern extent, based on the height of the cliff as computed from a HiRISE DEM and assuming horizontal emplacement. Two smaller cliff-forming units, characterized by their smooth appearance and light and medium albedos (Csl and Csm, respectively), are found in the south of the mapping area and are characterized by appearing similarly competent and spectrally bland. The majority of these two units, however, are covered in sand dunes.

A hummocky terrain unit is identifiable between the eastern and western cliff-forming units. Within this terrain there are three subregions, discriminated by texture: Smoother Hummocky (Hs), Rougher Hummocky (Hr) and Polygonally-fractured hydroxylated Hummocky (Hph). The polygonally-fractured unit (Hph) is characterized by a distinct, smaller scale texture of polygonal fractures, each approximately a few meters wide (Figure 15). The polygonal fracturing is coincident with spectral signatures of hydroxylation in CRISM data (scene 28B4, Section 4.2.4). The rougher and smoother hummocky units are distinguished based on the size and the frequency of the hills found within them. The differences between the subregions of this hummocky terrain may represent lateral variations within the unit or post-depositional changes segregated to different elevations.

Two small light-toned units were mapped: the Northern Light Toned (LTn) and the Hydroxylated Light Toned (LTh), the latter exposed in Figure 14. In common between these units is their high albedo and thin, recessive, nature. The hydroxylated light-toned (LTh) unit is so named because the CRISM coverage over it indicates a distinctive signature of hydroxylated minerals discussed in section 4.2.4. Although nearby and at a similar elevation to the polygonally fractured hummocky unit, it is texturally distinct. CRISM coverage over the northern light-toned (LTn) unit does not reveal any distinguishable mineralogy, but this may be due to dust cover.

As previously mentioned the two hydroxylated units have similar wavelength absorptions in both the 1.4 and 2.3-μm regions indicating a similar mineralogy (Figure 4). The

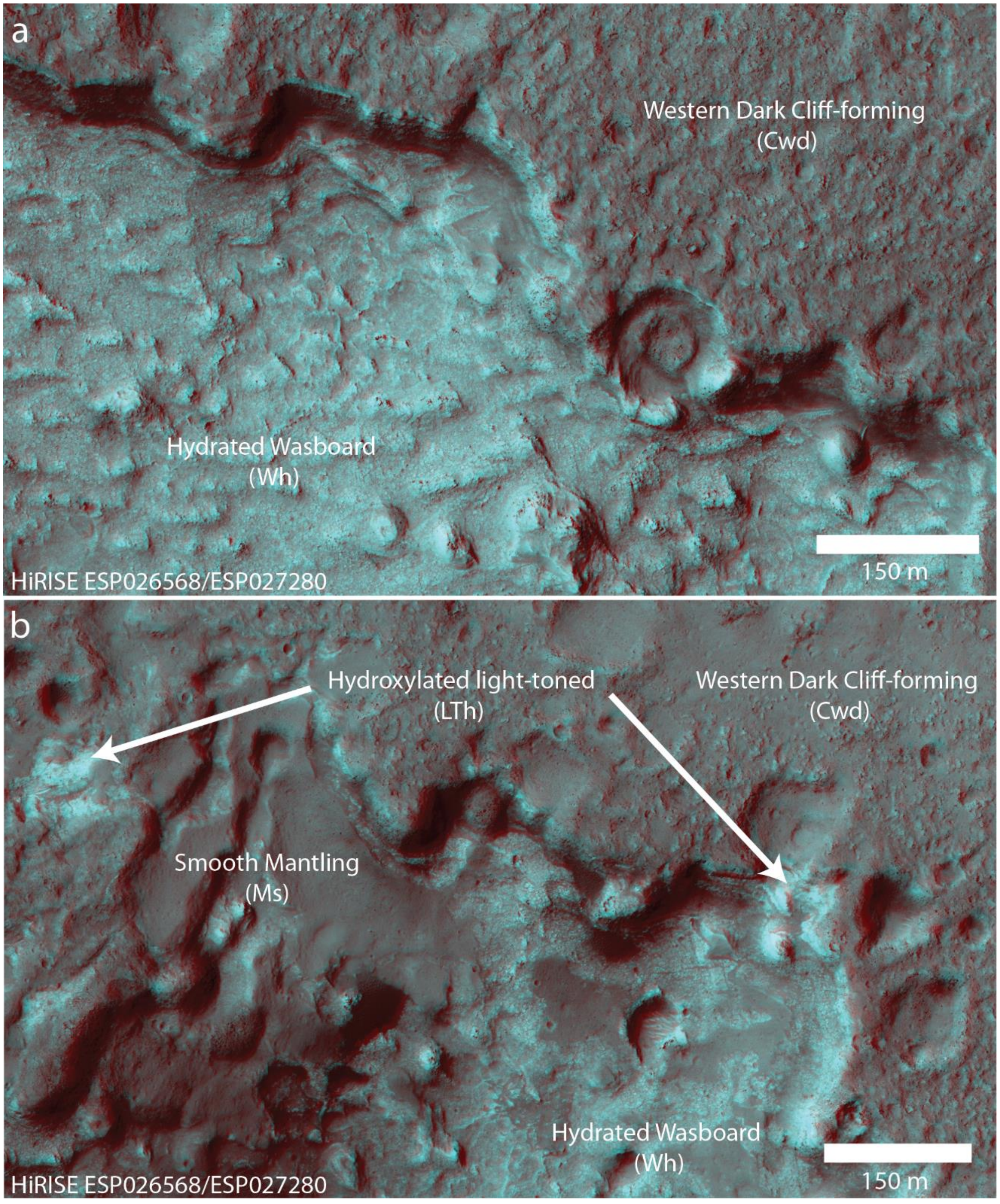

Figure 14. HiRISE (ESP 026568 and ESP 027280) anaglyphs of contacts at the western edge of a capping unit A) The phyllosilicate-bearing unit of preserved bedforms (Wh), characterized by distinct lithified linear dunes with a "washboard texture" as described by Milliken et al. [2014], has a sharp contact with the overlying spectrally bland and expansive cliff-forming unit (Cwd). B) At higher elevations a hydroxylated light-toned unit (LTh) appears between the washboard unit and the cliff-forming unit. There also appears to be a later event, which deposited a dark, bland, mantling material (Ms) onto all three units. Our interpretive stratigraphic column is shown in Figure 20.

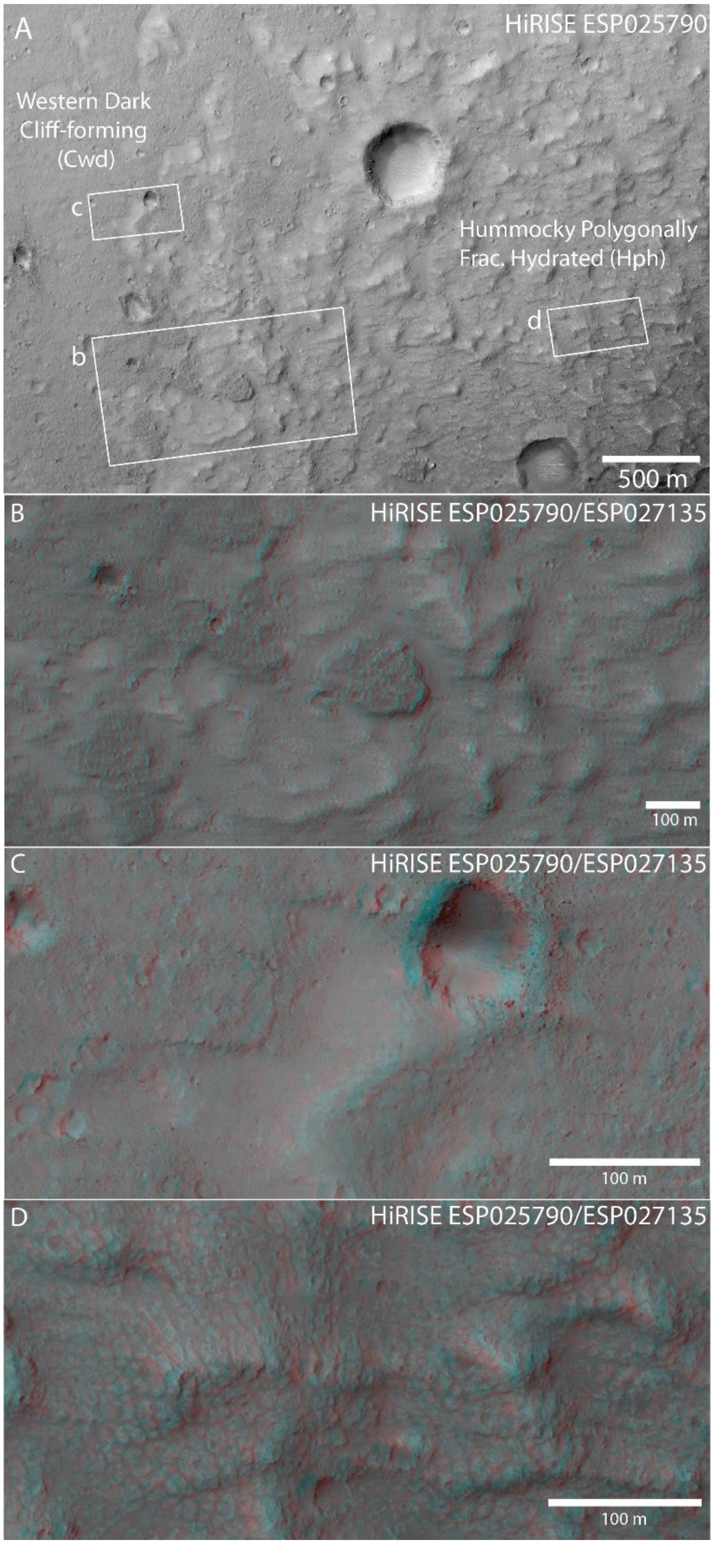

Figure 15 A) CTX image showing the contact between the dark capping unit (Cwd) (west) and hummocky polygonally fractured unit (Hph) (east). B) HiRISE anaglyph showing how Cwd appears to fill in topographic lows from Hph in an embaying relationship. C) HiRISE anaglyph

showing Hph emerging from below Cwd at a topographic high. D) HiRISE anaglyph showing a type section of Hph with several-meter scale polygonal fractures.

washboard (Wh) unit also has metal-OH absorptions at similar wavelengths, but also includes the 1.9-μm water absorption. Interestingly, these spectra have absorptions at similar wavelengths to the phyllosilicates detected in Farah Vallis and on the western Gale wall (CRISM scenes 2456A and 9D8A, respectively).

A mysterious dark depression approximately 3 km across (Figure 16) is almost completely surrounded by the hummocky terrain. Within the depression is a smooth material with a comparatively lower albedo, mapped as Smooth Depression (Ds). At the center of this smooth depression the material is highly polygonally fractured with raised ridges (Figure 16 inset). Additionally, large preserved linear ridges (Lrp) are present within the depression in close proximity to the fractures. These linear ridges are distinct from the polygonal ridges as they are in sets of parallel clusters (i.e., do not intersect). The stratigraphic relationship between this depression, the linear ridges and the hummocky terrain is not clear from the data available, i.e., whether the ridges only exist within the depression or whether they are in an underlying unit that crops out only in the depression.

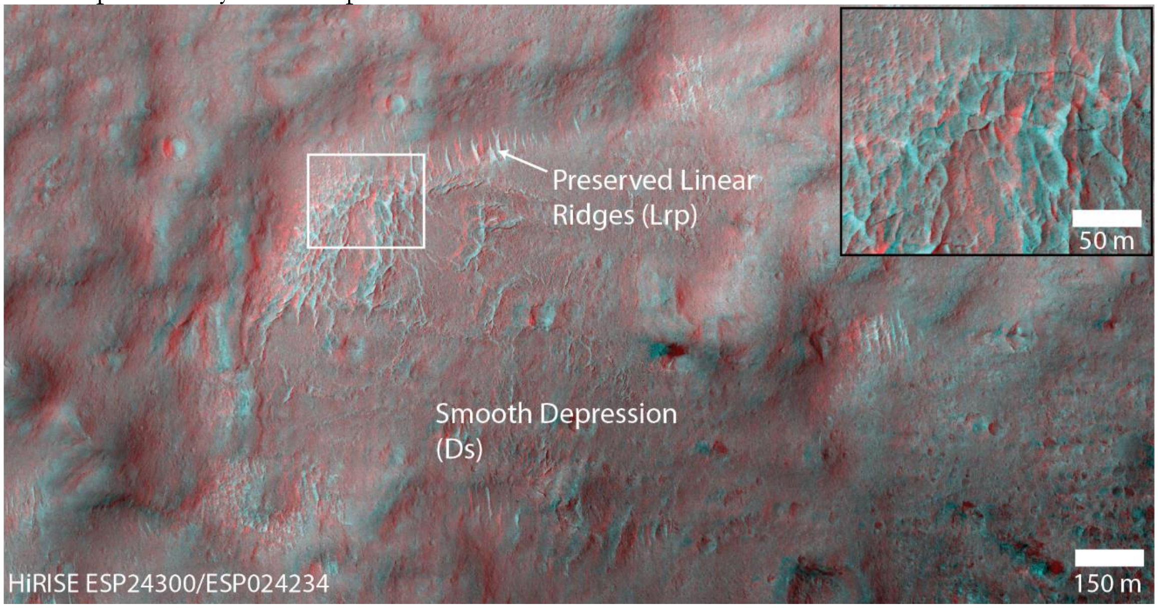

Figure 16 HiRISE anaglyph of the bottom of a smooth depression (Ds) on the Gale floor. Along the edges of the depression raised polygonal (inset) ridges and preserved linear ridges (Lrp) are present.

4.3.3 Exposed stratigraphy

Many of the stratigraphic relationships are hard to determine from orbit due to limits in the image and topographic resolution or because the contacts are obscured by dust, sand, or other units. However, a combination of image datasets and topography have allowed us to determine some of the stratigraphic relationships.

HiRISE anaglyphs (Figures 14 and 15) and DEMs (Figure 13a) over the western dark cliff-forming (Cwd) unit and adjacent exposures show a clear contact: the Cwd overlies a thin exposure of light-toned hydroxylated unit (LTh), which in turn overlies the washboard unit (Wh). The cliff-forming unit (Cwd) also overlies the polygonally-fractured hummocky unit

(Hph) and fills in depressions within the hummocky terrain (Figure 15). Cwd, LTh, and Wh are all partially overlain by a small deposit of a dark mantling material (Ms) (Figure 14).

A profile taken near the base of Mt. Sharp shows some of the elevation extents of the mapped units (Figure 13a). Apparent in this profile is the flat surface created by the western cliff forming (Cwd) unit and the hilly nature of the hummocky unit (Hr/Hs/Hph). Overall, the floor units are generally flat and gently dropping in elevation from the base of the Gale rim toward Mt. Sharp (Figure 13B).

The contact of the Murray formation (from [*Grotzinger et al.*, 2015; *Fraeman et al.*, 2016]) with the units mapped in this study (eastern cliff forming (Ced), and rough and polygonally fractured hummocky units (Hr and Hph, respectively)) does not occur at a single elevation. Rather the Murray appears to have significant vertical and lateral extent, meeting each unit at a different elevation. Rover-scale observations just east of our study region show that the Bradbury group, which corresponds to some of our mapped units (for example the eastern and pock-marked cliff-forming units (Ced and Cpm, respectively)), interfingers with and overlies the Murray unit [*Grotzinger et al.*, 2015].

A unique window into the stratigraphy of the Gale floor sedimentary deposits is provided by a relatively fresh ~4-km crater, the walls of which expose multiple geologic units spanning >250 m of continuous section (Figure 17). While the crater from Figure 10 does not demonstrate any distinguishable layering, the crater from Figure 17 has multiple identifiable units. The uppermost portion of the crater wall is characterized by brecciated material with meter-sized blocks and occasional light-toned fracture fill. The topographic profile of the crater (Figure 17c) shows that the breccia is limited to the region above the existing landscape, and therefore, likely represents disrupted materials and the crater ejecta. Outside of the crater, the northern light toned (LTn) unit is below the dark ejecta blanket and the dark pock-marked cliff-forming unit, Cpm. This light toned unit does not seem to be exposed within the crater. Below the brecciated unit relatively competent material is exposed, expressed as the large knobs (Figure 17b). This knobby material overlies several recessive units, which form a well-bedded, ~90-m thick layered sequence with alternating light and dark gray tones (Figure 17b). This 4-km crater excavates the deepest sedimentary units exposed within Gale crater. Its base is ~50 m below the lowest elevation explored by Curiosity (just east of Yellowknife Bay). A comparison of the depth of materials exposed within this crater with those mapped elsewhere on the northwest Gale floor shows that the recessive layers lie below the other units (Figure 18). In fact, the topographic extent of all of the orbitally mapped units are above or within the elevation boundaries of the knob forming layer. Thus, the ~100-m layered sequence of light-dark units represent the lowest elevation sedimentary units exposed in Gale crater. The layered sedimentary units extend to the base of the crater, indicating that Gale-impact related bedrock is not exposed. CRISM coverage is available in this crater, though no mineral detections were made.

5.0 Discussion

5.1 The mineralogy of Gale crater's rim and walls

Olivine and hydrated silicates are relatively widespread within the Gale crater rim and wall materials, extending previous scattered detections by Wray [2013] and Ehlmann and Buz [2015]. Around the western rim of Gale and in the portions to the southwest incised by Farah Vallis, the competent bedrock that comprises Gale crater's upper rim materials is olivine-bearing. No feldspar-rich lithologies were observed in CRISM or THEMIS data, though obscuration by dust cover precludes a truly comprehensive survey. Very small outcrops with mineral detections present in targeted CRISM scenes, indicate that a fruitful avenue for further investigation will be analyses of additional CRISM targeted data acquired of the Gale rim. These future data remain the best near-term means available for identifying potentially feldspar-rich lithologies in the Gale rim that may be related to the more alkali-rich or felsic float rocks detected by Curiosity [*Stolper et al.*, 2013; *Sautter et al.*, 2014; *Thompson et al.*, 2015].

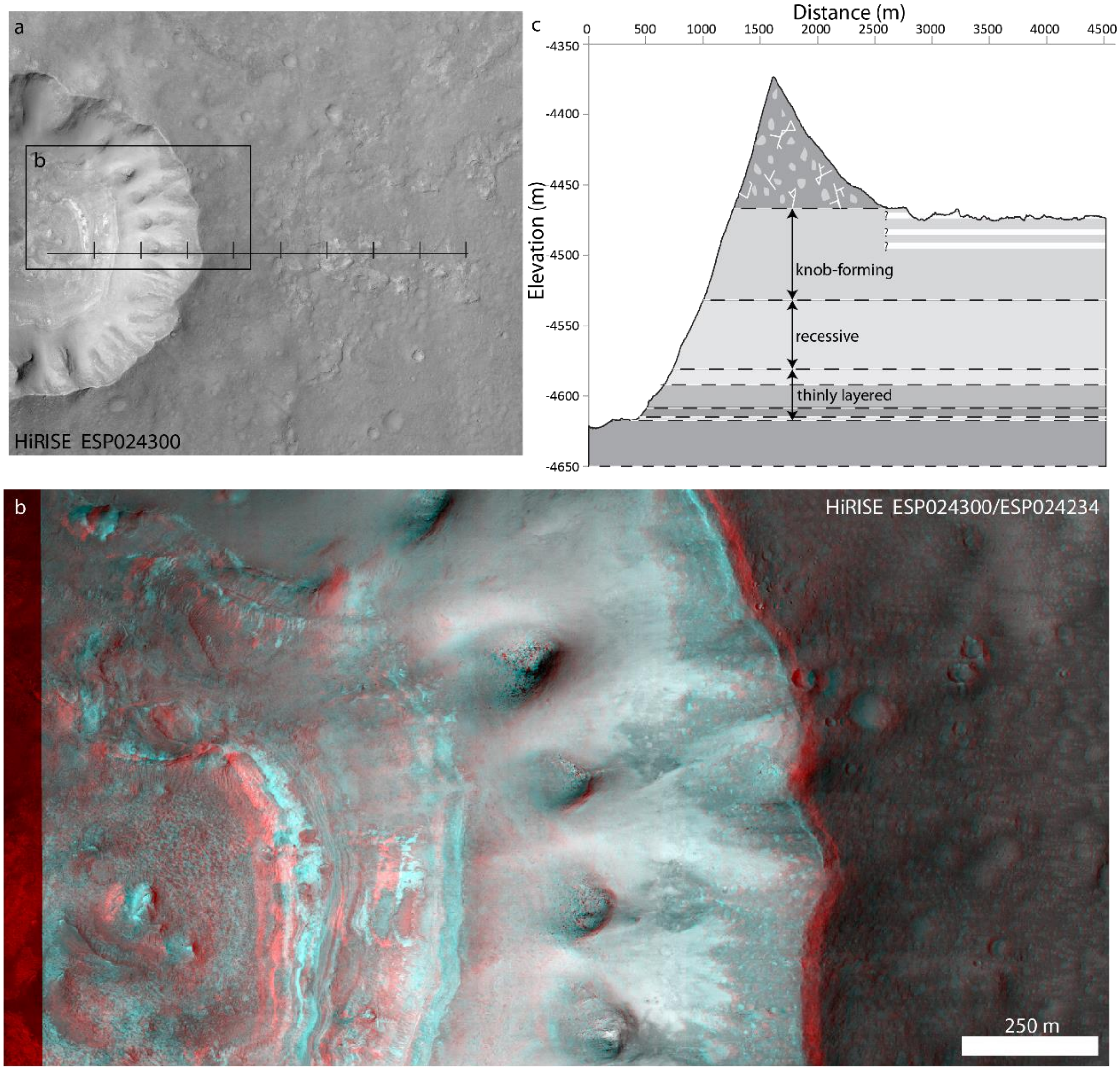

Figure 17 A ~4-km diameter fresh crater has impacted the northern Gale floor (see Figure 12 for context). A) The underlying stratigraphy is clearly seen on the crater walls in HiRISE ESP024300. East of the crater ejecta lie shallowly exposed light-toned deposits, which are indicated in C by horizontal white lines. B) HiRISE anaglyph of fresh crater. The bottom of the crater is layered, indicating that despite the crater's depth, sedimentary units are sampled; and the materials exposed by the crater do not reach the Gale basement. C) A HiRISE DEM permits estimating the bed thicknesses exposed within the crater, along the profile in A, assuming roughly horizontal bedding. The units observed have been used in our inferred sequence of events in Figure 20.

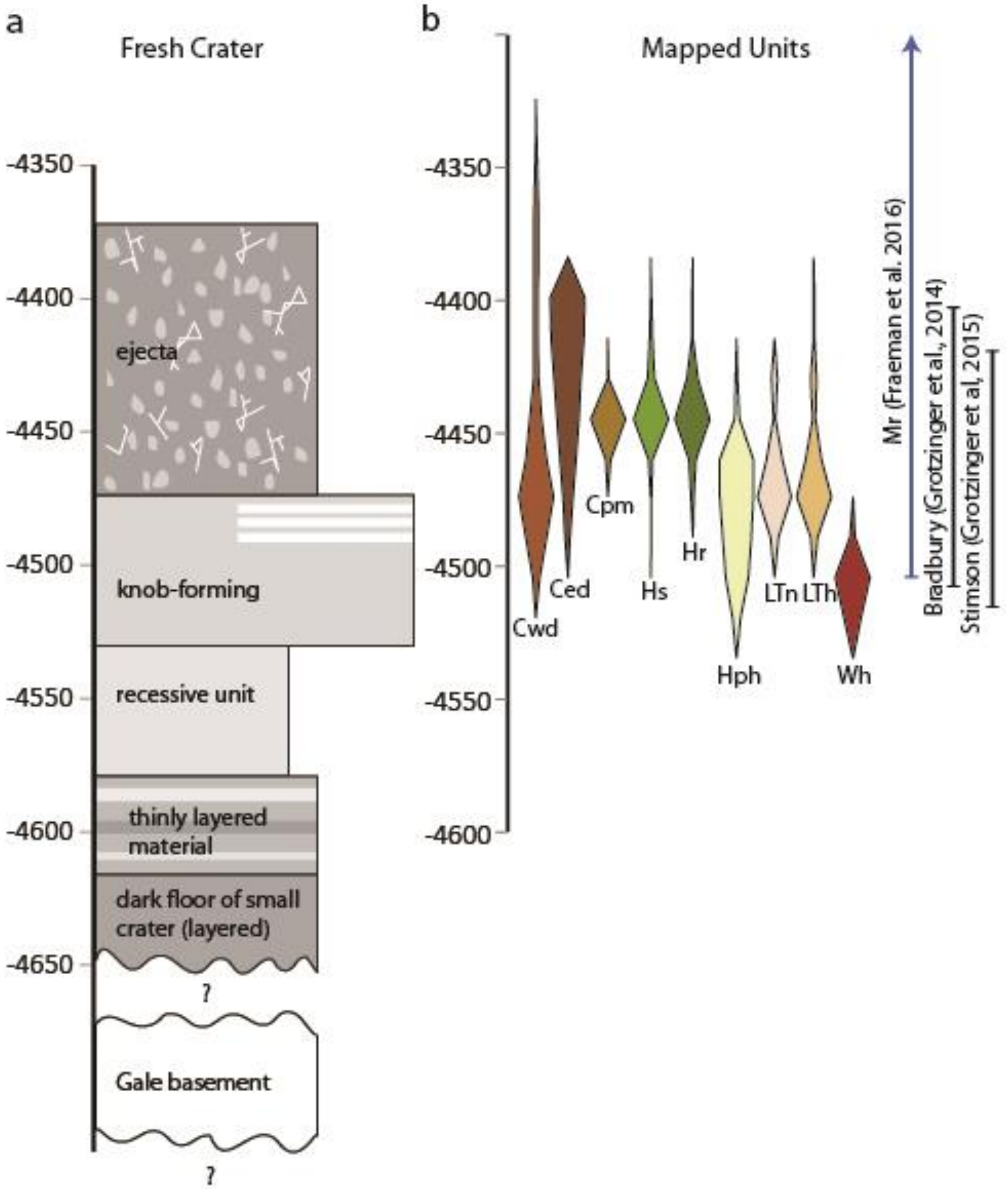

Figure 18 A) Stratigraphic column of the fresh crater in Figure 17. Using a HiRISE DEM (DTEEC ESP 024234 and ESP 024300), we are able to estimate the thickness of the units exposed in the walls. A coarse breccia with fracture fill is seen in the uppermost layers of the crater; the elevation profile indicates that this breccia is likely ejecta and/or impact-disrupted materials. Light-toned material crops out to the east of the crater, though does not appear to extend into the crater. An especially competent unit erodes into knobs along the wall of the crater; below it is a bland recessive unit. The lowermost units in the crater are finely layered with alternating light and dark bands. B) Elevation extents of a subset of the mapped units as well as the Murray unit as mapped in prior work [*Fraeman et al.*, 2016]. The elevation ranges observed in

the mapped units further demonstrate that the stratigraphy is complex, likely with multiple unconformities, as many of the units have overlapping vertical extents.

Rim rock outcrops also contain Fe/Mg phyllosilicates, seen most clearly in the boulder-rich upper reaches of Farah Vallis. However, the timing of phyllosilicate formation is ambiguous: alteration of the rim bedrock may pre-date Gale crater formation or have occurred any time thereafter. Materials lower down on the walls of Gale crater – either mass-wasted bedrock materials or overlying sediments– also have signatures of olivine and Fe/Mg phyllosilicates, sometimes found within the same pixels (e.g., image 9D8A; Figures 4 and 9).

There is notable variability in band center wavelength and strength in the absorptions related to hydration and hydroxylation. Units with 1.9-μm absorptions characteristic of hydrated minerals are seen in the crater ejecta from 1791F and also in eastern Gale. Units without the 1.9-μm absorption but with Fe/Mg-OH absorptions are present on the Gale floor (in scenes 28B4 and 1791F). Detections with both hydration and hydroxylation are seen primarily on the Gale wall/rim. There is significant variability in the exact band position for both the 1.4 μm and 2.3 μm absorptions (Figure 19). When comparing the band positions of these absorptions with that of library spectra, we observe that, overall, the absorptions mostly cluster near nontronite but that some spectra are more characteristic of Fe-saponites (Figure 19). Thus, the orbital data imply dioctahedral and trioctahedral phyllosilicates, varying in composition by location. Some of the olivine-bearing materials are also hydrated/hydroxylated, which could indicate their alteration by interaction with water.

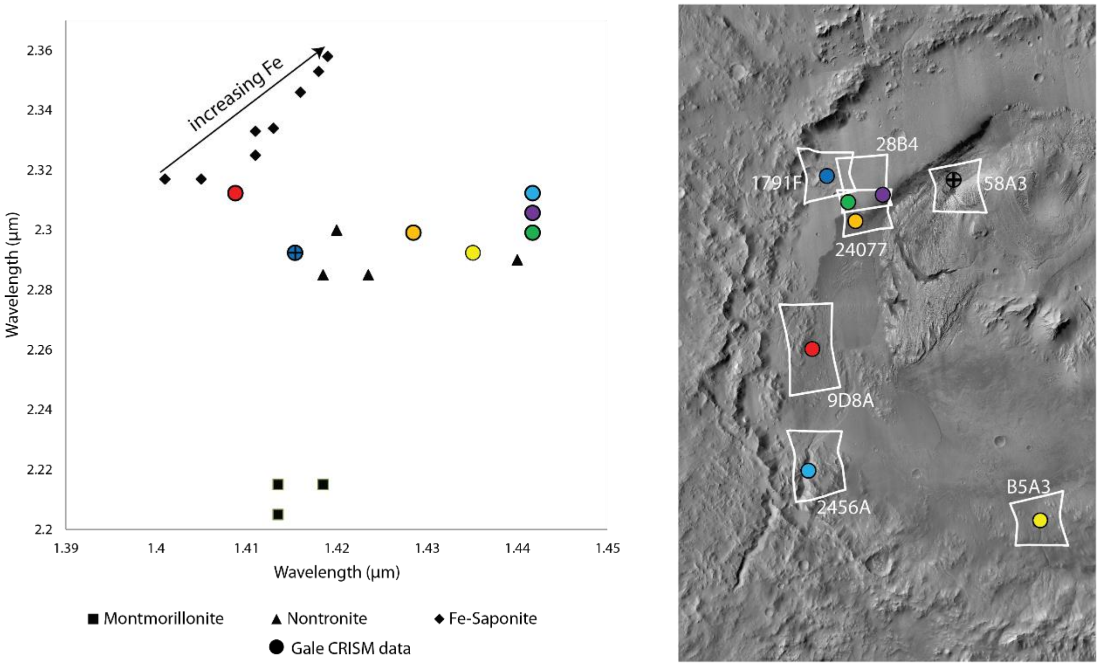

Figure 19 Plot of 1.4 and 2.3 μm band centers of our remote sensing observations and comparison with library spectra. Colored circles correspond to the CRISM images from Gale at right and band centers were computed from the spectra in Fig. 4. Library spectra were taken from the USGS spectral library [*Clark et al.*, 2007], RELAB spectra used in Michalski et al [2015] and Cuadros et al. [2013], as well as ferrous saponites measured in a Mars-like environment from Chemtob et al. [2015]. In the case of our detections, the shorter wavelength absorption is more

diagnostic of mineral composition since it has a broader range. The comparison indicates that we are likely observing phyllosilicates near the nontronite end of the smectite continuum.

5.2 Potential sulfates or zeolites on the eastern Gale rim

A novel finding of this work is the detection of materials with 1.92-µm and 2.48-µm absorption features in the eastern Gale rim rocks. Both absorptions are consistent with their cause being water (H_2O) in the mineral structure. Current spectral data do not permit a unique identification of the phase. One candidate for these detections are zeolite minerals, including calcium and sodium zeolites which have water-related absorptions in similar positions [*Cloutis et al.*, 2002]. Zeolite minerals have been previously found on Mars and represent low temperature hydrothermal fluid circulation or diagenesis in highly alkaline systems with peak temperatures < ~300° C [*Arkai et al.*, 2003; *Hay*, 2009; *Ehlmann et al.*, 2011]. A second possibility is sulfates. Spectra from the eastern rim are similar to, but not uniquely matched to, the hydrated calcium sulfate bassanite, which has also been detected by the Curiosity rover and which formed from diagenesis [*Vaniman et al.*, 2014]. When compared with the sulfates identified in Fraeman et al. [2016], the absorptions in the eastern rim rocks are similarly broad though appear at a shorter wavelength (Figure 5). Topography shows that the minerals on the eastern rim occur at an elevation that is ~2 km higher than those sulfates in the mound. Thus, these hydrated materials along the eastern Gale rim are intriguing but additional identified exposures will be required to determine their origin and relationship – if any – to sulfates in Mt. Sharp.

5.3 Gale walls as source for floor material

The rim and wall materials have certainly contributed to the floor sediments by ongoing erosion of Gale crater's walls. Some morphological features are clearly related to mass wasting, such as the landslides seen in CRISM scenes B5A3 and 2456A (Figures 7 and 8, respectively). Others are fluvial, such as inverted channels on the NW Gale floor (Figure 12) and Peace Vallis. Consistent with this observation, previous mapping has indicated that some of the floor deposits originated from bedrock channels incised into the crater walls (e.g., Le Deit et al. [2013]). The majority of the hydrated mineral detections in the rim and wall are within areas with apparent fluvial, alluvial, or mass wasting activity. In particular, recent landslides in scenes 2456A and B5A3 contain phyllosilicates. Watkins et al. [2015] previously studied the association between clays and landslides in Valles Marineris, suggesting that clays may facilitate landsliding, a conclusion which may be relevant to Gale. Alternatively, phyllosilicates may not cause or facilitate sliding but simply be best exposed in these deposits because they are more recent and less dust-covered.

Phyllosilicate mineral detections made on the wall and rim of Gale crater have absorptions in the 2.1-µm to 2.4-µm range, with the metal-OH band minima centered near 2.28-2.32 µm, suggesting Fe/Mg smectites, ranging from dioctahedral nontronite to trioctahedral saponite (Figures 4, 19). Some rim/wall rocks are Fe-saponite bearing, similar compositionally to the clay minerals detected at Yellowknife Bay. One simple scenario is that the materials transported to the Gale floor were already partially altered from the original protolith and that the clay minerals are mostly detrital, derived from the rim rocks. In this scenario, further transformation and mineral precipitation might then take place as diagenesis proceeded during burial (similar to the process hypothesized by Ehlmann and Buz [2015] and Schieber et al. [2017]). However, the similarities between the mineral assemblages detected orbitally and those detected by the rover and on the Gale floor do not require a common origin. A potential alternative scenario is that bedrock at each locality started with a similar mafic type composition and later underwent alteration due to local lacustrine or diagenetic aqueous activity (the original hypothesis for the Yellowknife Bay locality [*Vaniman et al.*, 2014; *Bristow et al.*, 2015]). In fact, textural studies of the Sheepbed mudstone at Yellowknife Bay indicate that the raised ridges [*Siebach et al.*, 2014] and nodules [*Stack et al.*, 2014] are of diagenetic origin. Furthermore, chemical analyses of the raised ridges show a composition similar to an Fe- or Mg- smectite [*Léveillé et al.*, 2014]. Both scenarios likely apply to rover-explored sedimentary rocks in different units, i.e., some clay minerals were transported from rim/wall units and some were formed *in situ*. Some may have also then been altered by burial diagenesis. The hydroxylated units on the floor might represent clay-bearing sedimentary units of either origin that were dehydrated then exhumed. However, importantly, the rim/wall and floor unit spectral signatures indicate distinct chemistries from the Al-nontronite detected from orbit in Mt. Sharp's phyllosilicate unit [Milliken et al. 2010; Fraeman et al., 2016]. This suggests either different protoliths or different water chemistries to explain the distinct clay chemistry between the units in the walls and floor and those in units yet-to-be-explored by the rover in Mt Sharp.

5.4 Potential lacustrine deposits and evidence for groundwater diagenesis

Many units in our study area share characteristics with the lacustrine or distal fluvial units traversed by the Curiosity [Grotzinger et al., 2014; 2015]. The strongest evidence for lacustrine sedimentary rocks is in the alternating light and dark layers found within the fresh crater from Figure 17, which mimic small-scale bedding sequences seen in sediments from lacustrine environments on Earth [*Bohacs et al.*, 2003]. At least 20 distinct thin layers are visible within a ~90-m sedimentary stack. The layered sediments in the fresh crater are also considerably more recessive in comparison with the knob-forming unit above them, which would be expected for less resistant materials such as siltstones or mudstones. Assuming roughly flat lying units such that elevation is a proxy for age, these lake deposits likely pre-date those investigated at Yellowknife Bay by the rover. The thinly layered materials of the fresh crater may be stratigraphically older facies, equivalents of the Murray and Sheepbed mudstones. This interpretation could be consistent with a long-lived lake whose shore receded away from the crater rim with time [*Grotzinger et al.*, 2015]. Alternatively, episodically present lakes where the depth fluctuated repeatedly might explain the thickness of the strata and the variation in properties in the layered sequence. The massive, comparatively more competent, knob-forming layer may represent a capping sandstone on these thinly layered deposits, in a similar manner to the capping units seen by the Curiosity rover [*Grotzinger et al.*, 2014; *Grotzinger et al.*, 2015]. Without *in situ* data on these strata and their decameter to millimeter-scale textures it is not possible to definitively discriminate between these scenarios.

The mapped floor units in NW Gale crater show a transition from readily eroded recessive units to competent, cliff-forming units. A similar pattern is also observed in the relatively fresh 4-km diameter crater walls (Figure 17), which transition from thinly layered material to knob forming materials. However, the materials exposed in the crater and floor units occur at different elevations. This may indicate that transitions of this style are episodic and have occurred multiple times. Lacustrine units potentially include the light-toned units (LTn and LTh) and the Hph polygonally fractured and hydroxylated hummocky unit. All three units are recessive, consistent with being comprised of easily eroded fine grained sedimentary rocks. They all underlie cliff-forming units similar to the knob-forming unit of the fresh crater. The hydroxylation in LTh and Hph is consistent with formation in or interaction with an aqueous environment. A final observation is the ≥m scale fracturing in the hummocky unit. If the sedimentary rocks are lacustrine, the fractures may have resulted from desiccation or freeze-thaw cycles. Alternative explanations for the fractures include unloading of previously buried material and weathering along fracture surfaces.

Regardless of the past extent of lakes on the Gale floor and their expression in these units, there is evidence for groundwater diagenesis. The polygonal ridges within the smooth depression (Ds) are consistent with mineralization along fractures by groundwater (Figure 16). Diagenetic alteration to form clay minerals within aeolian sandstones has been previously proposed to explain the spectral properties and corrugated appearance of the hydrated washboard unit [*Milliken et al.*, 2014].

5.5 Stratigraphically younger, spectrally bland, cliff-forming materials

A distinguishing feature of the cliff-forming units, when compared with other mapped floor units is their apparent spectral blandness, i.e., the lack of any electronic or vibrational absorptions to discriminate the units from a dusty or basaltic background suite of materials. Given the roughly homogeneous dust cover among all mapped units, there are at least three possible explanations for the unique lack of spectral features in the cliff-forming units: (1) under a scenario of mass wasting or fluvial/aeolian transport from the crater rim, the hydrated silicates and mafics may have become diluted and be present in abundances below the detection limit; (2) the absence of hydrated/hydroxylated phases could also be consistent with declining lacustrine and groundwater activity through time and/or inhibition of mineralization during any water-assisted deposition under drier, colder conditions; (3) in an airfall source scenario, the material may be spectrally bland (dust- or feldspar-rich). The first two scenarios are not mutually exclusive. Without additional evidence for an airfall scenario, we interpret these cliff-forming units as sandstones, possibly similar to rover-observed Bradbury and Stimson caprock units [*Williams et al.*, 2013; *Edgett et al.*, 2016]. Additionally, our mapped boundaries for the Ced eastern dark cliff-forming unit and the Cpm pock-marked cliff-forming unit are partially coincident with previous mapping of a cratered surface and rough terrain of Grotzinger et al. [*Grotzinger et al.*, 2014]. As with the rover-explored units, the observed diversity in cliff-forming morphology results from different dominant modes of deposition (aeolian vs. fluvial vs. mass wasting) or different styles of diagenesis.

5.6 Inferred Environmental History

We propose one potential formation scenario for the northern Gale floor, based on observations of the Gale rim rocks, floor sediments, and sedimentary rocks of the Murray formation explored by the Curiosity rover team (Figure 20). At the base of the sedimentary succession lies the Gale basement, an olivine-bearing suite of rocks impacted during Gale crater formation in the late Noachian/early Hesperian. Because the Gale basement is not exposed, it is unknown if anything lies between it and the lowest in elevation sedimentary unit observed, the thinly layered sedimentary rocks from the fresh crater in Figure 17. Regardless, sometime after crater formation, a 100-m thick succession of finely stratified sediments was deposited on the Gale floor, which we hypothesize were likely lake deposits. Concurrently or shortly thereafter, a series of hydrated and hydroxylated units were emplaced. The Hph hummocky unit is the most spatially extensive, containing dehydrated Fe/Mg phyllosilicates and showing a

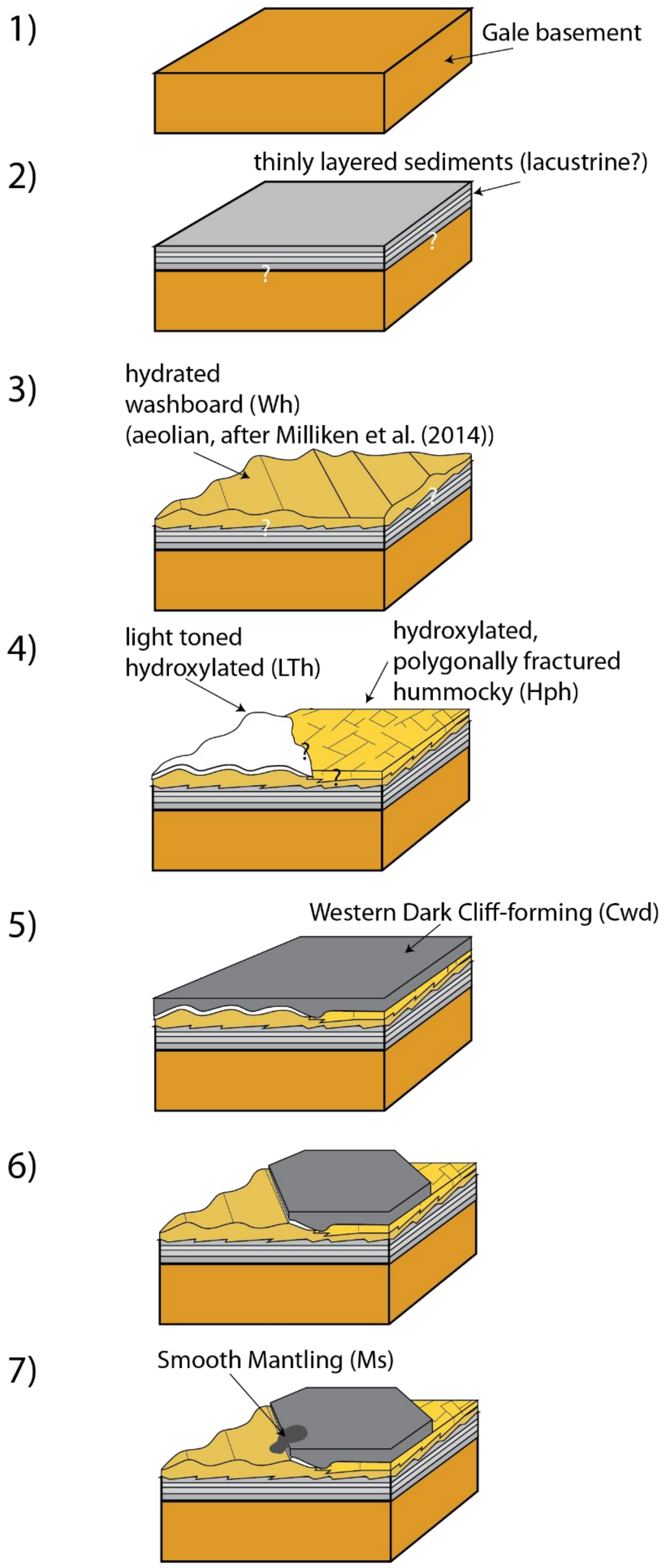
1)
Gale basement
2)
thinly layered sediments (lacustrine?)
?
?
3)
hydrated
washboard (Wh)
(aeolian, after Milliken et al. (2014))
?
?
4)
light toned
hydroxylated (LTh)
hydroxylated,
polygonally fractured
hummocky (Hph)
?
?
5)
Western Dark Cliff-forming (Cwd)
6)
7)
Smooth Mantling (Ms)

Figure 20 Schematic of the potential evolution of Gale crater floor sediments: 1) Gale crater is formed by a large impact, exposing basement rock (including potential impact melt sheets/impact-disrupted materials). 2) Sometime later, >100m of thinly layered sediments which alternate in brightness are deposited in extensive units on the paleofloor of Gale (as seen in the fresh crater from Figure 17). These may be the result of a lacustrine environment. The exact contact relationship between these sediments and the Gale basement floor is unknown (indicated by a white question mark). 3) Perhaps due to a shallowing of the water present in Gale and the emplacement of sand dunes (as originally interpreted by Milliken et al. [2014] to explain the washboard morphology), the hydrated washboard (Wh) and hydroxylated polygonally fractured unit (Hph) are formed above the sediments. Although there is no clear contact between Wh, Hph, and the thinly laminated sediments, the stratigraphy seen in the fresh crater from Figure 17 indicates that the former two likely overly the latter. The uncertainty is again indicated by white question marks. 4) A localized zone of a light toned hydroxylated material (LTh) is seen stratigraphically above Wh, formed, e.g., by evaporite deposition atop an aeolian unit as drawn here. The relationship between LTh and Hph, both of which are hydroxylated units, is obscured by a cap. The relationship between LTh and Wh may be related by sequential units in time: LTh as an alteration of the Wh or LTh as alteration at the base of the overlying spectrally bland cliff-forming unit. 5) A spectrally bland and extensive cliff-forming unit (Cwd) covers Wh, LTh, and Hph. This unit is competent and may represent a sandstone, fluvially-facilitated mass wasting from the crater wall, or emplacement of an airfall deposit. 6) Erosion carves the cliff-forming unit back revealing the underlying sandstone and polygonally fractured unit. 7) A spectrally bland mantling unit (Ms) partially covers Cwd, LTh, and Wh.

polygonally fractured morphology. The washboard unit (Wh) has hydrated Fe/Mg phyllosilicates associated with paleo-aeolian deposits [*Milliken et al.*, 2014] and occupies a similar elevation range to the Hph hummocky unit and similar stratigraphic position, beneath a cliff-forming unit (Figure 18). If the Hph hummocky and Wh washboard units are from a lacustrine or perilacustrine environments, one possible chronology may be a time-equivalent lateral transition from lake sediments to mud flats then to sand dunes. Small exposures of light-toned hydroxylated materials (LTh) are exposed stratigraphically above the washboard only; a contact relationship with the hummocky unit is not observed. The spectral similarities between the polygonally fractured hummocky unit (Hph) and the LTh hydroxylated light toned deposits may indicate that the two units are closely related or perhaps that LTh is the thin distal portion of the hummocky unit (though does not share the same polygonal fracturing).

The transition from the hydrated washboard to the hydroxylated light-toned unit and then to the spectrally bland Cwd cliff-forming unit could have resulted from a variety of scenarios. Three plausible explanations for this sequence are (1) The LTh light-toned unit is the alteration product of the washboard unit; (2) The LTh light-toned unit is a separate unit from the Wh washboard and Cwd cliff-forming units, or (3) The LTh light-toned unit is the alteration product of the Cwd cliff-forming unit. One environmental scenario that may explain the sequence is a series of shallow lakes with relatively drier intervals (forming aeolian units) and wetter intervals (leaving light-toned polygonally fractured fine-grained sedimentary deposits upon evaporation). Aeolian units may have been cemented by minerals precipitated during groundwater upwelling. Lacustrine units explored by the Curiosity rover show abundant evidence for multiple episodes of diagenetic alteration [*Grotzinger et al.*, 2014; *Nachon et al.*, 2014; *Kah*, 2015; *Kronyak et al.*, 2015]. Following the major water-related events the spectrally bland cliff-forming units were emplaced and then later eroded leaving the landscapes seen today. Some more recent mantling and crater ejecta material has been emplaced in discrete locations superposing sequences of stratigraphic units (such as in Figure 14b).

All data from orbit are consistent with the scenario outlined above; nevertheless, confirmation of this would require viewing the context and textures at sub-m or sub-cm resolution. Evidence for environmental scenarios that we propose might be found in the units that lie ahead in the Curiosity rover traverse.

6.0 Conclusions

The following are the key findings from our joint analysis of the Gale crater rim, wall, and floor units, which used CRISM and THEMIS spectroscopic data and high resolution imagery, coupled with geologic mapping:

- Extensive olivine- and Fe/Mg phyllosilicate-bearing materials were identified in the Gale wall, rim, and floor. No distinctly felsic materials were found, though detection capabilities are diminished by image artifacts and dust cover.
- The Mt. Sharp Fe/Al phyllosilicates are spectrally distinct from the Fe/Mg phyllosilicates observed on the wall, rim, and floor of Gale crater from orbit
- Some of the floor phyllosilicates, including those observed at Yellowknife Bay by MSL may be in part detrital with already altered sediments (olivine altered to Fe/Mg smectite) having been transported to the Gale floor. Alternative scenarios involve widespread alteration of rim and wall rocks and floor sediments by waters of similar chemistry.
- Sedimentary deposits within Gale crater near the rover landing site are >250 m thick and include a ~90-m thick succession of thinly layered sediments, possibly formed in an ancient lake(s). Relative to the units observed with Curiosity (Grotzinger et al 2014; 2015) these findings extend the stratigraphic record of lake(s) within Gale crater.
- Stratigraphic relationships between floor units with different characteristics may indicate alternating aeolian and lacustrine environments with different amounts of surface or groundwater. Contemporaneous lateral variations as well as possible multiple arid/wet cycles may have produced the observed sequences.
- Cliff-forming units on top of the floor strata have no evidence for hydrated minerals, may postdate the most water-rich periods, and may be similar to the sandstones observed with the Curiosity rover.
- Dramatic representations of recent and/or ongoing erosion, including landsliding, are observed on the Gale rim and walls.

The source of the feldspar rich lithologies observed by the Curiosity rover still remains a mystery. Targeted CRISM data over more of the Gale rim and wall will be the best source of new data to continue the search for Fe-bearing feldspars and additional minerals. Additional spectral analysis, including use of oversampled data and new noise reduction techniques may help elucidate the relationship between the floor and wall/rim lithologies. Supplementary HiRISE imagery will allow for more stratigraphic relationships to be determined and may allow further characterization of the units identified on the floor.

7.0 Acknowledgements

All data used in this paper are available in the NASA Planetary Data System; derived products are available by request. Thanks to the efforts of the many spacecraft and instrument teams for their collection of these right datasets. Thanks to Ara Oshagan, Christopher Edwards, and Daven Quinn for assistance with data processing. J.B. was supported by a NASA Earth &

Space Sciences Fellowship for the conduct of this work. Partial support was also provided by an MSL Participating Scientist grant to B.L.E. We also thank Sanjeev Gupta and an anonymous reviewer for their comments and suggestions, which have improved this manuscript.

9.0 References

Anderson, R., and J. Bell (2010), Geologic mapping and characterization of Gale Crater and implications for its potential as a Mars Science Laboratory landing site *Mars* 576-128, doi:10.1555/mars.2010.0004.

Arkai, P., F. Sassi, and J. Desmons (2003), A systematic nomenclature for metamorphic rocks. 5. Very low-to low-grade metamorphic rocks, *Recommendations by the IUGS Subcommission on the systematics of metamorphic rocks.*

Bandfield, J., D. Rogers, M. Smith, and P. Christensen (2004), Atmospheric correction and surface spectral unit mapping using Thermal Emission Imaging System data, *J. Geophys. Res.*, 109.

Bandfield, J. L. (2009), Effects of surface roughness and graybody emissivity on martian thermal infrared spectra, *Icarus*, 202, 414-428, doi:10.1016/j.icarus.2009.03.031.

Bandfield, J. L., E. S. Amador, and N. H. Thomas (2013), Extensive hydrated silica materials in western Hellas Basin, Mars, *Icarus*, 226, 1489-1498, doi:10.1016/j.icarus.2013.08.005.

Bandfield, J. L., V. E. Hamilton, and P. R. Christensen (2000), A Global View of Martian Surface Compositions from MGS-TES, *Science*, 287, 1626-1630, doi:10.1126/science.287.5458.1626.

Banham, S. G., S. Gupta, D. M. Rubin, J. A. Watkins, D. Sumner, J. Grotzinger, K. W. Lewis, K. S. Edgett, L. A. Edgar, and K. M. Stack (2016), Reconstruction of an Ancient Eolian Dune Field at Gale Crater, Mars: Sedimentary Analysis of the Stimson Formation, *paper presented at LPSC*, 2346, LPI Contributions, The Woodlands, Texas.

Bish, D. L., D. Blake, D. Vaniman, S. Chipera, R. Morris, D. Ming, A. Treiman, P. Sarrazin, S. Morrison, and R. Downs (2013), X-ray diffraction results from Mars Science Laboratory: Mineralogy of Rocknest at Gale crater, *Science*, 341, doi:10.1126/science.1238932.

Bishop, J., J. Madejova, P. Komadel, and H. Froschil (2002), The influence of structural Fe, Al, and Mg on the infrared OH bands in spectra of dioctahedral smectites, *Clay Minerals*, 37, 607-616, doi:10.1180/0009855023740063.

Bishop, J. L., E. Z. N. Dobrea, N. K. McKeown, M. Parente, B. L. Ehlmann, J. R. Michalski, R. E. Milliken, F. Poulet, G. A. Swayze, and J. F. Mustard (2008), Phyllosilicate diversity and past aqueous activity revealed at Mawrth Vallis, Mars, *Science*, 321, 830-833, doi:10.1126/science.1159699

Bishop, J. L., E. Murad, and M. D. Dyar (2015), Akaganéite and schwertmannite: Spectral properties and geochemical implications of their possible presence on Mars, *American Mineralogist*, 100, 738-746, doi:10.2138/am-2015-5016.

Blake, D. F., R. Morris, G. Kocurek, S. Morrison, R. Downs, D. Bish, D. Ming, K. Edgett, D. Rubin, and W. Goetz (2013), Curiosity at Gale crater, Mars: Characterization and analysis of the Rocknest sand shadow, *Science*, 341, doi:10.1126/science.1239505

Bohacs, K. M., A. R. Carrol, and J. E. Neal (2003), Lessons from large lake systems- Thresholds, nonlinearity, and strange attractors, *Geological Society of America Special Paper*75-90.

Bristow, T., et al. (2015), The origin and implications of clay minerals from Yellowknife Bay, Gale crater, Mars, *American Mineralogist*, 100, 824-836, doi:10.2138/am-2015-5077CCBYNCND.

Cabrol, N. A., E. A. Grin, H. E. Newsom, R. Landheim, and C. P. McKay (1999), Hydrogeologic evolution of Gale Crater and its relevance to the exobiological exploration of Mars, *Icarus*, 139, 235-245, doi:10.1006/icar.1999.6099.

Carter, J., C. Viviano-Beck, D. Loizeau, J. Bishop, and L. Le Deit (2015), Orbital detection and implications of akaganéite on Mars, *Icarus*, 253, 296-310, doi:10.1016/j.icarus.2015.01.020.

Chemtob, S. M., R. D. Nickerson, R. V. Morris, D. G. Agresti, and J. G. Catalano (2015), Synthesis and structural characterization of ferrous trioctahedral smectites: Implications for clay mineral genesis and detectability on Mars, *J. Geophys. Res.*, 120, 1119-1140, doi:10.1002/2014JE004763.

Christensen, P. R., B. M. Jakosky, H. H. Kieffer, M. C. Malin, H. Y. McSween Jr, K. Nealson, G. L. Mehall, S. H. Silverman, S. Ferry, and M. Caplinger (2004), The thermal emission imaging system (THEMIS) for the Mars 2001 Odyssey Mission, *Space Sci. Rev.*, 110, 85-130, doi:10.1023/B:SPAC.0000021008.16305.94.

Christensen, P. R., et al. (2005), Evidence for magmatic evolution and diversity on Mars from infrared observations, *Nature*, 436, 504-509, doi:10.1038/nature03639.

Clark, R. N., T. V. V. King, M. Klejwa, G. A. Swayze, and N. Vergo (1990), High spectral resolution reflectance spectroscopy of minerals, *J. Geophys. Res.*, 95, 12653-12680, doi:10.1029/JB095iB08p12653.

Clark, R. N., G. A. Swayze, R. Wise, K. E. Livo, T. M. Hoefen, R. F. Kokaly, and S. J. Sutley (2007), USGS digital spectral library splib06a, US Geological Survey Reston, VA.

Cloutis, E. A., P. M. Asher, and S. A. Mertzman (2002), Spectral reflectance properties of zeolites and remote sensing implications*, J. Geophys. Res.*, 107, doi:10.1029/2000JE001467.

Cuadros, J., J. R. Michalski, V. Dekov, J. Bishop, S. Fiore, and M. D. Dyar (2013), Crystal-chemistry of interstratified Mg/Fe-clay minerals from seafloor hydrothermal sites, *Chemical Geology*, 360–361, 142-158, doi:http://dx.doi.org/10.1016/j.chemgeo.2013.10.016.

Edgett, K. S., et al. (2016), Recent Observations by Curiosity's Mars Hand Lens Imager (MAHLI) of Rock Strata and Eolian Sediment on the Lower North Slope of Aeolis Mons, Gale

Crater, Mars, *paper presented at LPSC*, 1382, LPI Contributions, The Woodlands, TX, March 1, 2016.

Ehlmann, B. L., and J. Buz (2015), Mineralogy and Fluvial History of the Watersheds of Gale, Knobel, and Sharp craters: A Regional Context for MSL Curiosity's Exploration, *Geophys. Res. Lett.*, doi:10.1002/2014GL062553.

Ehlmann, B. L., J. F. Mustard, R. N. Clark, G. A. Swayze, and S. L. Murchie (2011), Evidence for low-grade metamorphism, hydrothermal alteration, and diagenesis on Mars from phyllosilicate mineral assemblages, *Clays and Clay Minerals*, 59, 359-377, doi:10.1346/ccmn.2011.0590402.

Ehlmann, B. L., J. F. Mustard, G. A. Swayze, R. N. Clark, J. L. Bishop, F. Poulet, D. J. Des Marais, L. H. Roach, R. E. Milliken, and J. J. Wray (2009), Identification of hydrated silicate minerals on Mars using MRO-CRISM: Geologic context near Nili Fossae and implications for aqueous alteration, *J. Geophys. Res.,* 114, doi:10.1029/2009JE003339.

Fassett, C. I., and J. W. I. Head (2008), The timing of martian valley network activity: Constraints from buffered crater counting, *Icarus*, 195, 61-89, doi:10.1016/j.icarus.2007.12.009.

Fraeman, A., R. Arvidson, J. Catalano, J. Grotzinger, R. Morris, S. Murchie, K. Stack, D. Humm, J. McGovern, and F. Seelos (2013), A hematite-bearing layer in Gale Crater, Mars: Mapping and implications for past aqueous conditions, *Geology*, 41, 1103-1106, doi:10.1130/G34613.1.

Fraeman, A. A., B. L. Ehlmann, R. E. Arvidson, C. S. Edwards, J. P. Grotzinger, R. E. Milliken, D. P. Quinn, and M. S. Rice (2016), The Stratigraphy and Evolution of Lower Mt. Sharp from Spectral, Morphological, and Thermophysical Orbital Datasets, *J. Geophys. Res.*, doi:10.1002/2016JE005095.

Grant, J. A., S. A. Wilson, N. Mangold, F. Calef, and J. P. Grotzinger (2014), The timing of alluvial activity in Gale crater, Mars, *Geophys. Res. Lett.*, 41, doi:10.1002/2013GL058909.

Grotzinger, J. P., J. Crisp, A. R. Vasavada, R. C. Anderson, C. J. Baker, R. Barry, D. F. Blake, P. Conrad, K. S. Edgett, and B. Ferdowski (2012), Mars Science Laboratory mission and science investigation, *Space Sci. Rev.*, 170, 5-56, doi:10.1007/s11214-012-9892-2.

Grotzinger, J. P., et al. (2015), Deposition, exhumation, and paleoclimate of an ancient lake deposit, Gale crater, Mars, *Science,* 350, doi:10.1126/science.aac7575.

Grotzinger, J. P., et al. (2014), A Habitable Fluvio-Lacustrine Environment at Yellowknife Bay, Gale Crater, Mars, *Science*, 343, doi:10.1126/science.1242777.

Hay, R. (2009), Geologic occurrence of zeolites and some associated minerals, *Pure and Applied Chemistry*, 58, 1339-1342, doi:10.1351/pac198658101339.

Irwin, R. P., A. D. Howard, R. A. Craddock, and J. M. Moore (2005), An intense terminal epoch of widespread fluvial activity on early Mars: 2. Increased runoff and paleolake development, *J. Geophys. Res.*, 110, E12S15, doi:10.1029/2005JE002460.

Kah, L. C. (2015), Late Diagenetic Cements in the Murray Formation, Gale Crater, Mars: Implications for Postdepositional Fluid Flow, *paper presented at AGU Fall Meeting*, 73614, San Fransisco, CA.

Kite, E. S., I. Halevy, M. A. Kahre, M. J. Wolff, and M. Manga (2013a), Seasonal melting and the formation of sedimentary rocks on Mars, with predictions for the Gale Crater mound, *Icarus*, 223, 181-210, doi:10.1016/j.icarus.2012.11.034.

Kite, E. S., K. W. Lewis, M. P. Lamb, C. E. Newman, and M. I. Richardson (2013b), Growth and form of the mound in Gale Crater, Mars: Slope wind enhanced erosion and transport, *Geology*, 41, 543-546, doi:10.1130/G33909.1

Kreisch, C., R. Arvidson, J. O'Sullivan, K. Li, D. Politte, J. Finkel, E. Guinness, N. Stein, and A. Fraeman (2015), Log-Likelihood Method of Reducing Noise in CRISM Along-Track Oversampled Hyperspectral Images, *paper presented at Computational Optical Sensing and Imaging*, Arlington, VA.

Kronyak, R. E., L. C. Kah, D. Blaney, D. Sumner, M. Fisk, W. Rapin, M. Nachon, N. Mangold, J. Grotzinger, and R. C. Wiens (2015), Garden City Vein Complex, Gale Crater, Mars: Implications for Late Diagenetic Fluid Flow, *paper presented at AGU Fall Meeting*, 73835, San Fransisco, CA.

Lane, M. D., and P. R. Christensen (2013), Determining olivine composition of basaltic dunes in Gale Crater, Mars, from orbit: Awaiting ground truth from Curiosity, *Geophys. Res. Lett.*, 40, 3517-3521, doi:10.1002/grl.50621.

Lapotre, M. G. A., B. L. Ehlmann, S. E. Minson, R. E. Arvidson, F. Ayoub, A. A. Fraeman, R. C. Ewing, and N. T. Bridges (2017), Compositional Variations in Sands of the Bagnold Dunes, Gale Crater, Mars, from Visible-Shortwave Infrared Spectroscopy and Comparison to Ground-Truth from the Curiosity Rover, *J. Geophys. Res.*, 122, 2489–2509, doi:10.1002/2016JE005133.

Le Deit, L., E. Hauber, F. Fueten, M. Pondrelli, A. P. Rossi, and R. Jaumann (2013), Sequence of infilling events in Gale crater, Mars: Results from morphology, stratigraphy, and mineralogy, *J. Geophys. Res.*, 118, 2439-2473, doi:10.1002/2012JE004322.

Léveillé, R. J., et al. (2014), Chemistry of fracture-filling raised ridges in Yellowknife Bay, Gale Crater: Window into past aqueous activity and habitability on Mars, *J. Geophys. Res.*, 119, 2398-2415, doi:10.1002/2014JE004620.

Malin, M. C., et al. (2007), Context Camera Investigation on board the Mars Reconnaissance Orbiter, *J. Geophys. Res.*, 112, doi:10.1029/2006JE002808.

Malin, M. C., and K. S. Edgett (2000), Sedimentary rocks of early Mars, Science, 290, 1927-1937, doi:10.1126/science.290.5498.1927

McEwen, A. S., et al. (2007), Mars Reconnaissance Orbiter's High Resolution Imaging Science Experiment (HiRISE), *J. Geophys. Res.*, 112, E05S02, doi:10.1029/2005JE002605.

McLennan, S. M., et al. (2014), Elemental Geochemistry of Sedimentary Rocks at Yellowknife Bay, Gale Crater, Mars, *Science*, 343, doi:10.1126/science.1244734.

Michalski, J. R., J. Cuadros, J. L. Bishop, M. Darby Dyar, V. Dekov, and S. Fiore (2015), Constraints on the crystal-chemistry of Fe/Mg-rich smectitic clays on Mars and links to global alteration trends, *Earth Planet. Sci. Lett.*, 427, 215-225, doi:10.1016/j.epsl.2015.06.020.

Milliken, R., J. Grotzinger, and B. Thomson (2010), Paleoclimate of Mars as captured by the stratigraphic record in Gale Crater, *Geophys. Res. Lett.*, 37, doi:10.1016/j.epsl.2015.06.020.

Milliken, R. E., R. C. Ewing, W. W. Fischer, and J. Hurowitz (2014), Wind-blown sandstones cemented by sulfate and clay minerals in Gale Crater, Mars, *Geophys. Res. Lett.*, 41, doi:10.1002/2013GL059097.

Morgan, F., F. Seelos, S. Murchie, and C. Team (2009), CAT tutorial, *paper presented at CRISM Data User's Workshop*, Houston, TX.

Murchie, S., et al. (2007), Compact Reconnaissance Imaging Spectrometer for Mars (CRISM) on Mars Reconnaissance Orbiter (MRO), *J. Geophys. Res.*, 112, E05S03, doi:10.1029/2006JE002682.

Murchie, S. L., F. P. Seelos, C. D. Hash, D. C. Humm, E. Malaret, J. A. McGovern, T. H. Choo, K. D. Seelos, D. L. Buczkowski, and M. F. Morgan (2009), Compact Reconnaissance Imaging Spectrometer for Mars investigation and data set from the Mars Reconnaissance Orbiter's primary science phase, *J. Geophys. Res.*, 114, E00D07, doi:10.1029/2009JE003344.

Nachon, M., et al. (2014), Calcium sulfate veins characterized by ChemCam/Curiosity at Gale crater, Mars, *J. Geophys. Res.*, 119, 1991-2016, doi:10.1002/2013JE004588.

Osterloo, M. M., F. S. Anderson, V. E. Hamilton, and B. M. Hynek (2010), Geologic context of proposed chloride-bearing materials on Mars, *J. Geophys. Res.*, 115, doi:10.1029/2010JE003613.

Palucis, M. C., W. E. Dietrich, R. M. E. Williams, A. G. Hayes, T. Parker, D. Y. Sumner, N. Mangold, K. Lewis, and H. Newsom (2016), Sequence and relative timing of large lakes in Gale crater (Mars) after the formation of Mount Sharp, *J. Geophys. Res.*, 121, 472-496, doi:10.1002/2015JE004905.

Pan, L., B. L. Ehlmann, J. Carter, and C. M. Ernst (2015), Probing Mars' Northern Plains Stratigraphy with Impact Craters, *paper presented at LPSC*, 2583, LPI Contributions, The Woodlands, TX.

Pelkey, S., J. Mustard, S. Murchie, R. Clancy, M. Wolff, M. Smith, R. Milliken, J. P. Bibring, A. Gendrin, and F. Poulet (2007), CRISM multispectral summary products: Parameterizing mineral diversity on Mars from reflectance, *J. Geophys. Res.*, 112, E08S14, doi:10.1029/2006JE002831.

Pelkey, S. M., and B. M. Jakosky (2002), Surficial geologic surveys of Gale Crater and Melas Chasma, Mars: Integration of remote-sensing data, *Icarus*, 160, 228-257, doi:10.1006/icar.2002.6978.

Pelkey, S. M., B. M. Jakosky, and P. R. Christensen (2004), Surficial properties in Gale crater, Mars, from Mars Odyssey THEMIS data, *Icarus*, 167, 244-270, doi:10.1016/j.icarus.2003.09.013.

Poulet, F., J. Carter, J. L. Bishop, D. Loizeau, and S. M. Murchie (2014), Mineral abundances at the final four curiosity study sites and implications for their formation, *Icarus*, 231, 65-76, doi:10.1016/j.icarus.2013.11.023.

Rogers, A. D., and J. L. Bandfield (2009), Mineralogical characterization of Mars Science Laboratory candidate landing sites from THEMIS and TES data, *Icarus*, 203, 437-453, doi:10.1016/j.icarus.2009.04.020.

Rogers, A. D., and P. R. Christensen (2007), Surface mineralogy of Martian low-albedo regions from MGS-TES data: Implications for upper crustal evolution and surface alteration, *J. Geophys. Res.*, 112, doi:10.1029/2006JE002727.

Rogers, A. D., P. R. Christensen, and J. L. Bandfield (2005), Compositional heterogeneity of the ancient Martian crust: Analysis of Ares Vallis bedrock with THEMIS and TES data, *J. Geophys. Res.*, 110, doi:10.1029/2005JE002399.

Rogers, A. D., and R. L. Fergason (2011), Regional-scale stratigraphy of surface units in Tyrrhena and Iapygia Terrae, Mars: Insights into highland crustal evolution and alteration history, *J. Geophys. Res.*, 116, doi:10.1029/2010JE003772.

Sautter, V., C. Fabre, O. Forni, M. Toplis, A. Cousin, A. Ollila, P. Meslin, S. Maurice, R. Wiens, and D. Baratoux (2014), Igneous mineralogy at Bradbury Rise: The first ChemCam campaign at Gale crater, *J. Geophys. Res.*, doi:10.1002/2013JE004472.

Schieber, J., D. Bish, M. Coleman, M. Reed, E. M. Hausrath, J. Cosgrove, S. Gupta, M. E. Minitti, K. S. Edgett, and M. Malin (2017), Encounters with an unearthly mudstone: Understanding the first mudstone found on Mars, *Sedimentology*, 64, 311-358, doi:10.1111/sed.12318.

Schmidt, M. E., et al. (2014), Geochemical diversity in first rocks examined by the Curiosity Rover in Gale Crater: Evidence for and significance of an alkali and volatile-rich igneous source, *J. Geophys. Res.*, 119, doi:10.1002/2013JE004481.

Seelos, K. D., F. P. Seelos, C. E. Viviano-Beck, S. L. Murchie, R. E. Arvidson, B. L. Ehlmann, and A. A. Fraeman (2014), Mineralogy of the MSL Curiosity landing site in Gale crater as observed by MRO/CRISM, *Geophys. Res. Lett.*, 41, 4880-4887, doi:10.1002/2014GL060310.

Siebach, K. L., M. B. Baker, J. P. Grotzinger, S. M. McLennan, R. Gellert, L. M. Thompson, and J. A. Hurowitz (2017), Sorting out Compositional Trends in Sedimentary Rocks of the Bradbury Group (Aeolus Palus), Gale Crater, Mars, *J. Geophys. Res.*, doi:10.1002/2016JE005195.

Siebach, K. L., and J. P. Grotzinger (2014), Volumetric estimates of ancient water on Mount Sharp based on boxwork deposits, Gale Crater, Mars, *J. Geophys. Res.*, 119, 189-198, doi:10.1002/2013JE004508.

Siebach, K. L., J. P. Grotzinger, L. C. Kah, K. M. Stack, M. Malin, R. Léveillé, and D. Y. Sumner (2014), Subaqueous shrinkage cracks in the Sheepbed mudstone: Implications for early fluid diagenesis, Gale crater, Mars, *J. Geophys. Res.*, 119, 1597-1613, doi:10.1002/2014JE004623.

Stack, K. M., et al. (2014), Diagenetic origin of nodules in the Sheepbed member, Yellowknife Bay formation, Gale crater, Mars, *J. Geophys. Res.*, 119, 1637-1664, doi:10.1002/2014JE004617.

Stolper, E. M., et al. (2013), The Petrochemistry of Jake_M: A Martian Mugearite, *Science*, 341, doi:10.1126/science.1239463.

Sunshine, J. M., and C. M. Pieters (1998), Determining the composition of olivine from reflectance spectroscopy, *J. Geophys. Res.*, 103, 13675-13688, doi:10.1029/98JE01217.

Szabo, T., G. Domokos, J. P. Grotzinger, and D. J. Jerolmack (2015), Reconstructing the transport history of pebbles on Mars, *Nature Communincations*, 6, doi:10.1038/ncomms9366.

Taylor, G. J., W. V. Boynton, S. M. McLennan, and L. M. V. Martel (2010), K and Cl concentrations on the Martian surface determined by the Mars Odyssey Gamma Ray Spectrometer: Implications for bulk halogen abundances in Mars, *Geophys. Res. Lett.*, 37, doi:10.1029/2010GL043528.

Thompson, L., R. Gellert, J. G. Spray, L. C. Kah, and M. S. Team (2015), The composition of the basal murray formation at Pahrump Hills, Gale Crater, Mars *paper presented at LPSC*, 1429, LPI Contributions, The Woodlands, TX.

Thomson, B., N. Bridges, R. Milliken, A. Baldridge, S. Hook, J. Crowley, G. Marion, C. de Souza Filho, A. Brown, and C. Weitz (2011), Constraints on the origin and evolution of the layered mound in Gale Crater, Mars using Mars Reconnaissance Orbiter data, *Icarus*, 214, 413-432, doi:10.1016/j.icarus.2011.05.002.

Treiman, A. H., et al. (2016), Mineralogy, provenance, and diagenesis of a potassic basaltic sandstone on Mars: CheMin X-ray diffraction of the Windjana sample (Kimberley area, Gale Crater), *J. Geophys. Res.*, 121, 75-106, doi:10.1002/2015JE004932.

Vaniman, D., D. Bish, D. Ming, T. Bristow, R. Morris, D. Blake, S. Chipera, S. Morrison, A. Treiman, and E. Rampe (2014), Mineralogy of a mudstone at Yellowknife Bay, Gale crater, Mars, *Science*, 343, doi:10.1126/science.1243480.

Viviano-Beck, C. E., et al. (2014), Revised CRISM spectral parameters and summary products based on the currently detected mineral diversity on Mars, *J. Geophys. Res.*, 119, 1403-1431, doi:10.1002/2014JE004627.

Watkins, J. A., B. L. Ehlmann, and A. Yin (2015), Long-runout landslides and the long-lasting effects of early water activity on Mars, *Geology*, 43, 107-110, doi:10.1130/g36215.1.

Williams, R. M. E., et al. (2013), Martian Fluvial Conglomerates at Gale Crater, *Science*, 340, 1068-1072, doi:10.1126/science.1237317.

Wiseman, S. M., R. E. Arvidson, R. V. Morris, F. Poulet, J. C. Andrews-Hanna, J. L. Bishop, S. L. Murchie, F. P. Seelos, D. Des Marais, and J. L. Griffes (2010), Spectral and stratigraphic mapping of hydrated sulfate and phyllosilicate-bearing deposits in northern Sinus Meridiani, Mars, *J. Geophys. Res.*, 115, E00D18, doi:10.1029/2009JE003354.

Wray, J. J. (2013), Gale crater: the Mars Science Laboratory/Curiosity Rover Landing Site, *Int. J. Astrobio.*, 12, 25-38, doi:10.1017/S1473550412000328.

Chapter 3

PHOTOMETRIC CHARACTERIZATION OF LUCIDEON AND AVIAN TECHNOLOGIES COLOR STANDARDS: APPLICATION FOR CALIBRATION OF THE MASTCAM-Z INSTRUMENT ON THE MARS 2020 ROVER

Jennifer Buz[1], Bethany L. Ehlmann[1,2], Kjartan Kinch[3], Jeffrey R. Johnson[4], M.S. Rice[5], Justin Maki[2], James F. Bell III[6]
[1]Department of Geologic and Planetary Sciences, California Institute of Technology, Pasadena, CA 91125, U.S.A. [2]NASA Jet Propulsion Laboratory, La Cañada, CA 91109, U.S.A. [3]University of Copenhagen, Niels Bohr Institute, Copenhagen, Denmark [4]Applied Physics Laboratory, Johns Hopkins University, 11101 Johns Hopkins Road 200-W230 Laurel, Maryland 20723-6005, U.S.A. [5]Geology Department, Physics and Astronomy Department, Western Washington University, Bellingham, Washington, USA [6]School of Earth and Space Exploration, Arizona State University, PO Box 871404, Tempe, Arizona 85287-1404, U.S.A.

Abstract

Several commercially available color standards exist, generated by a variety of manufacturers including LabSphere, Lucideon, and Avian Technologies. Previous work has characterized the photometric properties of LabSphere Spectralon targets. Here, we measure the visible and shortwave infrared (VSWIR; 0.4-2.5 um) reflectance at multiple angles and determine the photometric properties of candidate calibration target materials for the Mars 2020 Mastcam-Z instrument. The Lucideon black, grey 33, green, and cyan samples were found to be significantly forward-scattering. The yellow, red, and grey 70 samples were found to be weakly forward scattering. The white Avian Technologies AluWhite98 sample was found to be weakly back scattering. We characterize the absorptions observable with the Mastcam-Z and SuperCam Mars-2020 instruments and note the occurrence of wavelength-dependent photometric properties. The reflectance and photometric data collected here enable the use of these color standards for calibration of Mastcam-Z data from Mars, extension for calibration of other rover cameras and spectrometers, and provide key information for other applications that require the calibration of data from multiple lighting or viewing geometries.

1.0 Introduction

The Mars-2020 (M2020) rover will go to Mars to achieve four main goals: characterize an astrobiologically relevant site, determine the habitability of the site and if any biosignatures are present, cache geologically relevant samples for future retrieval, and prepare for eventual humans on Mars [*Mustard et al.*, 2013]. To achieve these goals several instruments have been selected for the rover, including the Mastcam-Z (MCZ) instrument, which consists of a multispectral pair of visible/near-infrared (VNIR; 440-1010 nm), adjustable-zoom cameras. The science goals of the MCZ instrument, in brief, are to characterize the geomorphology and geology at the rover field site, assess current atmospheric and astronomical phenomena, and provide operational support and scientific context for the M2020 rover [*Bell et al.*, 2016]. In addition to imagery from MCZ, the multispectral capability included allows discrimination of iron-bearing minerals and certain water bearing minerals by detection of their characteristic VNIR absorptions and/or spectral shapes [*Burns*, 1993; *Clark et al.*, 2007].

The MCZ instrument includes a fixed calibration target composed of a reference set of color and grey scale materials of known spectral and photometric properties [*Bell et al.*, 2016]. Illumination conditions vary on the surface of Mars according to the local solar time and the aerosol opacity of the atmosphere at the time of observation. The calibration target is necessary for verification of the preflight calibration of the camera, monitoring the stability of the instrument throughout the mission, and conversion of the radiance measured in data numbers to radiance factor or Lambert albedo to enable comparison with laboratory reflectance spectra of Earth materials [e.g., *Bell et al.*, 2017]. In addition, the MCZ calibration target may be useful for calibration of other onboard instruments such as the VNIR (400-900 nm) and the shortwave infrared (SWIR; 1300-2600 nm) passive spectra from SuperCam, engineering cameras, and cameras mounted on the rover arm. Furthermore, the target serves as a platform of known spectral characteristics to monitor dust deposition and removal throughout the mission [e.g., *Johnson et al.*, 2006; *Kinch et al.*, 2007]. For the calibration target to enable these tasks, a detailed understanding of the photometric properties of the materials that compose the calibration target is imperative. This is the goal of this study.

This study replicates some of the techniques and analysis conducted for the common reflectance standard, Spectralon® SRS-99 (Labsphere, North Sutton, New Hampshire) [*Bruegge et al.*, 1993; *Flasse et al.*, 1993; *Bruegge et al.*, 2001]. The materials used here, manufactured by Lucideon (Staffordshire, UK) and Avian Technologies LLC (Sunapee, NH), are common, commercially available color standard. Therefore, we expect that this study is of utility to others who employ these standards for imaging or spectroscopy applications. We assess the wavelength-dependent spectroscopic properties and photometric behavior of the calibration materials. This paper supplements detailed characterization of the actual assembled calibration target and the derived bidirectional reflectance function for the engineering spare chips (Kinch et al., in prep.).

2.0 Mastcam-Z and its calibration target

The MCZ instrument consists of two zoom-lens cameras, each with a broadband Bayer filter for red/green/blue imagery and with 7 filters mounted on a wheel to provide multispectral capabilities [*Bell et al.*, 2016]. The filters are selected to characterize absorptions in the visible to near-infrared (VNIR) in the wavelength range of 445-1013 nm. The filter combinations allow for 14-wavelength multispectral analysis (Figure 1). The calibration target is a ~8 cm diameter disk with eight color/greyscale chips surrounding four concentric greyscale rings (Figure 1). A gnomon is in the center of the calibration target. The gnomon casts a shadow across the calibration target which allows comparison of direct versus diffuse components of the solar and sky irradiance [*Bell et al.*, 2017]. The calibration target is similar to that flown on the Mars Science Laboratory (MSL) Curiosity rover with modifications based on lessons learned (Figure 1)[*Bell et al.*, 2016]. It is located on the rover at a position where the MCZ instrument has an unobstructed view, where it will be fully illuminated during surface operations, and where there is a minimum of diffuse or reflected light from other structures on the rover. The target is viewed at an angle of 58° from the rover mast while geological materials on the surface are viewed at a wide range of angles.

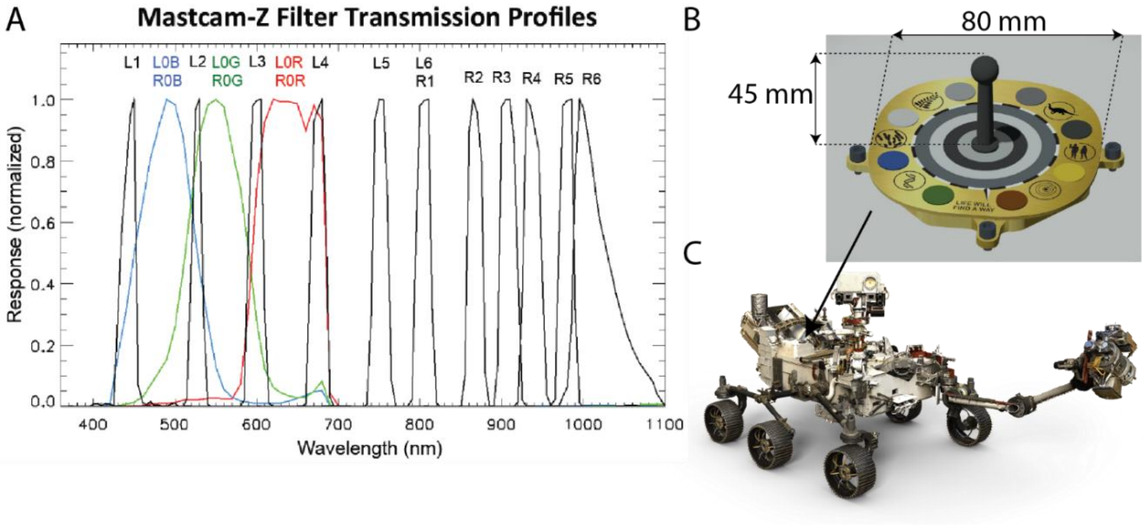

Figure 1. (a) MCZ filter transmission. (b) Primary calibration targets on board the M2020 rover. Not shown, below each color calibration target circle lies a small circular sweep magnet intended to repel some of the Martian dust. Note motto and graphics are preliminary.

For each multispectral target imaged, a corresponding multispectral observation of the calibration target under similar illumination conditions is also acquired, typically on the same day for the MER rover [*Bell et al.*, 2004] or within a five sols for the Mars Science Laboratory rover [*Bell et al.*, 2017; *Wellington et al.*, 2017]. Procedures are expected to be similar for the Mars-2020 rover. From these calibration target images, regions of interest (ROIs) of uniform dust cover are selected from each of the three greyscale rings and the ROI means are plotted against laboratory-measured directional-hemispherical reflectance values [*Wellington et al.*, 2017]. A calibration factor is needed for conversion to radiance factor (I/F), the radiance on sensor compared to the incident solar illumination. To correct for the presence of dust, a two-layer scattering model is used, closely following that of Kinch et al. [2015] with a key difference in that all irradiance is assumed to come from the direction of the sun [*Bell et al.*, 2017]. The result of this model is a single-scattering albedo spectrum for the dust, which can be used to correct the reflectance values on the greyscale ROIs to I/F [*Wellington et al.*, 2017]. Lastly, the calibrated radiance factor is divided by the cosine of the solar incidence angle to determine the relative reflectance (REFF; see Methods) [*Hapke*, 1993; *Wellington et al.*, 2017].

3.0 Methods

In order to characterize the photometric properties of the candidate MCZ calibration target materials it was necessary to obtain reflectance measurements at a series of geometries with a stable and well-calibrated detector and light source. We used a spectro-goniometer developed at Caltech (Figure 2a) that is capable of measuring at all azimuth (Az) angles (0-180°) and at emission (e) and incidence (i) angles from -70° to 70° with a minimum phase angle of ~12°. Incidence and emission angles are measured as positive angles from the vertical, and azimuth is measured positive clockwise from the horizontal projection of the incidence angle (Figure 2b). The phase angle (g), the angle between the incidence and emission angle, is calculated as follows:

$$g = \arccos(\cos(i) * \cos(e) + \sin(i) * \sin(e) * \cos(Az)).$$

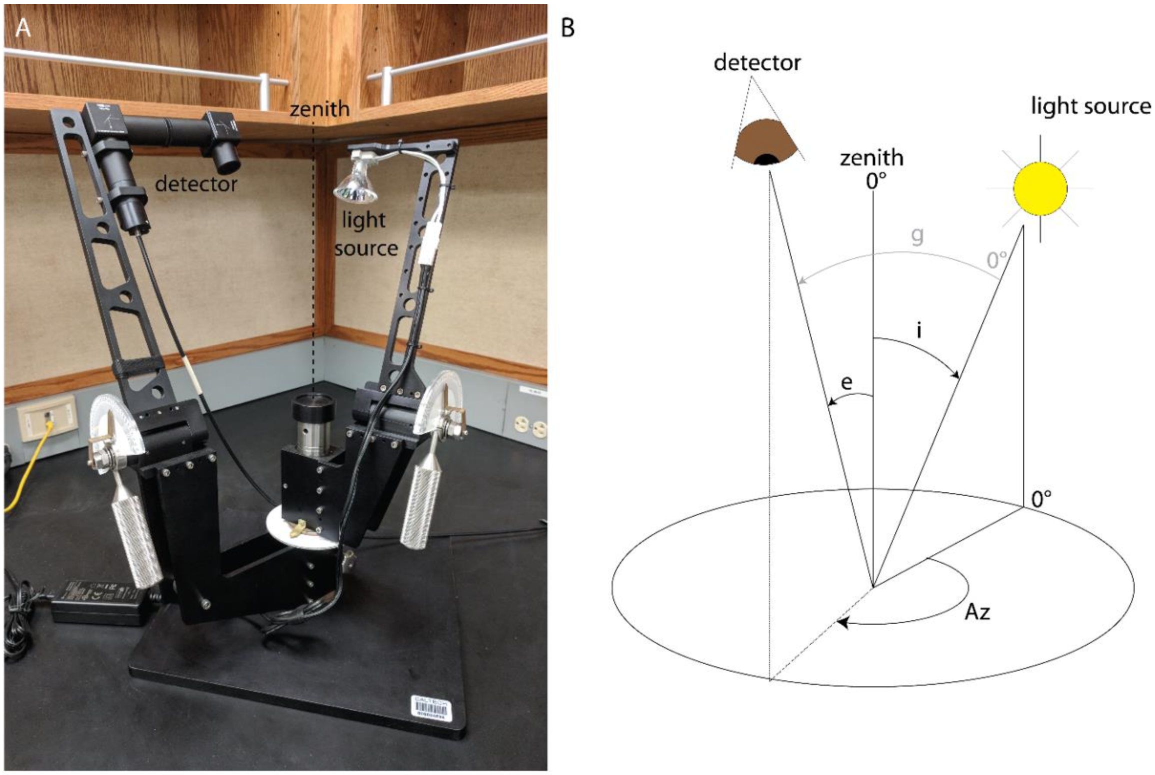

Figure 2. (a) Goniometer set up at the Caltech Earth and Planetary Remote Sensing Laboratory. A fiber optic cable from the spectrometer is fed into the detector assembly. (b) Measurement convention used in this study. Arrows point in positive degree direction.

The measurements were taken with an Analytical Spectral Devices FieldSpec 3®, which allows for reflectance measurements from 350-2500 nm through the use of a 512 element silicon array detector in the VNIR and two graded InGaAs photodiodes in the short-wave infrared (SWIR). These measurements are comparable to those taken with the RELAB instrumentation at Brown University [*Mustard and Pieters*, 1989; *Pilorget et al.*, 2016]. The sample is illuminated with a halogen source. Baffling ensures that the signal comes from a <7 mrad cone, corresponding to diameters on sample of <5mm at e=0° and <2 cm at e=70°. Formally, this is a conical-conical reflectance (Case 5, in Schaepman-Straub et al [2006]) with small angles nearing the ideal bi-directional reflectance function (BRDF). For a white reference standard, we used a Spectralon® target which is approximately Lambertian [*Flasse et al.*, 1993; *Bruegge et al.*, 2001]. The Caltech goniometer was specifically designed for the Spectralon calibration target to lie coincident with the axes of rotation of the goniometer. To match this measurement plane, the MCZ candidate calibration target materials were lifted using thin washers.

Prior to measurements we optimized the gain on each detector with the Spectralon® present using a geometry of $i=12$ and $e=0$. We then positioned the goniometer at the specified geometry and obtained a spectral average of 400 white reference measurements. (This includes a dark current measurement also using a 400 spectra average.) The reflectance of each candidate target material was then measured at this geometry, also using a 400 spectral average. Every 10 minutes the white reference was re-measured, and its spectrum saved.

To account for the differences in each detector we used a routine available with the ASD FieldSpec 3® software. This routine uses five channels from each detector at the filter boundary to calculate a bias value for the VNIR and longer wavelength SWIR detectors. This bias value matches the offset with the shorter wavelength SWIR detector at the splice point.

Following Nicodemus et al. [1977] and the FieldSpec® Pro Users Guide [2002] we output the reflectance as the reflectance factor (*REFF*) which is defined as follows:

$$REFF(i,e,g,\lambda) = \frac{L_{samp}(i,e,g,\lambda) - L_{dark}(\lambda)}{L_{id}(i,e,g,\lambda) - L_{dark}(\lambda)},$$

where $L_{sample}(i,e,g,\lambda)$ is the radiance from the target measured at geometry (i,e,g) at a given wavelength, λ, $L_{id}(i,e,g,\lambda)$ is the radiance from an ideal, perfectly diffuse standard surface measured at geometry (i,e,g), and $L_{dark}(\lambda)$ is the radiance measured with no incident light.

For this study

$$REFF(i,e,g,\lambda) = \frac{L_{samp}(i,e,g,\lambda) - L_{dark}(\lambda)}{L_{std}(i,e,g,\lambda) - L_{dark}(\lambda)} Rstd,$$

where $REFF_{meas}$ is the measured wavelength-dependent reflectance relative to the Lstd, the Spectralon standard measured in the specified geometry. And R_{std} is the NIST-certified value for the wavelength-dependent reflectance of Spectralon®.

Because the purpose of this study was to obtain an understanding of the photometric properties of the target materials, we obtained the REFF measurements at 76 geometries, illustrated in Figure 3. To evaluate the scattering properties of the samples we observed the change in *REFF* at in- and out-of-plane at multiple geometries with $e=58°$ *and* $e=30°$ as well as for in-plane geometries at $e=0$ and $i=30$ (Figure 3). The emission angle of 58° was chosen because it is the approximate emission angle at which the MCZ detector will view the calibration target panel. The remaining angles were chosen to provide a full-suite of measurement geometries enabling a characterization of the photometric properties. We assume symmetry in the photometric properties for azimuth angles 180° to 360°. Each measurement in this study includes the full spectral wavelength range of 350-2500 nm; data were used starting at 400 nm. The data were used to determine the wavelength dependent reflectance of the calibration targets and their photometric properties, including wavelength-dependent changes in photometric behavior. Follow-up studies will obtain measurements at a higher resolution geometric sampling but at limited wavelengths to determine the functional form of the bidirectional reflectance distribution function (BRDF).

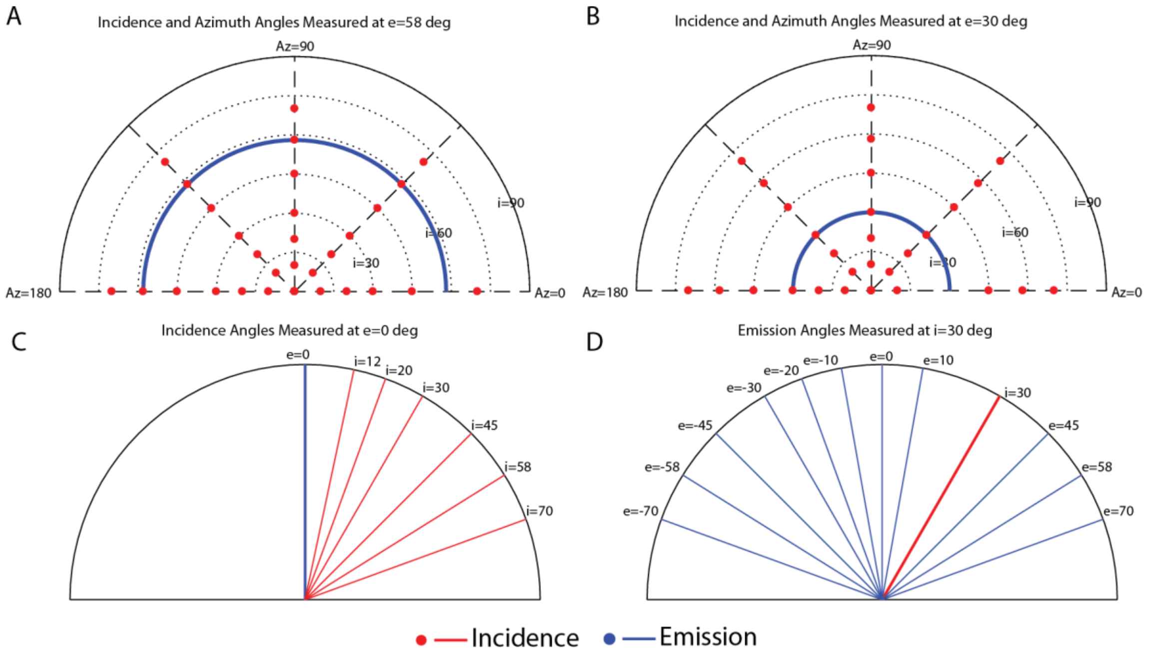

Figure 3. Schematic showing the multiple measurement geometries acquired with the incidence angle indicated in red and the emission angle indicated in blue. Out-of-plane phase angle measurement geometries are shown in (a) and (b) where the emission angle is fixed and the incidence and azimuth angle vary. (c) and (d) show the in-plane measurement geometries.

To ensure that the sample holder material did not influence the spectra collected we measured the sample holder material directly and noted its spectral properties (which were not in common with any of those of the target material and are not further discussed). Lastly, we confirmed absorptions in the 400-1100 nm range by measuring the samples using a different instrument, an Ocean Optics HR200CG ultraviolet-NIR Spectrometer at *i* and *e* of 0°.

4.0 Samples

Eight samples are candidate calibration target materials based on their ability to withstand the rover environment and their photometric properties. These samples are shown in Figure 4 with the Spectralon® white reference also shown. The red, yellow, green, cyan, grey 33, grey 70, and black samples are manufactured by Lucideon while the AluWhite 98 (from now on referred to as white) target is manufactured by Avian Technologies LLC. The Lucideon targets are 5 cm x 5 cm glazed and matted aluminum silicate tiles. The white target is a 5.08 x 5.08 cm matte tile composed of sintered alumina.

Figure 4. Calibration targets used in this study with manufacturer indicated in parentheses and Spectralon® for comparison. All of the Lucideon targets are mounted on a black plastic holder. The AluWhite 98 target is not mounted on any material.

5.0 Results

A summary of the BRDF measurements are given in Figures 5 and 6. The black, grey 33, green, and cyan samples were found to be significantly forward-scattering. The yellow, red, and grey 70 samples were found to be weakly forward scattering. The white sample was found to be weakly back scattering. All samples were found to have wavelength-dependent photometric properties and become more isotropic at longer wavelengths. A brief description of the scattering and reflectance properties of each sample follows, prefaced by an explanation of instrument artifacts. The most illustrative figures are presented here, and all data and normalization plots are available in the supplementary data.

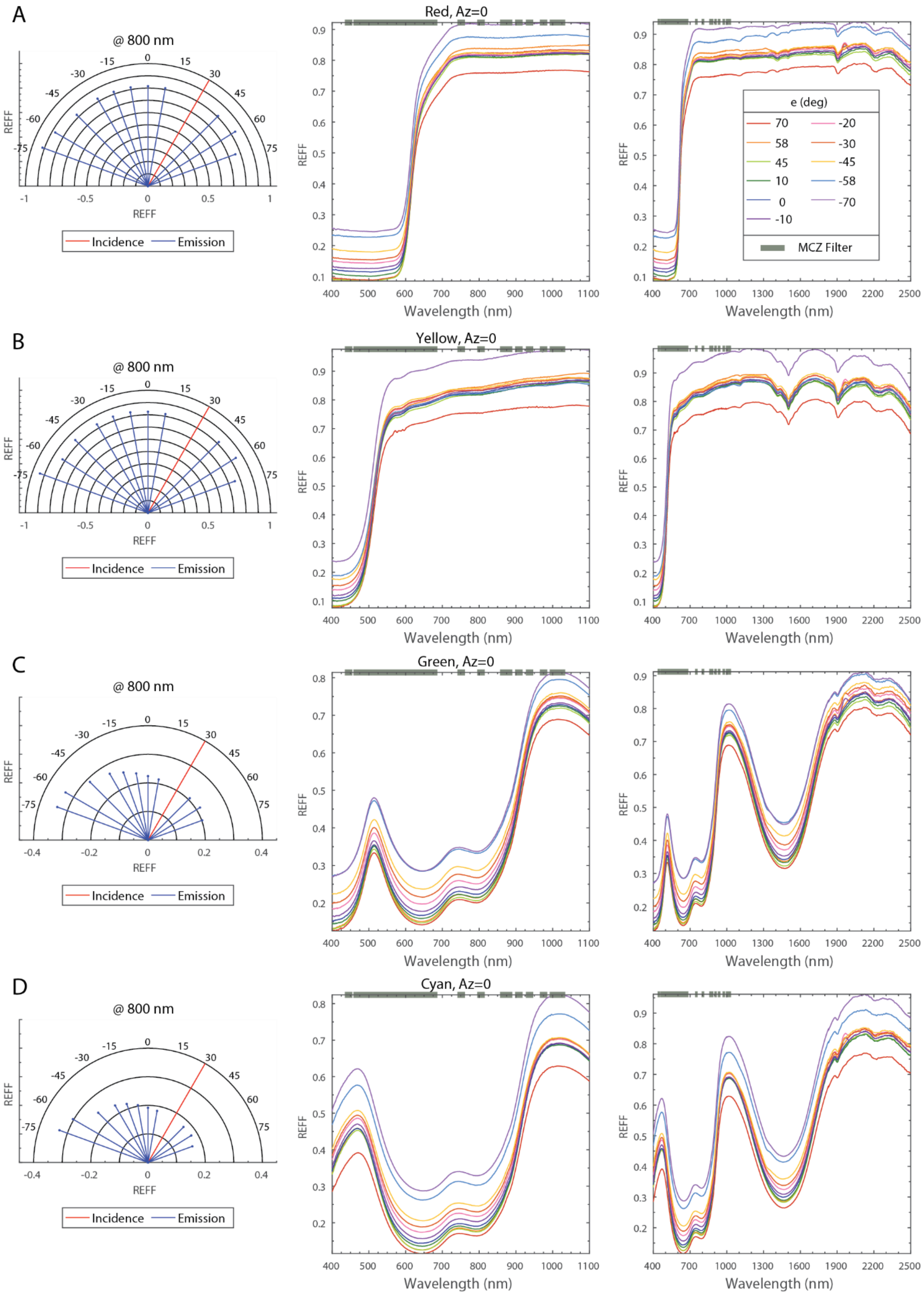
A
@ 800 nm
REFF
Incidence
Emission
Red, Az=0
Wavelength (nm)
e (deg)
70
58
45
10
0
-10
-20
-30
-45
-58
-70
MCZ Filter
B
@ 800 nm
Yellow, Az=0
C
@ 800 nm
Green, Az=0
D
@ 800 nm
Cyan, Az=0

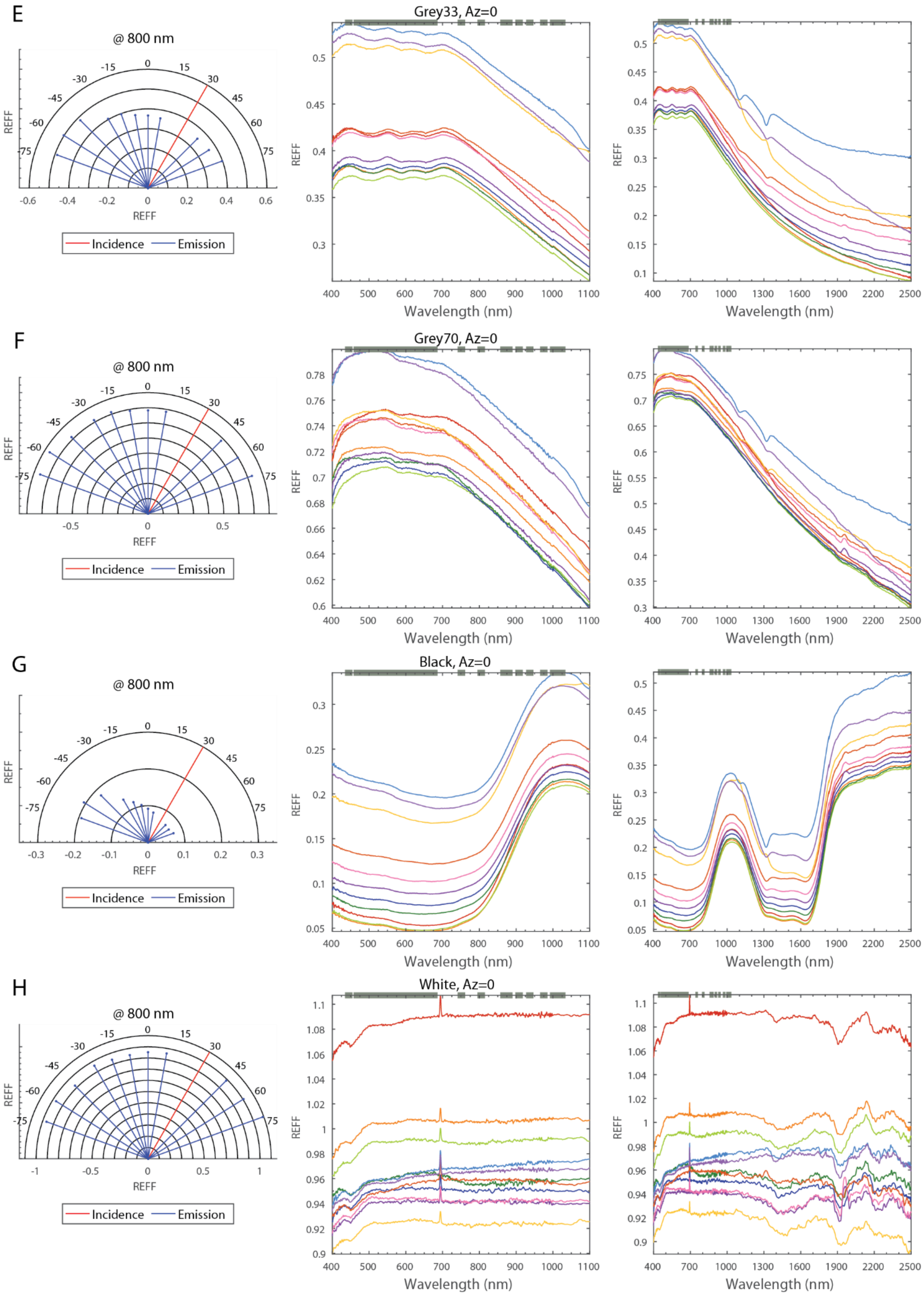

Figure 5. Spectra and scattering properties of the MCZ calibration targets. The left most polar

diagrams show the effect of changing emission angle on the REFF at 800 nm for a fixed incidence angle of 30 degrees in the principal plane. If the sample were isotropic its changing angular REFF would follow the semi-circle. The right two columns show the spectra for the various samples. The middle column shows only the MCZ relevant wavelengths and the right column shows the full measurement range.

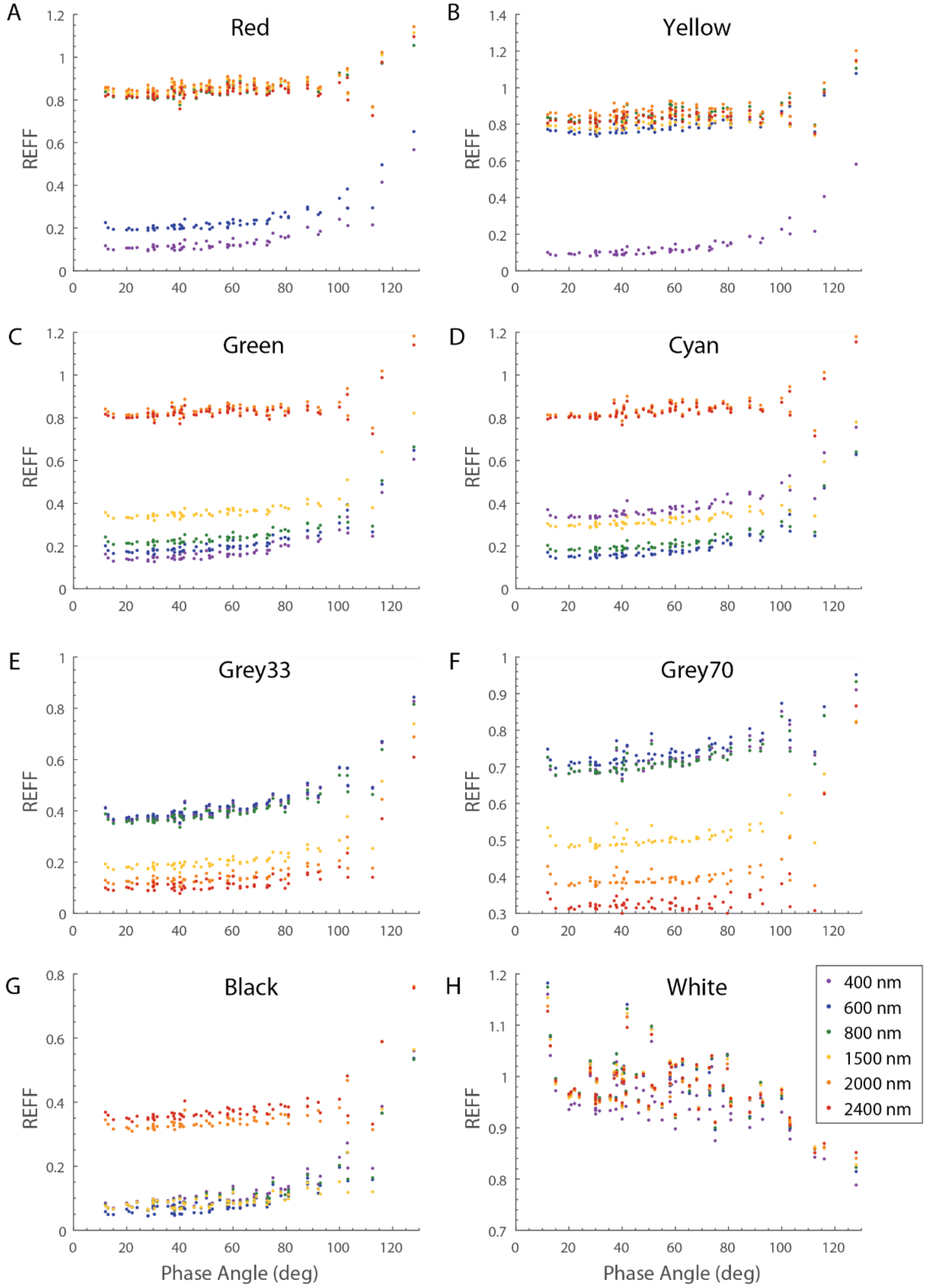

Figure 6. REFF at 400, 600, 800, 1500, 2000, and 2400 nm for all measured geometries. All samples except white demonstrate a positive trend with increasing phase angle, indicating forward scattering behavior. White displays a weak negative trend with phase angle indicating

back scattering behavior. There is a shallowing of this trend for the longer wavelength measurements.

5.1 Data quality and known instrument artifacts

The Caltech goniometer data were examined in Pilorget et al. [2016], compared to that acquired in RELAB, and matched within 10%. White reference spectra acquired every 10 minutes during measurement were ratioed and the instrument was stable. Data shorter than 400 nm and longer than 2500 nm were evaluated for quality and excluded due to low signal to noise ratio. The 400-2500 nm wavelength range is reliable with the exceptions below where caution in interpreting data is needed.

In the raw data from the spectrometer and also occasionally in the corrected reflectance data, we observe spectral features at ~1100 and ~1320 nm (dashed grey lines in Figure 7). According to correspondence with the makers of the ASD instrument, these absorptions are related to varying proportions of on-axis and off-axis signal entering the spectrometer, depending on brightness. These artifacts affect several of our spectra and are more pronounced at certain geometries. Consequently, the wavelength ranges 1100±30 nm and 1320±30 nm should be ignored in our REFF data. We also observe weak absorptions at ~1400 nm and ~1900 nm (dashed blue lines in Figure 7), which can be caused by vibrational absorptions related to water in the instrument path length. In most REFF data, this wavelength region is reliable. There are strong 1400 nm and 1900 nm absorptions in the samples themselves due to water in the materials; however, smaller, superimposed fluctuations should be interpreted with caution.

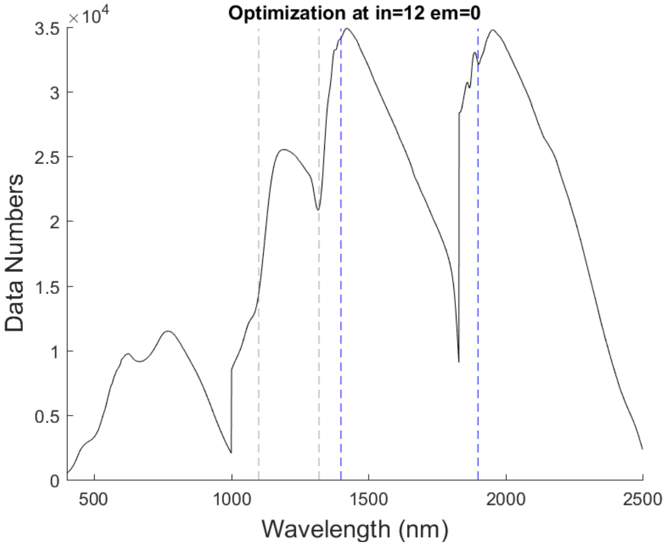

Figure 7. Optimization curves for the three detectors of the ASD FieldSpec 3® demonstrating features at 1100, 1320, 1400, and 1900 nm.

5.2 Lucideon Red

The Lucideon red target's spectrum is low, flat, and feature-less below ~600 nm with a strong increase of about 0.65 REFF between ~600 and ~700 nm. The spectrum remains flat after ~700 nm for the duration of the MCZ filter set; however, has several absorptions at wavelengths longer than 1000 nm. The strongest are at ~1400, ~1900, and ~2200 nm.

The red sample is quasi-isotropic, slightly forward scattering, as shown in Figures 5a, 6a, and 8. The REFF increases by ~0.21 over the 116° range at 800 nm. The sample becomes slightly more isotropic at longer wavelengths (change in REFF is ~0.47 at 400 nm). Observations at 58° and 70° may be slightly discrepant.

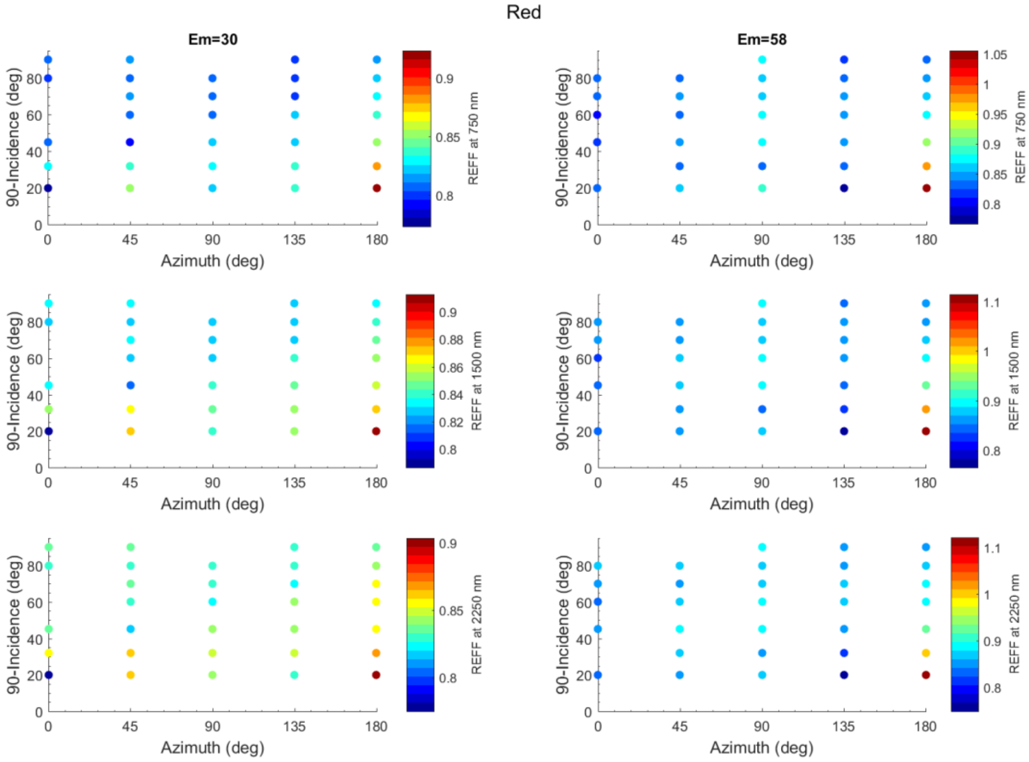

Figure 8. Scattering properties of the red target at 750, 1500, and 2250 nm. The sample appears to become slightly more isotropic at longer wavelengths (note the change in range in REFF for the Em=30 measurement suite.)

5.2 Lucideon Yellow

The Lucideon yellow target REFF is low below ~475 nm with a strong increase of about 0.6 REFF between ~475 and ~550 nm. The REFF increases at a low slope from ~550nm to ~1400 nm. There are weak absorptions around ~570, ~630, and ~800 nm. Several stronger absorptions are observed at wavelengths longer than the MCZ filter set at ~1400, ~1500, and ~1900 nm.

The yellow sample is quasi-isotropic, slightly forward scattering, as shown in Figures 5b, 6b, and 9. The REFF increases by ~0.25 over the 116° range at 800 nm. The sample becomes slightly more isotropic at longer wavelengths (change in REFF is ~0.5 at 400 nm). Observations at 58° and 70° may be slightly discrepant.

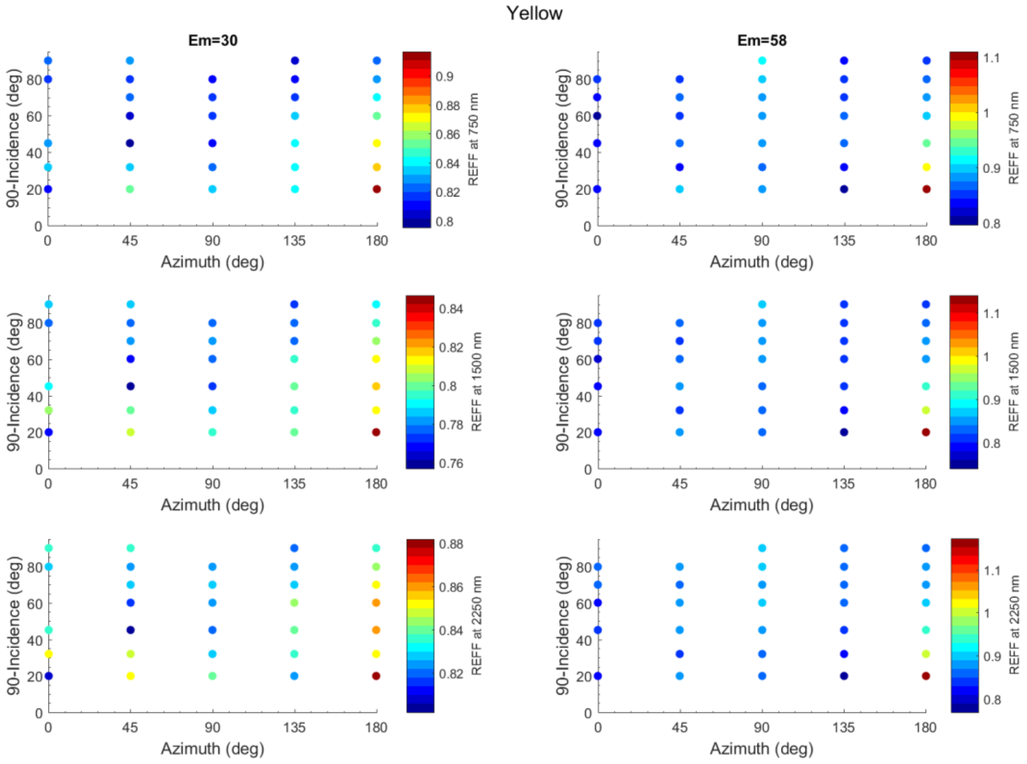

Figure 9. Scattering properties of the yellow target at 750, 1500, and 2250 nm.

5.3 Lucideon Green

The Lucideon Green sample spectrum is variable in the wavelength range of the MCZ filter set. Strong, broad absorptions appear at ~400, ~650, ~800 and ~1500 nm. Weaker absorptions are observed at ~1900 and ~2200 nm.

The green sample is forward scattering, as shown in Figures 5c, 6c, and 10. The REFF increases by ~0.4 over the 116° range at 800 nm. The sample becomes slightly more isotropic at longer wavelengths (change in REFF is ~0.45 at 400 nm).

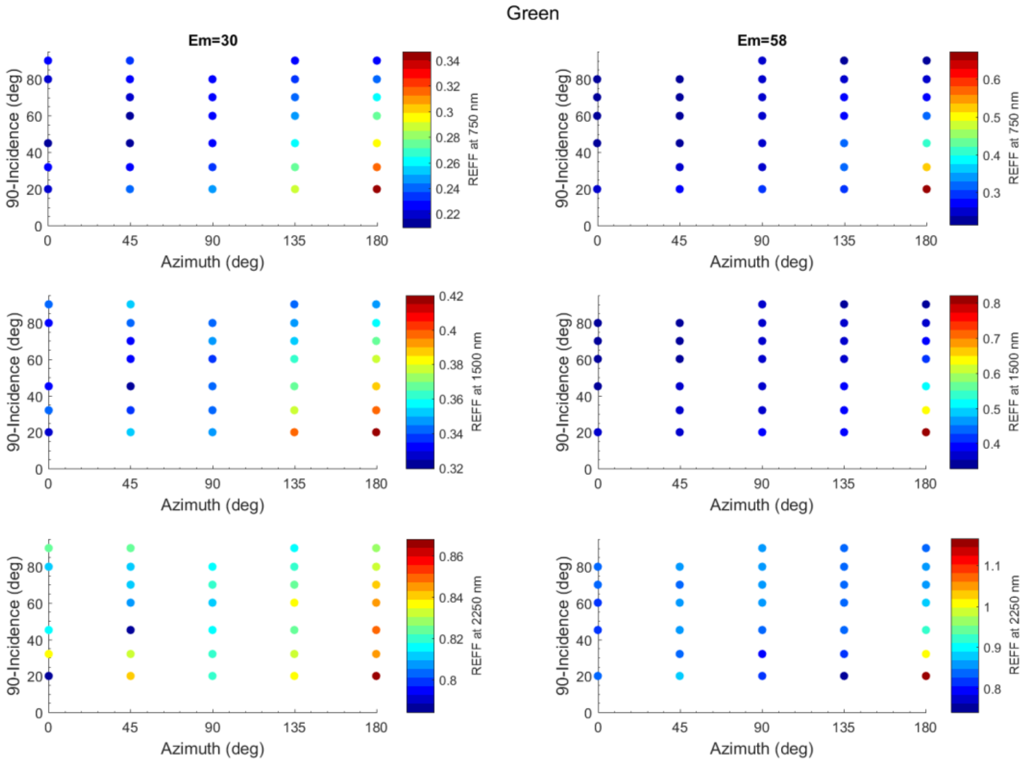

Figure 10. Scattering properties of the green target at 750, 1500, and 2250 nm.

5.4 Lucideon Cyan

The Lucideon cyan sample spectrum is variable in the wavelength range of the MCZ filter set. Strong, broad absorptions appear at ~650, ~800 and at ~1500 nm. Weaker absorptions are observed at ~1900 nm and ~2200 nm. The REFF increases from 400 nm to ~475 nm.

The cyan sample is forward scattering, as shown in Figures 5d, 6d, and 11. The REFF increases by ~0.45 over the 116° range at 800 nm. The sample becomes slightly more isotropic at longer wavelengths (change in REFF is ~0.35 at 2400 nm).

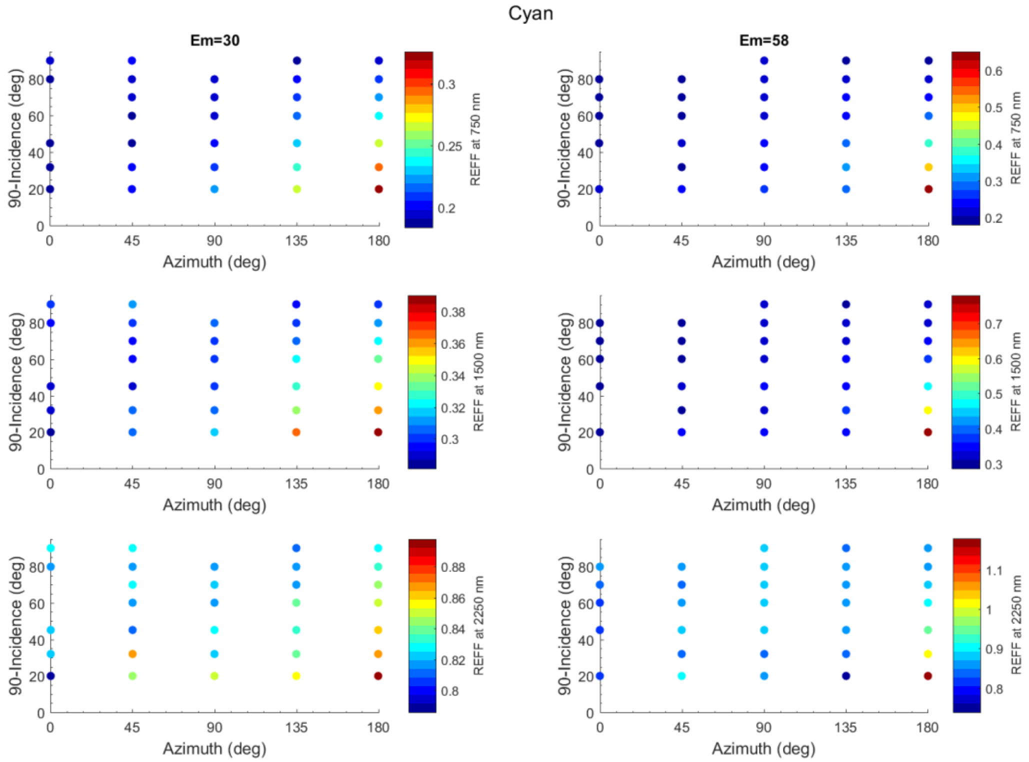

Figure 11. Scattering properties of the cyan target at 750, 1500, and 2250 nm.

5.5 Lucideon Grey 33

The Lucideon grey 33 sample is relatively flat between 400 and 700 nm (REFF varies <0.25), there are weak absorptions present at ~500, ~600, and ~650 nm. After ~700 nm the spectrum decreases linearly approximately 0.15 REFF until ~1250 nm after which the spectrum decrease shallows.

The grey 33 sample is quasi-isotropic, slightly forward scattering, as shown in Figures 5e, 6e, and 12. The REFF increases by ~0.5 over the 116° range at 800 nm. Observations at -45° and 70° may be slightly discrepant.

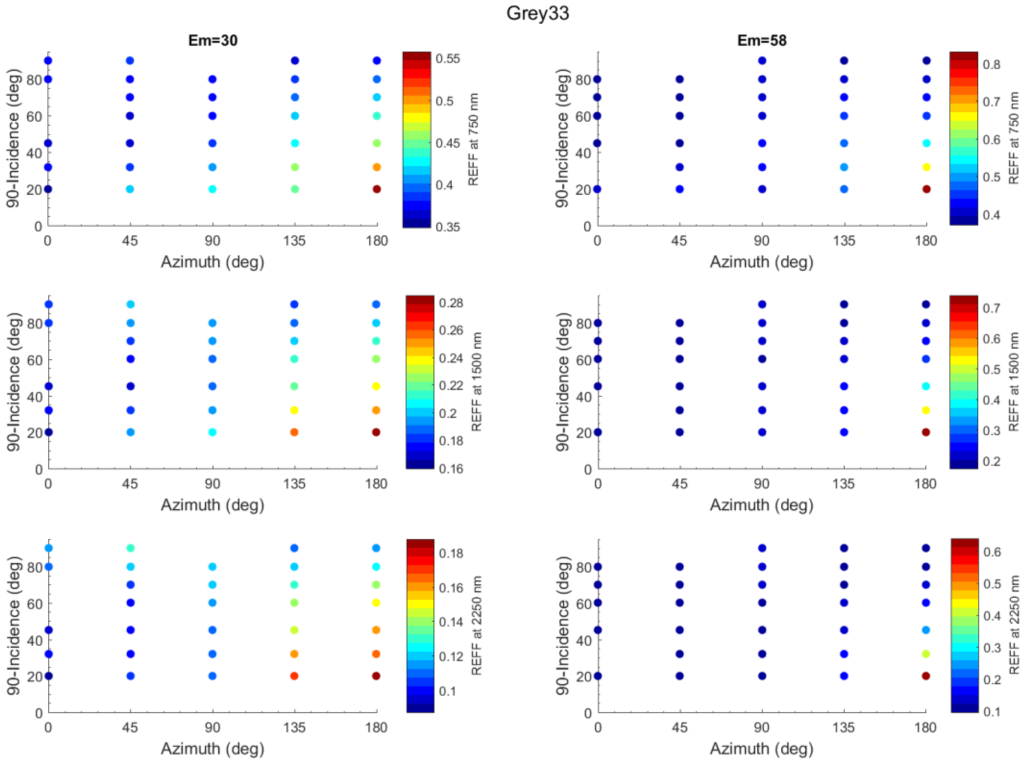

Figure 12. Scattering properties of the grey33 target at 750, 1500, and 2250 nm.

5.6 Lucideon Grey 70

The Lucideon grey 70 sample spectrum rises up to ~550 nm after which it has two small absorptions at ~600 and ~650. Around ~720 nm the spectrum begins a smooth and roughly monotonic decrease for the duration of the observed wavelength range.

The grey 70 sample is quasi-isotropic, slightly forward scattering, as shown in Figures 5f, 6f, and 13. The REFF increases by ~0.24 over the 116° range at 800 nm. Observations at -58°, -70°, and 70° may be slightly discrepant.

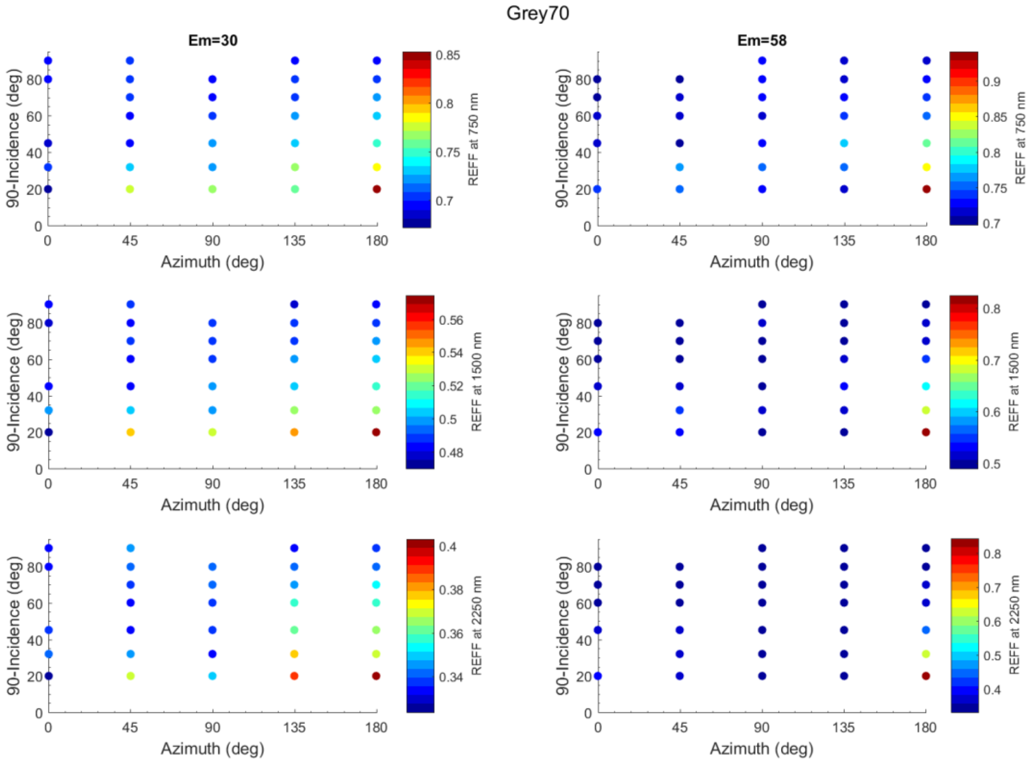

Figure 13. Scattering properties of the grey70 target at 750, 1500, and 2250 nm.

5.7 Lucideon Black

The Lucideon black sample spectrum is relatively flat from 400 to ~800 nm with a slight negative slope (REFF decreases ~0.04) and a subtle positive feature ~550 nm. The spectrum begins a gradual increase from ~800 to 1000 nm of about ~.15 REFF, after which it decreases approximately equally until ~1250 nm. At longer wavelengths the spectrum is flat until ~1700 nm and then increases sharply for ~100 nm after which the REFF increase is shallow.

The black sample is forward scattering, as shown in Figures 5g, 6g, and 14. The REFF increases by ~0.45 over the 116° range at 800 nm. The sample becomes slightly more isotropic at longer wavelengths (change in REFF is ~0.4 at 2400 nm). Observations at 70° may be slightly discrepant.

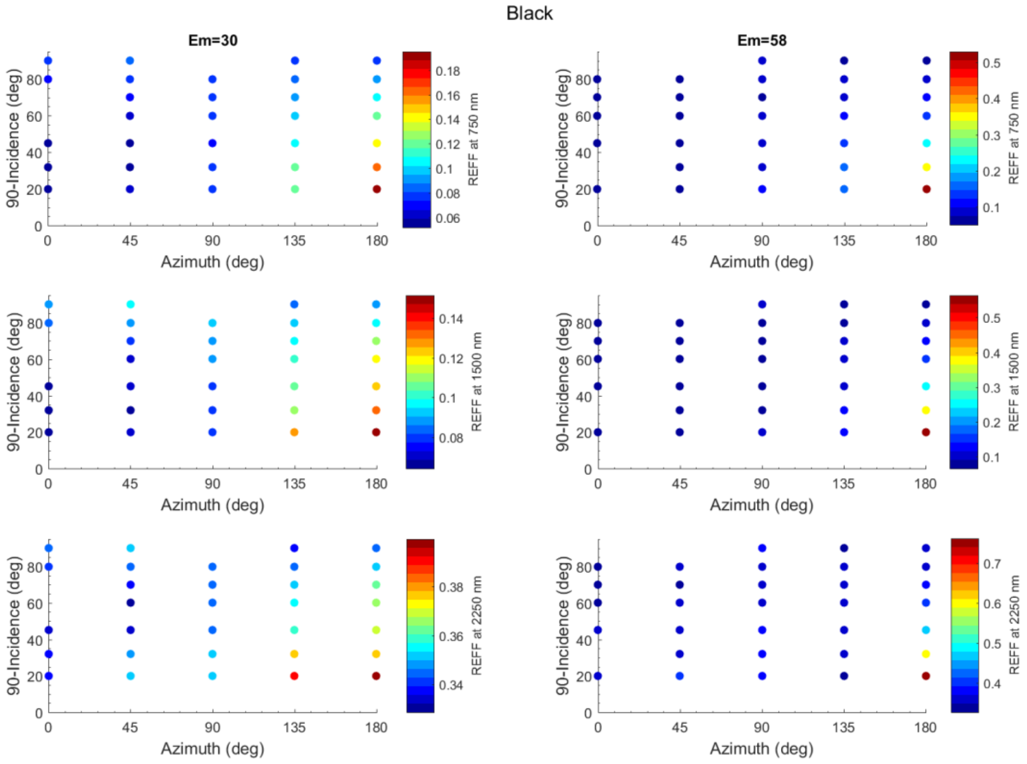

Figure 14. Scattering properties of the black target at 750, 1500, and 2250 nm.

5.8 Avian Technologies White

The Avian technologies white sample spectrum is relatively flat throughout the entire wavelength range (varying < 0.05 REFF). There is a weak absorption present at ~450 nm and a sharp peak at 694 nm (Figure 5h). This 694 nm peak was confirmed with the UV-NIR spectrometer and corresponds to a well-documented fluorescence in chromium, a common substitution in Al_2O_3, of which the sample is composed [*Ragan et al.*, 1992]. It may be related to a Cr for Al substitution in the structure.

The white sample is quasi-isotropic, slightly back scattering, as shown in Figures 5h, 6h, and 15. The REFF increases by ~0.25 over the 116° range at 800 nm. The sample becomes slightly more isotropic at longer wavelengths (change in REFF is ~0.5 at 400 nm). Observations at 70° may be slightly discrepant.

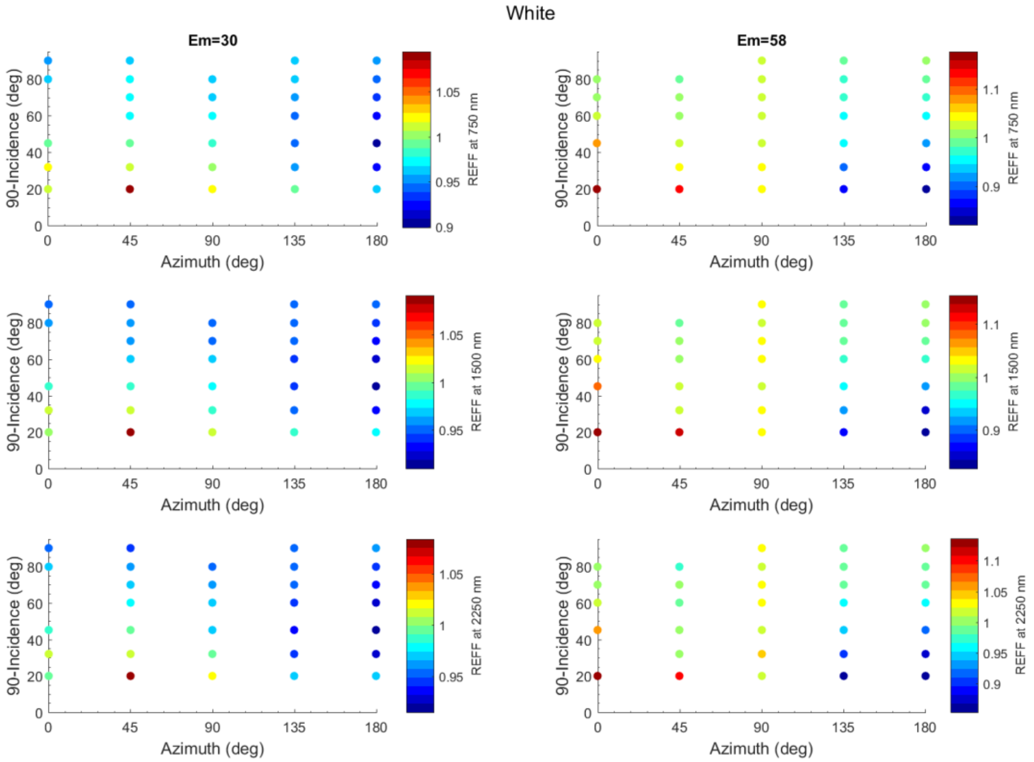

Figure 15. Scattering properties of the white target at 750, 1500, and 2250 nm.

5.9 Convolution to MCZ filter set

We approximated the MCZ camera multispectral data of the calibration targets (Figure 16). Overall the MCZ filter set reproduces the general spectral shape of the targets.

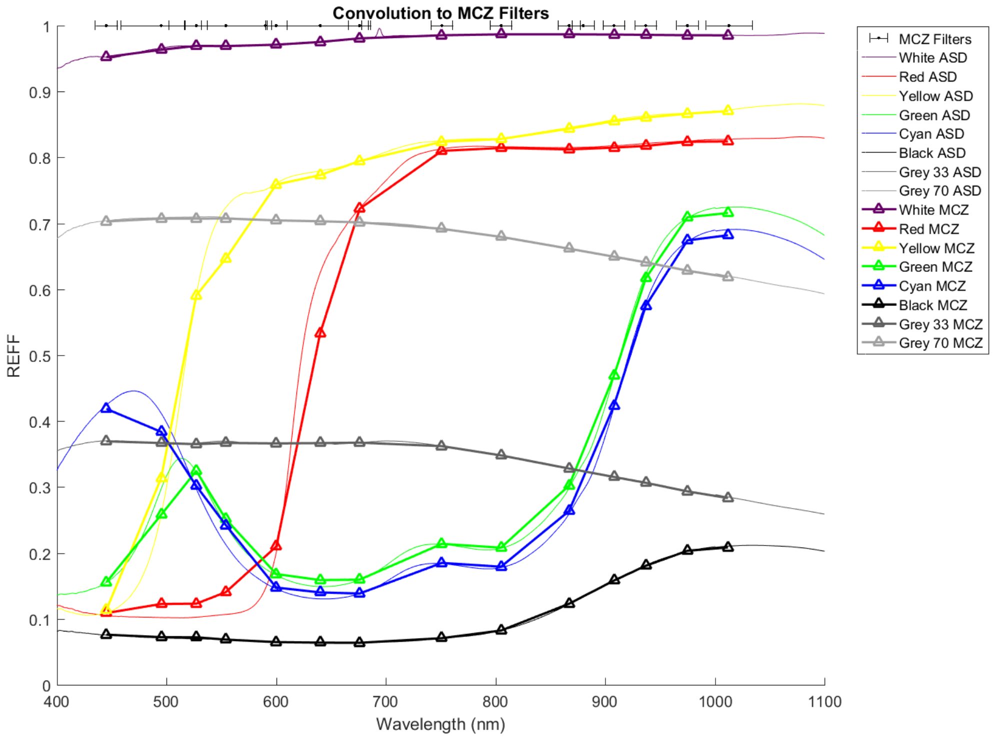

Figure 16. Convolution of spectra on calibration target materials to MCZ filter set.

5.10 Slope as a function of viewing geometry

There is a significant change in spectral slope with viewing geometry for certain measurement suites (Figure 17). The degree of this change is variable across samples and measurement suites. Figure 17 demonstrates two measurement suites for the grey33 and yellow samples. The yellow sample appears to have minimal/absent change in spectral slope for either measurement suite. The grey33 sample however has significant change in spectral slope at the Az=180, Em=58 measurement suite. This effect is still observed, though to a lesser degree at the Em=30 suite. This is likely due to wavelength dependent photometric properties suggested by the data in Figure 17.

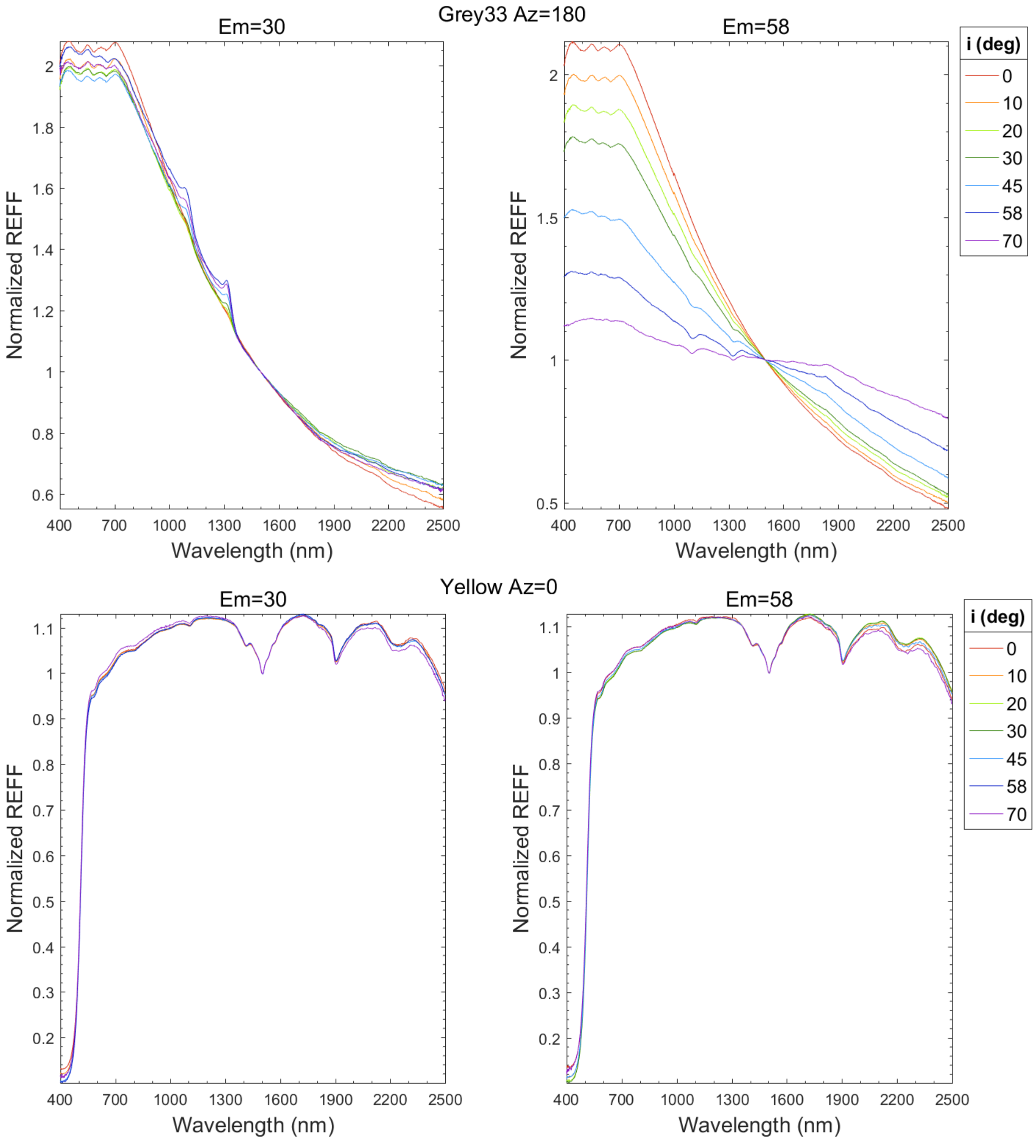

Figure 17. Slope as a function of viewing geometry for the same set of measurements for grey33 and yellow samples at Az=180.

5.11 Change in absorption strength as a function of viewing geometry

Two absorptions were analyzed for changes in band depth with viewing geometry: the 1470 nm absorption band on the green sample and the 660 nm absorption band on the grey 33 sample (Figure 18). On the green sample, for the e=58° measurements, the band depth appears to decrease with increasing azimuth for a given incidence angle suite. The sample however, is strongly forward scattering, as previously mentioned so there is an increase in REFF with azimuth. There is no observable trend with absorption strength for the grey 33 sample.

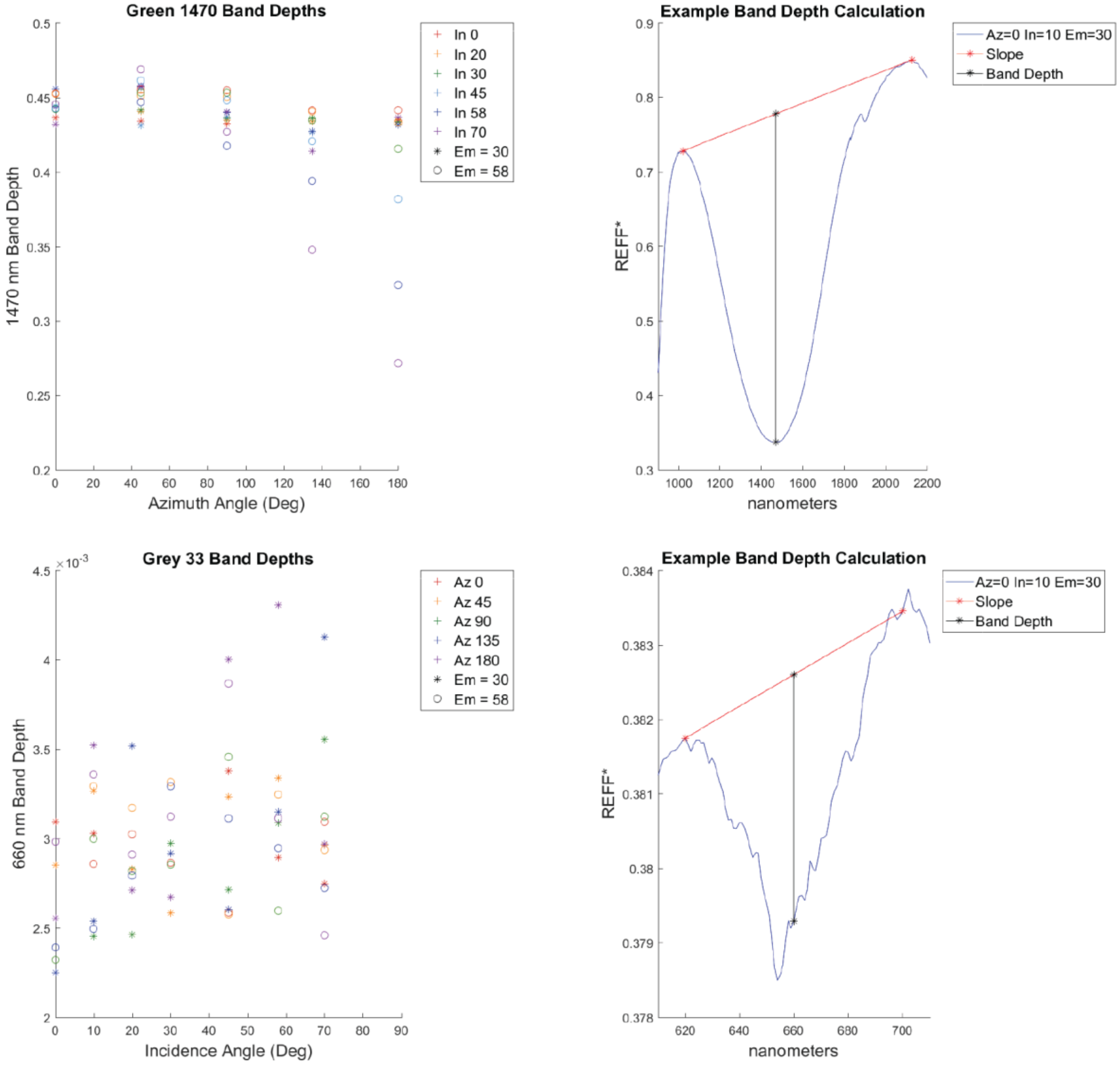

Figure 18. Band depth calculations and changes with phase angle

6.0 Discussion

For some applications where photometry is important, such as in observations of materials on Mars with the Mars-2020 rover, this study shows that the characterization of the angular dependence of sample reflectance for these candidate calibration target materials is critical. The suite of targets do not all behave in the same manner with weakly backward scattering (Avian Technologies AluWhite98), weakly forward scattering (Lucideon's yellow, red, and grey 70), and strongly forward scattering (Lucideon's cyan, green, grey 33, and black) behavior, depending on the sample. The calibration target materials are not Lambertian, and most vary from isotropic behavior in significant ways, but their photometric properties vary in consistent ways that can be easily described.

When compared with the calibration targets found on the MER rover calibration target and MSL Curiosity's Mastcam calibration targets [*Bell et al.*, 2003; *Bell et al.*, 2017], these candidate materials from commercial vendors are spectrally flatter in the 400-700 nm range, with the exception of the green target. Sharp absorptions should be avoided in calibration target materials, especially if they occur near the boundaries of the band pass filters, but these targets have smoothly varying properties in the relevant 400-1100nm range for Mars-2020/Mastcam-Z and for any other VNIR imaging and spectroscopy investigations. The Avian Technologies AluWhite 98 emission peak at 698 nm is an interesting, unexpected exception, but as it occurs within the center of the band pass, should not affect calibration. Sharp absorptions are present at longer wavelengths in the red, yellow, green, cyan, and white calibration materials tested, so users for SWIR multispectral imaging applications should consider these when selecting calibration materials and band pass cutoffs. The emission peak in AluWhite and the sharp absorptions at larger wavelengths may provide additional information to characterize wavelength position.

The change in photometric properties with wavelength for each target provides an explanation for the changes in slope and absorption strength observed in the samples. The changes in photometric properties certainly must be accounted for as the sun angle on the calibration target varies. For observations at longer wavelengths than the Mastcam-Z instrument, e.g., by SuperCam on Mars, the narrow absorptions confound use as uniform surfaces but may prove useful for monitoring dust buildup (by absorption shallowing), complementing short wavelength observations.

7.0 Conclusions and future work

The measurement suite captures the effect of viewing geometry on REFF for one Avian Technology target (AluWhite98) and 7 Lucideon targets (red, yellow, cyan, green, grey 70, grey 33, and black). Some of the samples are quasi-isotropic: the white target is slightly backward scattering and the red, yellow, and grey 70 targets are slightly forward scattering. The cyan, green, grey, and black targets are strongly forward scattering. The forward scattering behavior is most significant at shorter wavelengths (i.e., in the MCZ measurement range), generally decreasing at longer wavelengths. This wavelength-dependence cause changes in spectral slope and absorption band depth depending on the viewing geometry. The scattering properties have been quantified here and can thus be corrected for. Our data alone are too sparse for a full BRDF characterization as was done in Bell et al. [2003], but this will be future work led by one of us (Kinch). Additional measurements will be taken at the Bloomsberg University Goniometer and the data will be integrated into a combined He-Torrence/Hapke model [*He et al.*, 1991; *Hapke*, 1993].

8.0 References

Bell, J. F., 3rd, et al. (2004), Pancam multispectral imaging results from the Spirit Rover at Gusev Crater, *Science*, *305*, 800-806, doi:10.1126/science.1100175.

Bell, J. F., et al. (2017), The Mars Science Laboratory Curiosity rover Mastcam instruments: Preflight and in-flight calibration, validation, and data archiving, *Earth and Space Science*, *4*, 396-452, doi:10.1002/2016ea000219.

Bell, J. F., J. N. Maki, G. L. Mehall, M. A. Ravine, M. A. Caplinger, and Z. T. Mastcam (2016), MastCam-Z: Designing a geologic, stereoscopic, and multispectral pair of zoom cameras for the NASA Mars 2020 rover, paper presented at 3rd International Workshop on Instrumentation for Planetary Missions, 2016.

Bell, J. F., et al. (2003), Mars Exploration Rover Athena Panoramic Camera (Pancam) investigation, *J Geophys Res-Planet*, *108*, 8063, doi:10.1029/2003je002070.

Bruegge, C., N. Chrien, and D. Haner (2001), A spectralon BRF data base for MISR calibration applications, *Remote Sensing of Environment*, *77*, 354-366, doi:10.1016/S0034-4257(01)00214-0.

Bruegge, C. J., A. E. Stiegman, R. A. Rainen, and A. W. Springsteen (1993), Use of Spectralon as a Diffuse Reflectance Standard for in-Flight Calibration of Earth-Orbiting Sensors, *Optical Engineering*, *32*, 805-814, doi:10.1117/12.132373.

Burns, R. G. (1993), *Mineralogical applications of crystal field theory*, 5, Cambridge University Press.

Clark, R. N., G. A. Swayze, R. Wise, K. E. Livo, T. M. Hoefen, R. F. Kokaly, and S. J. Sutley (2007), *USGS digital spectral library splib06a*, US Geological Survey Reston, VA.

Devices, A. S. (2002), FieldSpec Pro–User's Guide.', *Analytical Spectral Devices: Boulder, CO*.

Flasse, S. P., M. V. Michel, P. Bernard, and J. B. Carol (1993), Modeling Spectralon's bidirectional reflectance for in-flight calibration of Earth-orbiting sensors, paper presented at Recent Advances in Sensors, Radiometric Calibration, and Processing of Remotely Sensed Data, 1993.

Hapke, B. (1993), *Theory of Reflectance Spectroscopy*, Cambridge University Press.

He, X. D., K. E. Torrance, F. X. Sillion, and D. P. Greenberg (1991), A Comprehensive Physical Model for Light-Reflection, *Comp Graph*, *25*, 175-186.

Johnson, J. R., et al. (2006), Radiative transfer modeling of dust-coated Pancam calibration target materials: Laboratory visible/near-infrared spectrogoniometry, *J. Geophys. Res.*, *111*, doi:doi:10.1029/2005JE002658.

Kinch, K. M., J. F. Bell, 3rd, W. Goetz, J. R. Johnson, J. Joseph, M. B. Madsen, and J. Sohl-Dickstein (2015), Dust deposition on the decks of the Mars Exploration Rovers: 10 years of dust dynamics on the Panoramic Camera calibration targets, *Earth Space Sci*, *2*, 144-172, doi:10.1002/2014EA000073.

Kinch, K. M., J. Sohl-Dickstein, J. F. Bell, J. R. Johnson, W. Goetz, and G. A. Landis (2007), Dust deposition on the Mars Exploration Rover Panoramic Camera (Pancam) calibration targets, *J. Geophys. Res.*, *112*, doi:10.1029/2006JE002807.

Mustard, J. F., et al. (2013), Report of the Mars 2020 Science Definition Team, *Mars Exploration Program Analysis Group*154.

Mustard, J. F., and C. M. Pieters (1989), Photometric Phase Functions of Common Geologic Minerals and Applications to Quantitative-Analysis of Mineral Mixture Reflectance Spectra, *J Geophys Res-Solid*, *94*, 13619-13634, doi:10.1029/JB094iB10p13619.

Pilorget, C., J. Fernando, B. L. Ehlmann, F. Schmidt, and T. Hiroi (2016), Wavelength dependence of scattering properties in the VIS–NIR and links with grain-scale physical and compositional properties, *Icarus*, *267*, 296-314, doi:10.1016/j.icarus.2015.12.029.

Ragan, D. D., R. Gustavsen, and D. Schiferl (1992), Calibration of the ruby R1 and R2 fluorescence shifts as a function of temperature from 0 to 600 K, *Journal of Applied Physics*, *72*, 5539-5544, doi:10.1063/1.351951.

Schaepman-Strub, G., M. E. Schaepman, T. H. Painter, S. Dangel, and J. V. Martonchik (2006), Reflectance quantities in optical remote sensing—definitions and case studies, *Remote Sensing of Environment*, *103*, 27-42, doi:https://doi.org/10.1016/j.rse.2006.03.002.

United States. National Bureau of, S., and F. E. Nicodemus (1977), *Geometrical considerations and nomenclature for reflectance*, 160, US Department of Commerce, National Bureau of Standards.

Wellington, D. F., J. F. Bell, J. R. Johnson, K. M. Kinch, M. S. Rice, A. Godber, B. L. Ehlmann, A. A. Fraeman, C. Hardgrove, and M. S. Team (2017), Visible to near-infrared MSL/Mastcam multispectral imaging: Initial results from select high-interest science targets within Gale Crater, Mars, *American Mineralogist*, *102*, 1202-1217, doi:10.2138/am-2017-5760CCBY.

Chapter 4

POSSIBLE SHOCK ORIGIN FOR MAGNETIZATION IN ALH84001 CARBONATES

Jennifer Buz[1], Joseph L. Kirschvink[1,2], Atsuko Kobayashi[2]
[1]Department of Geologic and Planetary Sciences, California Institute of Technology,
Pasadena, CA 91125, U.S.A. [2]Earth-Life Science Institute, Tokyo Institute of Technology,
Meguro, 152-8550 Tokyo, Japan.

Abstract

ALH84001 is a Martian meteorite containing magnetite crystals that are putative microfossils because of their striking resemblance to magnetite produced by magnetotactic bacteria. If these crystals were in fact formed biologically they would be entrained within the carbonate through a depositional/cementation process. An alternative, abiotic, origin hypothesis involves the generation of this magnetite from the chemical alteration (thermal or through a shock process) of the iron-bearing carbonate that hosts it. These origin scenarios would have different paleomagnetic signatures.

The Fuller test of NRM measures the efficiency of magnetization of a sample. For samples which have a magnetization from a depositional process, as would be the case for magnetite crystals produced prior to entrainment, the efficiency of the magnetization is ~100 times weaker as compared to magnetization acquired through chemical alteration or shock processes. This inefficiency is due to gravity and Brownian motion that act on the crystals during deposition, but also depends somewhat on the background field strength. The ARM susceptibility test probes the inter-particle interactions within a sample. Magnetite crystals formed prior to deposition are likely to clump together during aqueous transport. These clumped crystals will have large inter-particle interactions, as opposed to evenly distributed particles formed chemically or through shock. The Lowrie-Fuller test distinguishes between single (consistent with biogenic magnetite) and multi-domain particles and allows the coercivity of magnetization to be compared with laboratory fields. Shock processes preferentially affect lower coercivity grains.

We extracted four pieces of magnetite bearing carbonate from ALH84001 and using high-resolution scanning SQuID microscopy conducted standard demagnetization and the three aforementioned tests. We observe that the efficiency of magnetization is high, which would be consistent with a chemical or shock origin in an Earth strength field. However, we find that the carbonate pieces host magnetic particles that are strongly interacting. The carbonates carry predominantly single domain grains and the demagnetization of three of the four particles is primarily carried in the low coercivity grains in the natural remanent magnetization, as opposed to more evenly distributed as in the laboratory applied fields. A nearly saturating magnetization in the fourth particle may indicate magnetic contamination (e.g. during processing). The cumulative test results favor a shock origin for the magnetization held within the carbonate crystals but a biogenic origin cannot be excluded because it is possible that the magnetite existed within the carbonate prior to this potential shock event.

1. Introduction

1.1 Potential Biosignatures

ALH84001's infamy began with McKay et al.'s [1996] claim that the meteorite hosted potential Martian biosignatures. McKay et al [1996] reported the presence of polycyclic aromatic hydrocarbons (PAHs; which in terrestrial rocks are often derived from chemical aromatization of biological precursors), carbonate zonation mimicking that mediated by biological processes, magnetite which is often indistinguishable in its purity, shape, and composition from that generated by magnetotactic bacteria, and lastly common ovoid and elongated forms in the carbonate that were interpreted as 'nanobacteria', but –if actually biological – would better be interpreted as subcellular appendages like flagella or pili [*Gibson et al.*, 2001]. While three of the four potential biosignatures have been demonstrated to occur abiotically, the formation of these unique magnetite nanocrystals has not been replicated in laboratory investigations. Approximately 9% of these magnetite particles examined by high-resolution transmission electron microscopy are indistinguishable from particles only known to be produced by strains of magnetotactic bacteria on Earth (Figure 1) [*McKay et al.*, 1996; *Thomas-Keprta et al.*, 2000; *Thomas-Keprta et al.*, 2001]. They bear five of six properties characteristic of biogenic magnetite: hexaoctahedron morphology, chemically pure, intact crystal lattice, inside the single domain stability field with restricted width/length ratios, and elongation along the [1 1 1] axis [*Thomas-Keprta et al.*, 2000]. The sixth characteristic, that the crystals are aligned in chains, is unlikely given that the crystals would have been clumped together after the bacteria's death due to their magnetic interaction. Tests for the presence of chains have been conducted and revealed that at most 10% of the grains are in isolated chains [*Weiss et al.*, 2004]. However, in a typical terrestrial sediment containing biogenic magnetite, more than 50% of the chains become disaggregated through diagenesis [*Mcneill and Kirschvink*, 1993] so the result is not conclusive of the original presence of chains. Laboratory and chemical alteration modeling calculations have shown that magnetite can be produced from the decomposition of iron-bearing carbonate [*Shearer et al.*, 1999; *Golden et al.*, 2004; *Treiman and Essene*, 2011], however these results have yet to demonstrate how the precise form of these unique magnetite crystals could have arisen, nor have they identified non-biological purification mechanisms for producing these pure iron oxide crystals from the unpure carbonate protolith.

2.0 Motivation

In the analyses to date there has not been a direct test of the probability that these particles are of detrital origin (as would be required in the biogenic hypothesis) vs. formed from the *in situ* decomposition of siderite ($FeCO_3$) [*Golden et al.*, 2001; *Golden et al.*, 2004; *Treiman and Essene*, 2011]. These two hypotheses lead to starkly contrasting predictions concerning the micron-scale arrangement of the tiny magnetite crystals. The McKay et al. hypothesis implies that magnetotactic bacteria were living in a fluid (likely within pore spaces, fractures, and voids within the rock) and as they died were deposited as clumped aggregates, then trapped in the carbonate, whereas the Golden/Treiman hypothesis argues that the magnetite crystals formed *in situ*, well distributed within the pre-existing carbonate matrix.

If it is possible to measure the magnetic moment of the magnetite within individual carbonate blebs from ALH84001, several rock magnetic techniques can be applied that can distinguish between these hypotheses. Fortunately, developments in the field of paleomagnetism and rock magnetism during the past decade have increased our ability to measure the magnetic moments, and magnetic properties, of tiny samples by nearly four orders of magnitude. Improvements in sensor design, scanning technology, and data analysis now permit quantitative measurement of particles only a few micrometers in size [*Weiss et al.*, 2007; *Lima and Weiss*, 2009; *Lima et al.*, 2013].

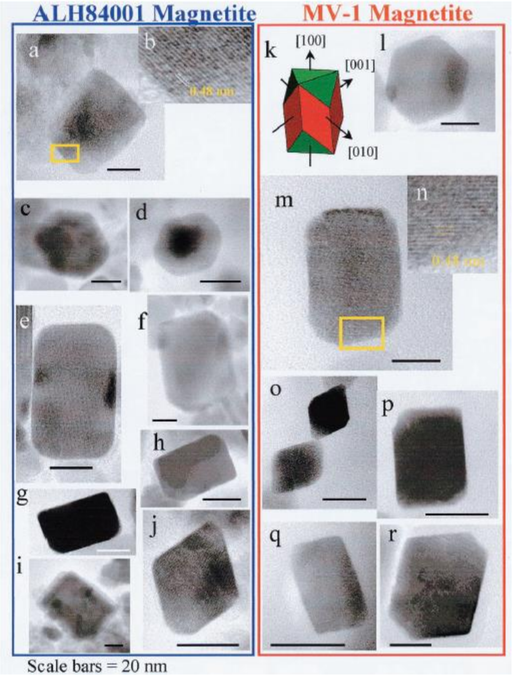

Figure 1. From Thomas-Keprta et al. [2000]. Comparison of magnetite crystals from ALH84001 and from magnetotactic bacteria.

We seek to test the hypothesis that the magnetite crystals that are presently imbedded in the carbonate blebs were trapped there from detrital aggregates present during carbonate precipitation. If this is false, and the crystals instead formed *in-situ* by solid-state or thermal decomposition processes, then the particles could not be the remnants of Martian magnetotactic bacteria. Deposition of carbonate within fractures in the sample represents a unique point in Mars time when there was warm (~18°C) water in contact with the atmosphere [*Halevy et al.*, 2011]. Most importantly, if the magnetites in ALH84001 are consistent with what is expected for biogenic magnetite, we may have uncovered a place in the solar system where life existed prior to its evolution on Earth. These bacteria would have existed long before the earliest known magnetotactic bacteria on Earth, from 1.8 Ga [*Chang and Kirschvink*, 1989; *Kopp and Kirschvink*, 2008; *Lin et al.*, 2017]. Furthermore, certain evolutionary characteristics are necessary for magnetotactic bacteria, such as cytoskeletons and intracellular membrane-bound organelles. Presumably if any of the ALH84001 magnetites are indeed biogenic these would far predate known life on Earth to when Mars hosted the necessary aqueous environmental conditions [*Halevy et al.*, 2011].

3.0 Methods

3.1 Paleomagnetism, in brief

Paleomagnetism is the study of magnetism recorded within rocks that was induced by an ancient magnetic field, usually a global magnetic field generated by a core dynamo. The magnetization present in a rock before laboratory analyses begin is known as the natural remanent magnetization (NRM) and it is the combination of original magnetization with any overprinting magnetization. Through laboratory measurements it is possible to determine the direction, intensity, stability, and duration of these ancient fields. By understanding how the rock became magnetized we can also learn about a rock's formation and its thermal and environmental history. The magnetization methods relevant to this study are discussed below and their rock magnetic properties are summarized in Table 1.

Detrital remanent magnetization (DRM) results in the aggregation of magnetic particles through a detrital process, such as deposition from a fluid (Figure 2). The particles will preferentially orient in the direction of any ambient magnetic field (Figure 2b). Because the particles are in a fluid they are subject to external forces and they may not be perfectly aligned with the ambient field, resulting in a weak magnetization in the direction parallel to the ambient field (Figure 2c). Additionally, after the particle is deposited and buried the sedimentary sequence may be subject to compaction, bioturbation, or other diagenetic process, further weakening their remanence. The magnetic nature of the particles causes them to clump as they are entrained within the sediments (Figure 2e). This process affects grains of all coercivities, though small single domain grains will be more easily aligned with the ambient field.

Chemical remanent magnetization (CRM) results when a rock undergoes an alteration process either from heating or from chemical interactions (Figure 3). The alteration process may cause the growth of magnetic particles (Figure 3b-d). As a grain grows in an ambient field it passes through distinct magnetic size regimes that dictate the grains ability to record a magnetic field. As the grains obtain the ability to record, they will record a bias in the direction of any ambient field (Figure 3d). This is an efficient form of magnetization because the grains are not subjected to other forces. The degree of alteration dictates the amount of inter-particle interaction (initially the process will produce well separated non-interacting grains but when fully altered the particles may be in close proximity and highly interacting). The size of the resulting magnetic grains will determine the coercivity of the magnetization recorded.

Shock or pressure remanent magnetization (SRM/PRM) is the acquisition of remanence during a shock event. The pressure wave which passes through the sample (Figure 4c-e) is related to this process and pressure remanent magnetization (PRM) and SRM are often discussed together. Although this method of magnetization is the hardest to study because of the extreme experiments that are required to produce shock events, it has been proposed that the shock events cause deformations within the crystals which lead to the acquisition of a remanence if an ambient field is present (Figure 4d-e) [*Cisowski et al.*, 1976]. The effects of impact processes are often seen in extraterrestrial samples [*Srnka et al.*, 1979]. Relatedly, it is possible that these impact fields may interact and amplify ambient fields on the surface [*Hood*, 1987; *Hood and Artemieva*, 2008]. This is an efficient form of magnetization because the grains are not subjected to other forces. The amount of inter-particle interaction will not change as a result of this process and will be determined by the distribution of particles in the sample. Laboratory shock experiments show that the low coercivity grains are preferentially affected by the shock process [*Gattacceca and Rochette*, 2004; *Shea et al.*, 2012].

Process	Efficiency	Inter-particle Interactions	Coercivity Range
Detrital	Low	High	All
Chemical	High	Variable	All
Shock	High	Variable	Low

Table 1: Comparison of rock magnetic properties of relevant remanent magnetization scenarios

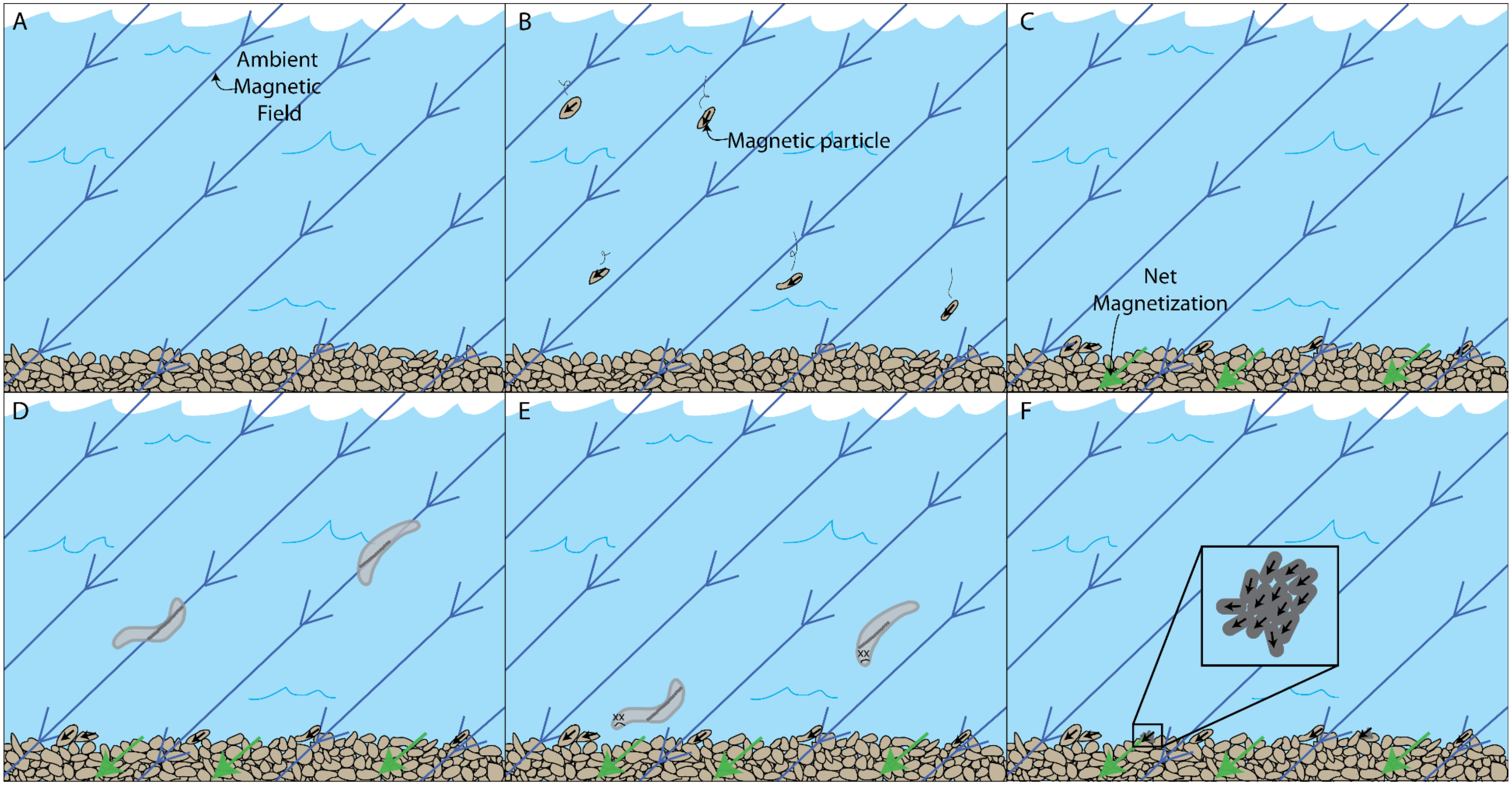

Figure 2. Detrital remanent magnetization. A) Water and sediment interact in the presence of an ambient magnetic field B) Magnetic particles present in the fluid preferentially align with the ambient field but are also subject to external forces C) As the magnetic particles become incorporated into the sediments a net magnetization is acquired in the general direction of the ambient field D) Magnetotactic bacteria align with the ambient magnetic field E) As the bacteria die they also become incorporated into the sediment F) The magnetic particles will clump together as they are deposited.

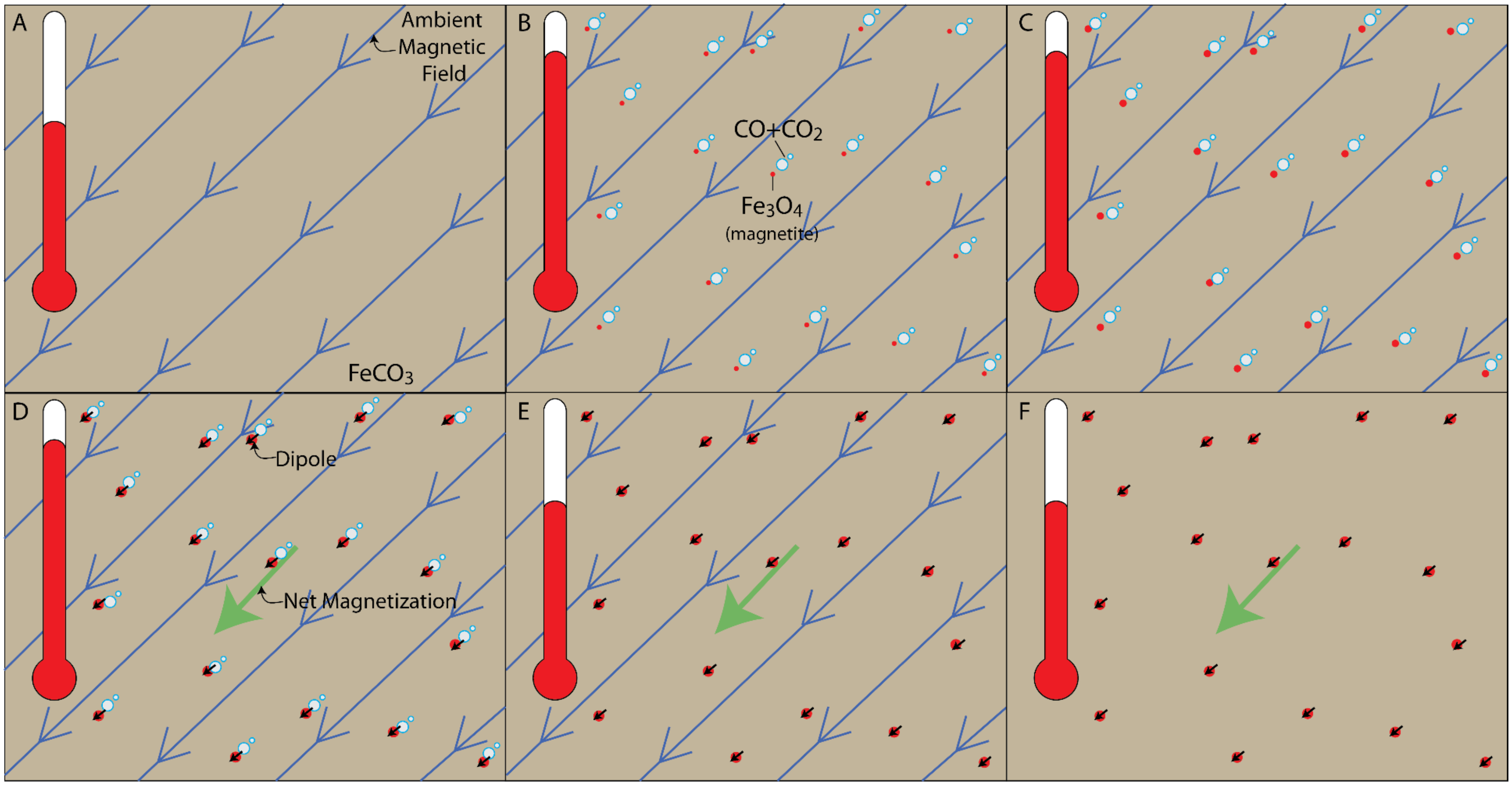

Figure 3. Chemical remanent magnetization. A) Siderite (FeCO3) at a stable temperature in an ambient magnetic field B) As the temperature increases siderite decomposes into magnetite (Fe3O4) and carbon monoxide and dioxide. C) The decomposition reaction continues. D) Eventually the magnetite crystals become large enough to acquire a remanent magnetization. E) As the temperature decreases the reaction stops and the rock remains magnetized. F) The magnetization remains after the ambient field leaves.

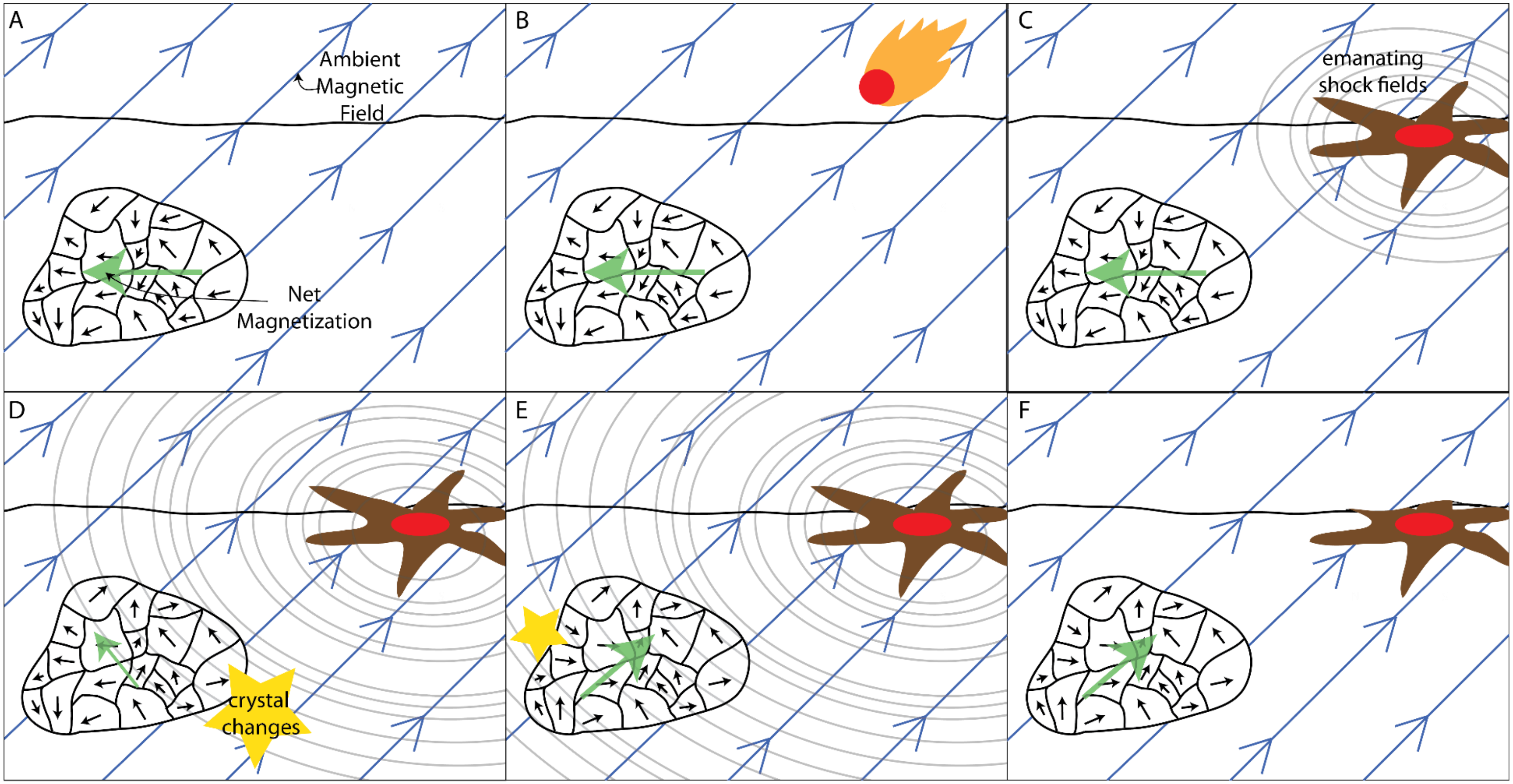

Figure 4. Shock Remanent Magnetization. A) A rock made of many magnetic domains sits on a planetary surface surrounded by an ambient magnetic field. B) An impactor approaches C) As the impactor hits the planet's surface shock/pressure waves emanate from the impact site D) The pressure waves hit the sample causing crystallographic changes which remagnetize the crystals in the direction of the ambient field, changing the net magnetization of the sample E) As the pressure wave leaves the sample the net magnetization is in agreement with the ambient field F) This magnetization persists even if the ambient field decays.

3.2 Unraveling a samples magnetic history through demagnetization

Because the remanent magnetization of a rock is the sum of all of the individual magnetic vectors, and because various processes affect magnetic grains differently (either through the grain's blocking temperature or its coercivity), it is possible for a rock to record the magnetization from various events. Therefore it is necessary to untangle the magnetic history recorded in the sample from the net magnetization observed initially. To do this we must systematically observe the magnetization recorded within discrete ranges of magnetic crystals (either their blocking temperature or coercivity or both). This is made possible through the use of demagnetization techniques that target crystals based on their coercivity or blocking temperatures. In the case of thermal demagnetization a sample is heated progressively in a zero field and the change in the magnetization is recorded after each heating step. This process can be destructive to the sample as minerals within the sample may react with the atmosphere of the oven at these high temperatures. To demagnetize the sample based on the coercivity of the grains within it we use alternating field (AF) demagnetization. In AF demagnetization, a decaying alternating magnetic field (Figure 5) is applied to the sample in three directions causing all magnetic particles with a coercivity lower than the peak field to acquire random magnetic directions, cancelling the net magnetization from those grains. The peak field is progressively increased until all of the magnetic remanence within the sample is randomized (removed).

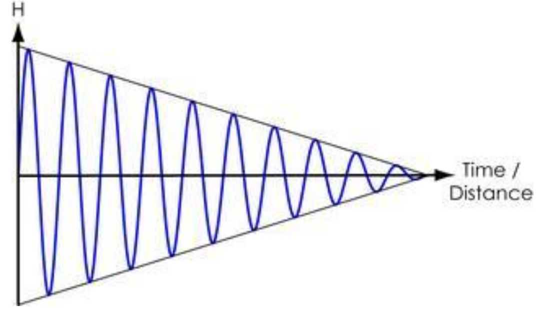

Figure 5. Alternating Field Demagnetization. Image from the public domain.

3.3 Classical rock magnetic techniques

3.3.1 Fuller Test of NRM

Around the time at which the carbonates formed at ~4 Ga, it has previously been established that Mars had a magnetic field of ~50 μT capable of imparting a remanent magnetization [*Weiss et al.*, 2008]. If the magnetite crystals grew in size via a solid-state process inside the carbonate blebs in a field of this strength, they would be unable to mechanically rotate as they become stably magnetized. Most magnetic moments would align in the direction of the local field, and the assemblage would be efficiently magnetized. In contrast, mature particles that are suspended in an aqueous solution are subject to Brownian motion that acts to disrupt their alignment, allowing their magnetic moments to clump [*Kobayashi et al.*, 2006], depending on the ambient field. This will reduce the net magnetization two to three orders of magnitude when compared to than those that are magnetized in place. A simple yet robust analysis based on these magnetization efficiency differences which distinguishes between chemical and depositional magnetization is the Fuller et al. [1988]test of natural remanent magnetization. The Fuller test uses information about the magnetic carriers, given by a strong isothermal remanent magnetization, while information about the magnetization process is given by the NRM. This test has been used extensively to distinguish between primary magnetization carried by detrital grains and secondary magnetization carried by authigenic magnetite (e.g., [*Hart and Fuller*, 1988]).

While the Fuller test of NRM is calibrated for the strength of Earth's magnetic field, coincidentally, previous paleointensity studies on ALH84001 have returned comparable Martian surface field strengths of ~ 50 μT [*Weiss et al.*, 2008].

3.3.2 Anhysteretic Remanent Magnetization (ARM) Susceptibility

When an alternating field is not perfectly symmetrical, either by laboratory error or intentionally, the result is ARM in the direction of the bias. The susceptibility, defined as the initial ratio of the intensity of the ARM with the strength of the applied field, of a sample to acquire this ARM varies based on the ability of the magnetic grains to interact. Interactions between single domain grains and the internal demagnetizing fields in multidomain grains provide a distribution of biasing fields that limit the ARM susceptibility [*Dunlop and Özdemir*, 2001]. Sugiura [1979] has demonstrated that as the concentration of single domain magnetites increases in a sample (and thus interaction between those magnetite grains) the ARM susceptibility decreases. Essentially, the ARM susceptibility probes the effective field strength between magnetic particles [*Cisowski*, 1981]. Although the concentration of magnetite in ALH84001 is low, the ARM susceptibility may be drastically different for the biogenic and abiogenic origins. The current abiogenic magnetite origin hypothesis involves partial decomposition of siderite to magnetite [*Treiman and Essene*, 2011] which would result in roughly equally spaced magnetite crystals dispersed throughout the carbonate blebs, yielding a high ARM acquisition slope. In the case of biogenic magnetite formation we would expect chains of magnetite to collapse into tight clusters as the magnetotactic bacterium dies and the magnetite grains are deposited, yielding a low ARM acquisition slope [*Kobayashi et al.*, 2006]. We applied the ARM susceptibility test on our carbonate grains and used natural siderite samples for comparison (a heated and altered siderite from Romanek [1994] and two unaltered siderite samples (from Roxbury, CT, USA and Ivittuut, Greenland)). Typically these results are also compared with Fe-bearing plagioclase as the non-interacting endmember and chiton teeth as the interacting endmember.

3.3.3 The Lowrie-Fuller Test

The coercivity of a magnetic particle describes how resistant the particle is to remagnetization by an external magnetic field. It is a function of size, shape, and mineralogy. In extremely small particles where the magnetization energy is less than thermal energy (kT), the magnetization is unstable; these particles are called superparamagnetic. Their magnetic moments dance around the local field direction, but do not preserve a memory of the magnetic direction. Much larger particles subdivide into multiple magnetic domains with magnetizations in different directions. As it is relatively easy to move domain boundaries and thereby shift a particle's net magnetization, multidomain grains are of fairly low coercivity. Only a narrow distribution of particle size and aspect ratio between these extremes produces single domain (SD) grains, which are of relatively high coercivity. It has long been known that magnetotactic bacteria produce particles that fall within this distribution [*Kirschvink and Lowenstam*, 1979], which allows them to maximize their stable magnetic moment while minimizing the amount of iron used. Pure bacterial magnetite therefore has a sharp coercivity distribution. The large fraction of magnetite particles from ALH84001 which fall into this narrow single-domain stability field for magnetite is one of the strong arguments for a biological origin [*Thomas-Keprta et al.*, 2000].

It is possible to determine the coercivity of the magnetic grains in a sample by the acquisition and demagnetization of isothermal remanent magnetization (IRM) and ARM through the Lowrie-Fuller test. Comparison of the demagnetization of these laboratory fields with that of the NRM also reveals the coercivity of magnetization.

3.3.4 Low temperature cycling

To assess the multi-domain component in the samples we cooled the samples to liquid nitrogen temperatures in a zero-field and measured the remanence before and after. The decrease in magnetization between these steps indicates what portion of the NRM may be from a multi-domain component.

3.3.5 Paleointensity

Several methods have been developed to determine the strength of a field responsible for the magnetization observed in a sample. We chose to apply relative paleointensity methods using ARM [*Tauxe*, 1993] and IRM [*Cisowski and Fuller*, 1986; *Fuller et al.*, 1988] which are non-destructive. Both methods are calibrated for thermal remanent magnetization, and therefore processes that are less efficient will give underestimates of the paleofield. Furthermore, these methods yield paleointensities within an order of magnitude of the paleofield.

To compute the paleointensity, the NRM demagnetization slope is normalized to the ARM or IRM acquisition slopes in at the same AF levels. We used an ARM bias field of 0.5 mT and an IRM acquired at 10 mT. The demagnetization fields used for comparison are 0, 5, 10, 25, 45, 60, (and where demagnetization data was available 80 and 103) mT. Ideally, the ratio should be constant throughout the demagnetization. We use calibration constants of f'=1.34 for the ARM paleointensity (see Yu et al. [2010]) and a= 3000 (see Kletetschka et al. [2004]). These calibration factors should be accurate to within a factor of 3-5 given the distribution of values observed in most natural samples (e.g., [*Cisowski et al.*, 1983; *Gattacceca and Rochette*, 2004; *Kletetschka et al.*, 2004; *Yu*, 2010].

3.4 SQUID microscopy

While many of the aforementioned paleomagnetic techniques have been in practice for decades, it was not possible until recently to conduct these tests on small samples because of instrument sensitivity. Now, through the use of ultra-high resolution scanning super conducting quantum interference device (SQuID) microscopy (referred from now on as SQuID microscopy) we are able to measure samples with magnetization as low as 7E-15 Am^2 [*Weiss et al.*, 2007]. SQuID microscopes utilize a pair of Josephson junctions, which are superconductors separated by two thin insulating barriers connected in a loop, across which a current can pass by quantum mechanical tunneling. The flux normal to the surface of the loop (actually, the vector potential, A, of the field in the gap) controls the current flowing across the Josephson junction, which can then be measured and converted to units of magnetic field. To measure the magnetic moment of a small sample, the sample is moved in a raster around the chip and the magnetic field is measured at all points. In order to minimize the necessary chip-to-sample distance a single chip is utilized and therefore the magnetic field is only measured in a single direction. In order to retrieve the magnetization direction of the sample the magnetic field map must be modeled with that of a dipole [*Lima and Weiss*, 2009]. Bulk magnetometers measure the magnetization vector in a single measurement whereas SQuID microscopes require, at a minimum, tens of points to obtain a good model of the magnetic field.

3.5 Sampling

The parent piece for our allocations of ALH84001 reside within the Antarctic meteorite collection at Johnson Space Center. For this study several carbonate disks found within fracture surfaces of ALH84001 were carefully flaked off the underlying pyroxenite using non-magnetic titanium needles. These flakes were then transported in a magnetically shielded container to Caltech. The majority of the carbonate flakes were very small and not easily further manipulated, however four flakes were large enough for analyses.

Because the samples are extremely small and therefore extremely weak, the moments observed through our magnetometer can easily be overwhelmed by the presence of dust or other noncarbonate particles. For this reason, we adopted the sample preparation technique of Fu et al. [2017] in which a piece of acid-washed quartz is milled with several holes behind which a thin (<100 μm) window remains. The four carbonate flakes were placed at the bottom of the holes and high-purity silica nanoparticles were packed in behind the flakes fixing them in position (Figure 6). The milled holder was taped onto a quartz disk 2.5 cm in diameter for ease of mounting on the instruments.

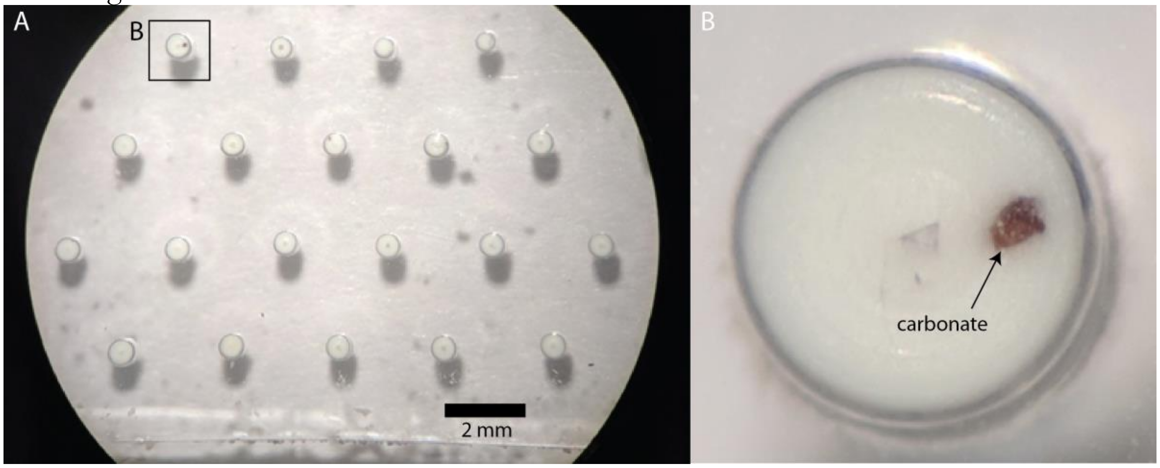

Figure 6. A. Milled holder B. Sample 1 within a milled holder and packed with silica.

3.6 Measurement

All processing techniques on the carbonates (application of AF field, IRM, and ARM) were conducted in a standard 2G magnetometer [*Kirschvink et al.*, 2008]. Aligning marks were placed on the quartz disk to ensure consistent placement of the sample holder into the SQuID microscope. After application of each laboratory field, the entire assembly was cleaned, covered in a thin sheet of Mylar, and placed against the measurement window of the SQUID microscope. Typical sensor-to-sample distances throughout this study were 250-400 μm. For measurement, the sample was rastered across the SQuID chip. Initial measurements used a grid spacing of 100 μm, but as the protocol improved, the step size was reduced to 50 μm.

Demagnetization of the carbonates consisted of AF fields applied in 0.5 mT steps from 1-47 mT, in 1 mT steps from 47-66 mT, in 20 mT steps to 70 mT, in 2.5 mT steps to 80 mT, in 5 mT steps to 95. Any remaining magnetization was removed at 10.3 and 430 mT steps. For rock magnetic tests, after full demagnetization, the sample was given an ARM bias of 0.025, 0.05, 0.1, 0.2, 0.35, 0.5, 0.65, and 0.9 mT in background fields of 100 mT. This ARM was then demagnetized at 5, 10, 25, 45, 60, 80, and 103 mT. The sample was then given a 100 mT IRM and demagnetized similarly. The sample was also subjected to a 0.5 mT ARM bias field with AF field strengths of 25, 37.5, 50, 63, 70, and 75. IRM acquisition was also measured at the same field strengths. Lastly, the sample was given an IRM at 37.5 and subjected to a low temperature cycle in a zero field to assess the amount of multi-domain carriers within the sample.

3.7 Dipole Fitting

Although the magnetic field we measure is only in the vertical direction, it is possible to determine the three-dimensional orientation of the magnetization measured. We used a dipole fitting routine modified from Lima and Weiss [2009] to determine the strength, direction, and location of the dipoles measured. This routine randomly modifies the available parameters until the residual between the model and the data is minimized. Because the individual carbonate blebs are separated from the bulk rock and each other the background field can be assumed to be zero. There is noise associated external magnetic fields and thermal fluctuations present around our instrument. We estimate the error on each dipole fit to be several x 10^{-14} Am^2 and within several degrees in direction, based on reproducibility of scans.

4. Results

4.1 Demagnetization

Each carbonate flake corresponded to a single dipole in our magnetic scans. For samples 1, 2, and 4 these were easily fit with a single dipole model. We also used a single dipole model for sample 3, however its magnetization was often ovoid rather than circular likely due to an elongate grain, causing higher scatter in dipole fits. Overall, we observe that the samples have a single, stable, magnetic component from AF 6 mT to total demagnetization (Figure 7). Unfortunately, initially the carbonate blebs were not properly fixed into their holders which resulted in their ability to jostle around during the first steps (AF 0 to AF 6 mT), before the problem was identified. We therefore have fixed the direction of the moment from AF 0 to AF 6 mT at the direction of the AF 6 mT step. Any directional information lost at these low coercivities would correspond to weak overprints on the original remanence.

We find that the majority of the magnetization is removed between 10 and 60 mT. Dipoles 1 and 3 had a fraction of very high coercivity magnetization that remained past 95 mT and was removed by our maximum AF step at 430 mT. Because the carbonates were flaked from the sample, it is not possible to compare the absolute directions measured from sample to sample. Higher scatter observed in the first demagnetization steps (< AF 15) are due to a coarser scanning grid used initially.

4.2 Fuller Test of NRM

The Fuller test of NRM revealed that the magnetization process responsible for the remanence in the samples was very efficient (Figure 8). All dipoles begin their magnetization in between 1:10 and 1:1 efficiency, which is in the range of chemical and shock remanent magnetization in Earth-strength fields. Dipoles 1, 2, and 4 remain within this range, whereas Dipole 3 crosses the 1:1 line at higher AF fields. Furthermore, demagnetization of their ARM (used as a thermal remanent magnetization proxy) was similar to the demagnetization of their NRM indicating that the NRM was carried by the same grains which were affected by the ARM.

4.3 ARM Acquisition

We observe that the carbonate particles experience significant inter-particle interaction (Figure 9). When compared with the Roxbury and Ivituut siderites and the Fe-bearing plagioclase, the ALH84001 dipoles are more interacting (have a shallower ARM susceptibility). However, when compared with a significantly altered piece of siderite from Romanek [1994] and chiton teeth, the ALH84001 dipoles are less interacting.

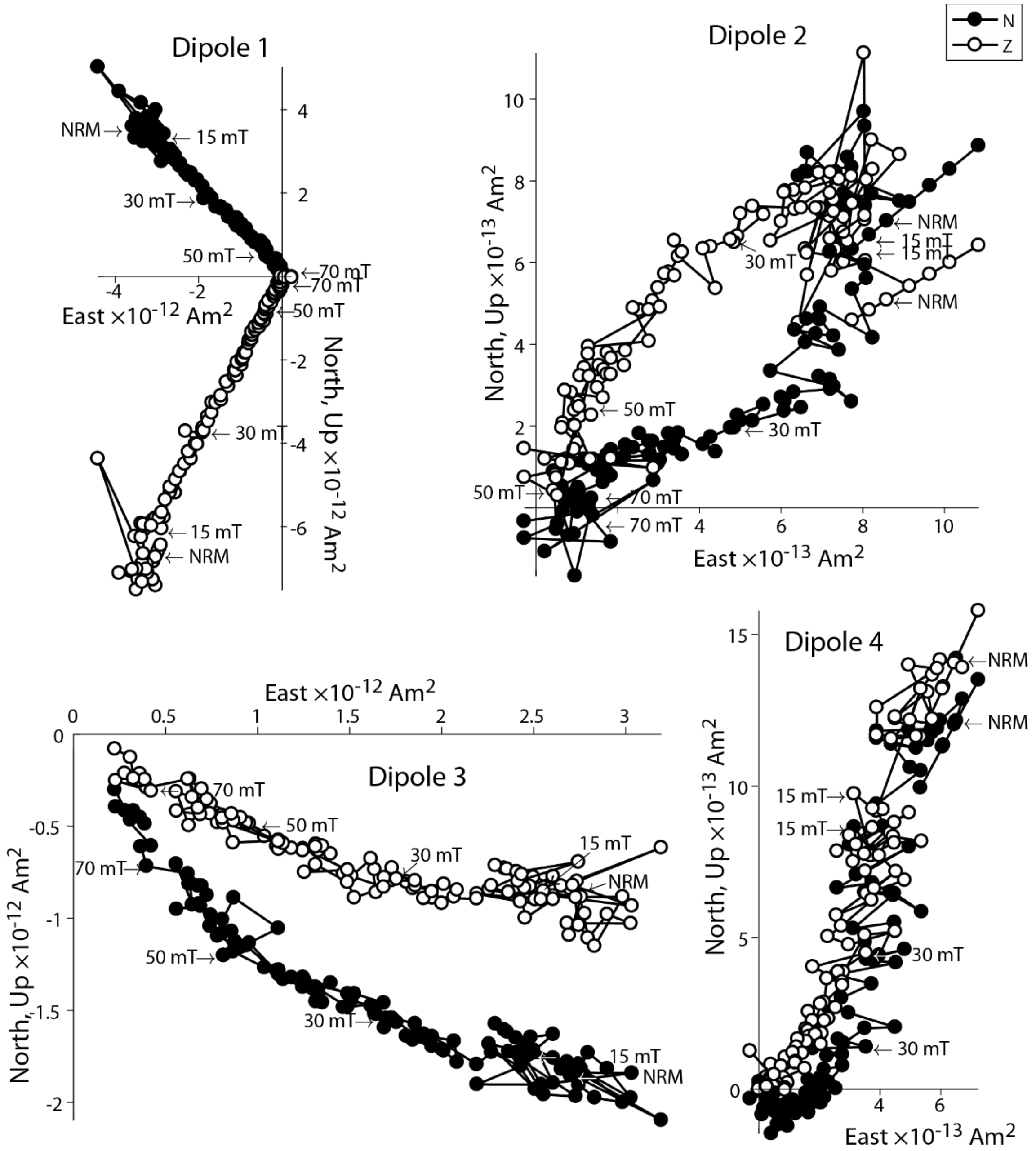

Figure 7

Demagnetization data for all four carbonate samples. Zijderveld plots are two dimensional representations of three dimensions with the vertical axis doubling as both Up and North. Closed and open symbols represent points projected onto horizontal N-S-E-W and vertical U-D-E-W planes, respectively. The nearly straight origin-trending movement from the NRM position to the origin indicate that the magnetization is unidirectional.

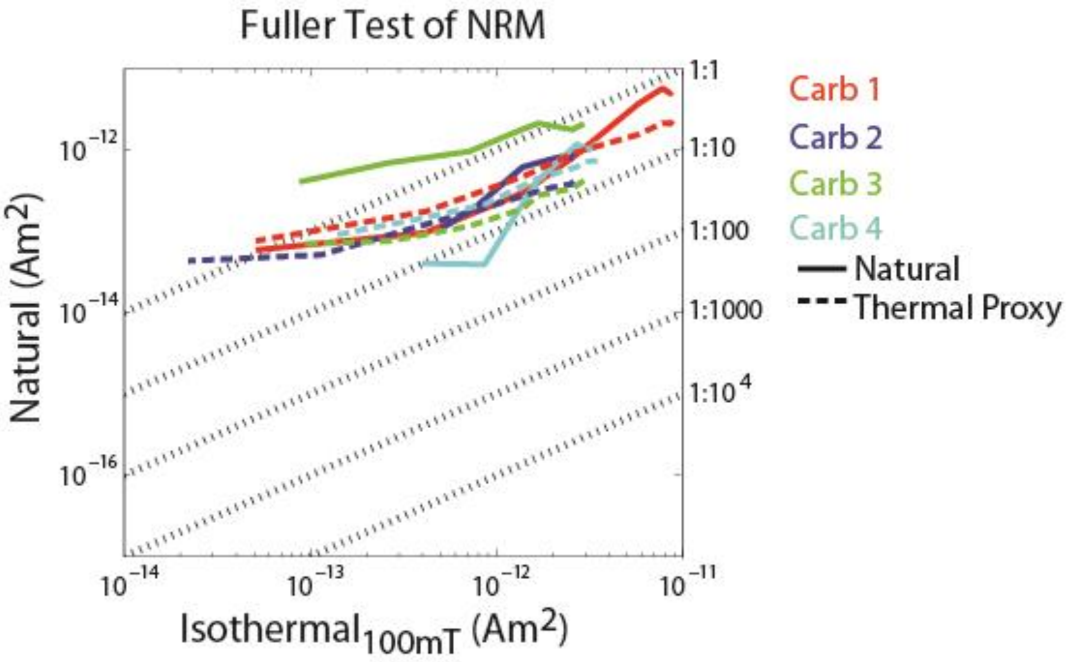

Figure 8. Comparison of NRM with demagnetization of IRM. Points included from right to left are AF 0, 5, 10, 25, 45, 60, and where available 80 and 103 mT.

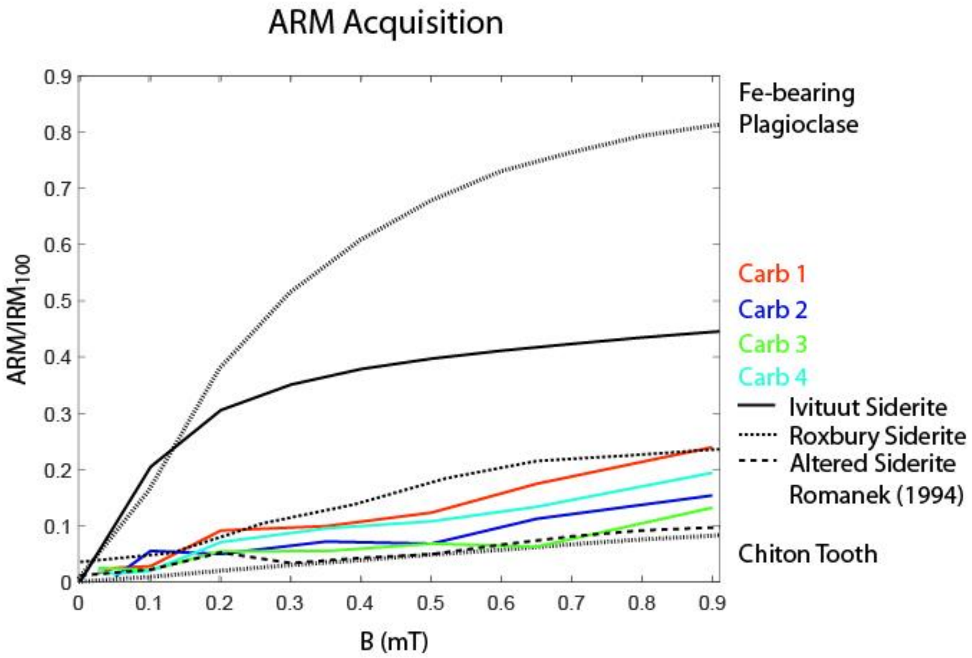

Figure 9. ARM acquisition curves for our samples plotted non-interacting curve from the Fe-bearing Lambert plagioclase and the strongly-interacting curve from Chiton teeth (S Cisowski, 1981) as well as pieces of a standard siderite sample (Roxbury) and a heavily altered heated siderite from Romanek et al. (1994).

4.4 Lowrie-Fuller Test and Low Temperature Cycling

Demagnetization of ARM and IRM reveals that the ARM produced a more stable magnetization than the IRM (Figure 10). This indicates the dominance of single domain grains within the samples. When both ARM and IRM are compared with the demagnetization of the NRM, we observe that the NRM magnetization is primarily carried in lower coercivity grains for dipoles 1, 2, and 4. However, for dipole 3 we see a roughly parallel demagnetization trend to the IRM demagnetization. The low temperature cycle for the samples revealed a loss of ~17% and ~27% of the total moment for dipoles 1 and 2. Changes in dipoles 3 and 4 were below the noise associated with the measurements (~several x 10^{-14} Am^2). This indicates that there is some fraction of multi-domain grains in dipoles 1 and 2 which may account for up to ~30% of the original observed NRM in these samples.

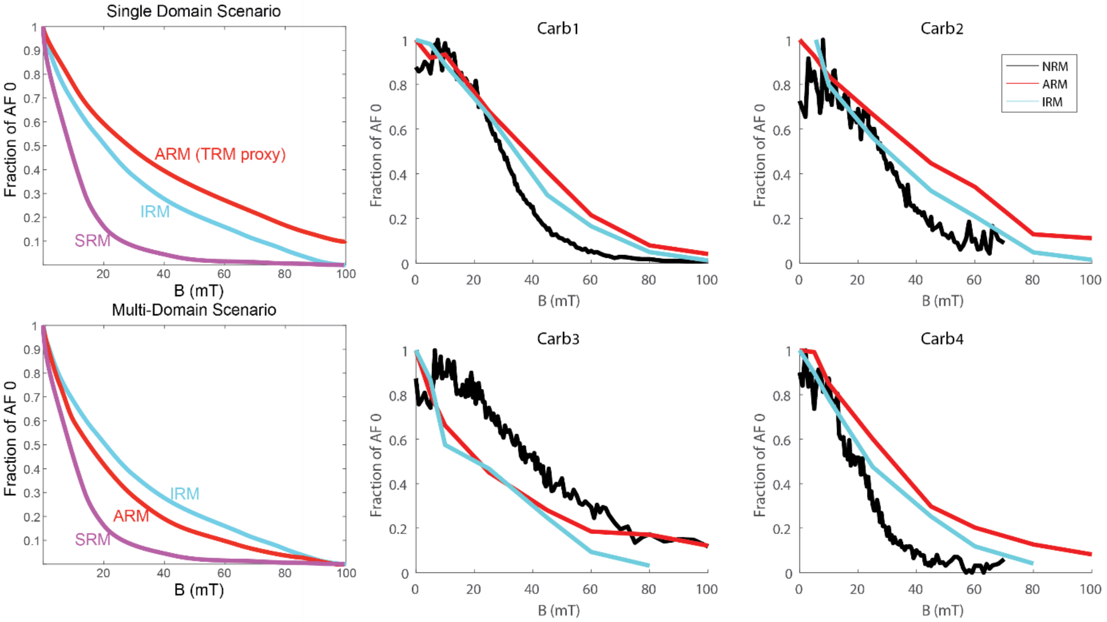

Figure 10. Comparison of demagnetization behavior for laboratory applied ARM and IRM with NRM. The data are normalized to the peak magnetic moment observed during demagnetization. The left-most plots are illustrative of the single and multi-domain scenarios.

4.5 Paleointensities

The IRM paleointensity experiment resulted in obvious positive correlation between the NRM lost and IRM gained at increasing demagnetizing fields (Figure 11). However, the ARM gained was erratic and did not yield to a well constrained ratio (Figure 12). We computed the average ratio of NRM lost to IRM and ARM gained by using the slopes (ratio of NRM to IRM or ARM) of the corresponding demagnetizations. We retrieve slopes between 0.38 and 0.88 for IRM paleointensity tests and between 2.11 and 3.68 for ARM paleointensity tests. These ratios correspond to paleointensities between 1 and 2 mT for the IRM method and 0.8 and 1.3 mT for the ARM method. These computed paleofield strength estimates should only be considered to within an order of magnitude of the absolute value. These methods are calibrated for low ratios of NRM to ARM or IRM (~0.1; (Weiss et al., 2008)) and therefore our use of them here is non-standard.

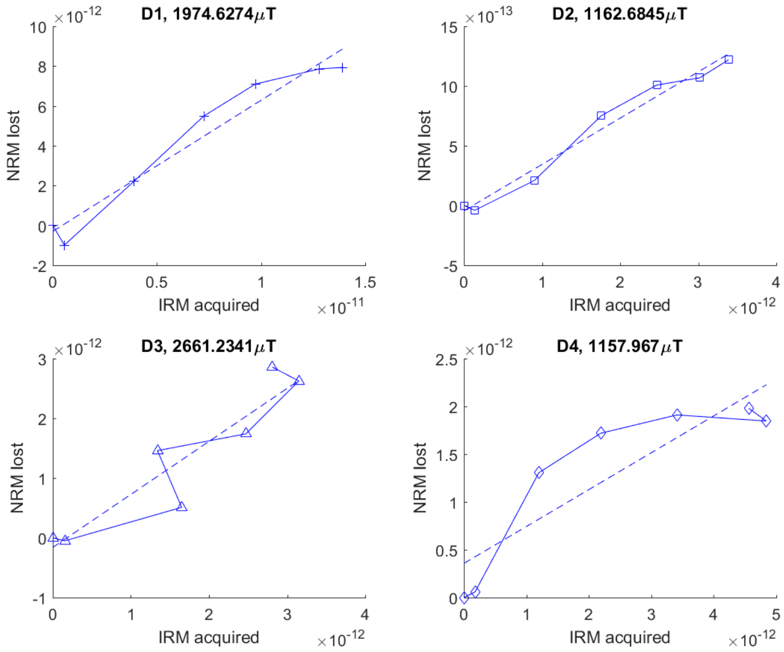

Figure 11. IRM paleointensity experiment results. Dashed lines indicate best fit lines to the data.

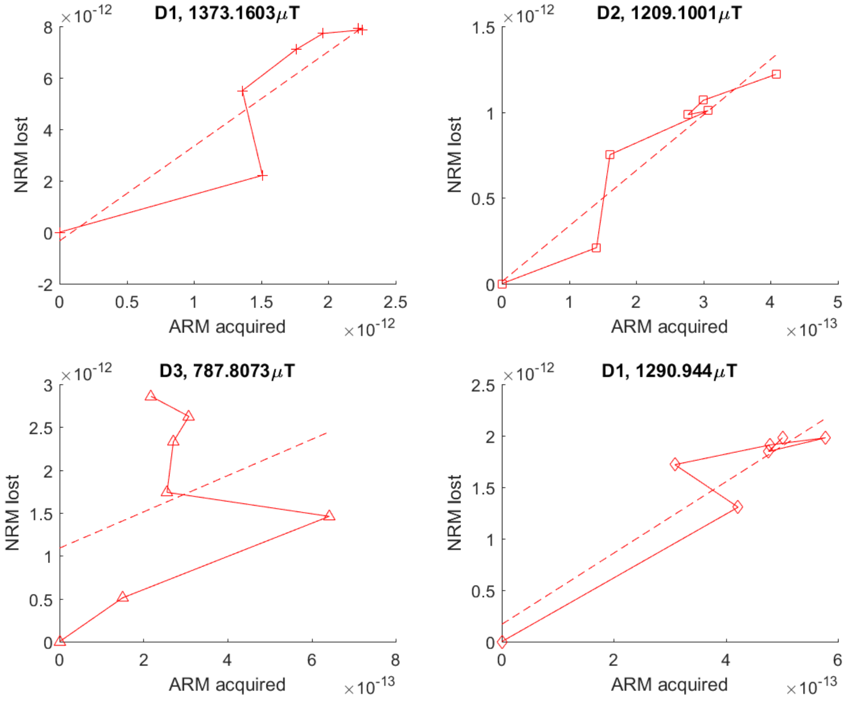

Figure 12. ARM paleointensity experiment results. Dashed lines indicate best fit lines to the data. While the NRM is consistently decreasing with AF field, the ARM acquisition is erratic.

5.0 Discussion

The simplest explanation for the consistently origin-trending demagnetization of the dipoles is that the magnetization for each sample was acquired through a single process. Any secondary process that may have imparted magnetization on the dipole after this would have had to only affect grains with coercivities less than 6 mT or have been acquired in an ambient field in the same direction as the remanence observed. The nature of the NRM, however, is less straightforward to explain.

The Fuller test of NRM reveals that the magnetization method responsible for the NRM observed in our samples is very efficient, comparable to a thermal, chemical, or shock remanence for dipoles 1, 2, and 4 and comparable to an IRM for dipole 3. The similarity between the ARM and the NRM further validates the result of this test. Because the Fuller test of NRM is calibrated for an Earth-strength field, the efficiencies presented here would have to be lower limits for weaker fields. Less efficient methods such as DRM would appear more efficient in a stronger field, however there is no evidence for a stronger field on Mars either through laboratory studies of Martian meteorites or modeling [*Weiss et al.*, 2008].

The ARM acquisition behavior of our four samples span the range from the slightly altered Roxbury siderite to the fully altered Romanek et al. (1994) siderite. Unfortunately, this range precludes an easy answer to the origin of the clumped nature of the magnetic particles within the samples. Although the samples are not clearly altered as in the Romanek et al. (1994) samples, it is possible that the carbonates are variably altered or that they do contain some fraction of clumped magnetic particles.

Perhaps the most elucidating data is present in the Lowrie-Fuller test and in the comparison of the demagnetization of the NRM with that of the laboratory fields. We will first discuss the magnetization of dipoles 1, 2, and 4 that behave similarly, then dipole 3. If the NRM of the dipoles 1, 2, and 3 were to be a result of IRM we would expect a decrease in moment similar to that observed in the demagnetization of the IRM (i.e., roughly monotonic). However, we actually observe that the NRM is removed mostly between 15 and 50 mT. A partial IRM overprint affecting these coercivities would similarly not explain the data because no change in direction is observed as the NRM is removed. We can therefore reject the hypothesis that the NRM is a result of an IRM. Similarly, the NRM behavior does not parallel the ARM, which is often a proxy for thermal/CRM. We therefore do not believe the magnetization observed is a result of one of these processes. In fact, the low-coercivity/soft magnetization observed with the NRM is similar to behavior seen with shock/pressure processes (e.g., Gattacceca et al. [2010]) that have been proposed to occur associated with large impacts [*Srnka et al.*, 1979; *Crawford and Schultz*, 1999; *Hood and Artemieva*, 2008]. There is much evidence for shock processes having affected ALH84001 [*Kirschvink et al.*, 1997; *Treiman*, 1998; *Eiler et al.*, 2002]. In the case of dipole 3, while more erratic, a comparison of the demagnetization of the NRM with the IRM shows that they are roughly parallel which may indicate that the remanence observed within this sample is related to an isothermal process, perhaps acquired during sample preparation.

Lastly, our paleointensity experiments resulted in paleofield strengths on the order of 1 mT (a factor of ~20 stronger than Earth's magnetic field today, and up to 2 orders of magnitude higher than previous paleointensity estimates for Mars. As previously mentioned, the paleointensity techniques are not well calibrated for ratios higher than ~0.1 and therefore the absolute intensity of the paleofield retrieved should not be trusted. However, it is clear that the paleofield strength required for the magnetization in these samples is exceptionally high. Also, as previously discussed, there is no evidence for fields of this strength on Mars. Because the demagnetization does not appear to be an IRM for dipoles 1, 2, and 4, again we revisit the possibility for a SRM or PRM. Models for the interaction of an impact field with an ambient magnetic field have concluded that the magnetic field may be concentrated/amplified and resulting in a field strength ~300 times the strength of the original field [*Hood*, 1987].

While the above scenario seems plausible, we must discuss the contradiction of this result with previous work on ALH84001, in particular that in which a weak paleofield has been previously calculated on ALH84001 using the magnetizations observed in the orthopyroxenite, both via analysis of individual dipoles [*Weiss et al.*, 2008] and analysis of bulk rock measurements [*Antretter et al.*, 2003]. The weak field calculated in Antretter et al [2003] is necessarily a lower limit given the previous observations that the magnetization of the sample is spatially heterogeneous within [*Kirschvink et al.*, 1997; *Weiss et al.*, 2000; *Weiss et al.*, 2002]. However, the paleofield estimations of Weiss et al. [2008] were conducted on individual magnetic anomalies, some of which are associated with carbonate. A look at the NRM/IRM ratio for the individual dipoles shows that four of the five outlier points (i.e., paleofield >200 μT, with a median value 34 μT) are associated with carbonate, none of these are associated with the fusion crust (see Supplementary Material of Weiss et al. [2008]). Still, these ratios are a factor of several below those calculated in this study. Given the range in NRM/IRM values observed in Weiss et al. [2008] and those calculated here, it may be possible that there is in fact a high range in this ratio throughout the sample. Many studies have noted that differences in results across studies of ALH84001 may have arisen because of the highly heterogeneous nature of the sample and the small sample allocations given to individual researchers. Therefore, we do not believe the different results to be problematic.

A SRM/PRM origin for the magnetization of ALH84001, while interesting, does not elucidate the debate about the potential biological formation of the magnetite within the ALH84001 carbonates. If the magnetite was already present in the carbonate prior to acquisition of the NRM, our ARM acquisition indicates that it may be potentially clumped. The Lowrie-Fuller test also indicates that the magnetization in the sample is primarily carried by single domain grains, which is also consistent with a biogenic origin. If the magnetite was instead formed through the shock process then it is not biogenic. However, it is not clear how this process – that of solid state diffusion – would lead to clumping of the particles, even during a brief episode of shock. It is also unclear how the shock process occurred without significant heating of the carbonate. Some of the magnetite has been suggested to have originated from condensation in a vapor phase [*Bradley et al.*, 1996].

6.0 Conclusions

We find that the magnetization process for all four carbonate samples is highly efficient, the inter-particle interactions are moderately interacting, the samples are predominantly single domain and that the remanence is carried primarily in the low coercivity range (except for dipole 3). The magnetization scenario that best explains the results of these tests (for carbonates 1, 2 and 4) is SRM/PRM. The remanence in sample 3 appears to be a saturating IRM, possibly from magnetic contamination during preparation. Typically, a sample can be given a laboratory PRM for comparison but the nature of our microscopic samples and their holder precludes this.

The data presented here still cannot definitely rule out a biogenic origin for the magnetite within the ALH84001 carbonates. More complicated scenarios exist in which the magnetite is detrital and then later shocked. Furthermore, the most tentative aspect of this work is the reliance on paleofield strength estimates that are used to interpret the results of the Fuller test of NRM. If the ancient magnetic field was considerably stronger, a DRM origin may still be plausible. Furthermore, the single domain dominance in the samples would be consistent with a biogenic origin. At this time the previous work on the paleofield strength, which indicates an Earth-strength field, is the best estimate we have.

7.0 References

Antretter, M., M. Fuller, E. Scott, M. Jackson, B. Moskowitz, and P. Solheid (2003), Paleomagnetic record of Martian meteorite ALH84001, *J Geophys Res-Planet*, *108*, 5049, doi:10.1029/2002je001979.

Bradley, J. P., R. P. Harvey, and H. Y. McSween, Jr. (1996), Magnetite whiskers and platelets in the ALH84001 Martian meteorite: evidence of vapor phase growth, *Geochim Cosmochim Acta*, *60*, 5149-5155, doi:10.1016/S0016-7037(96)00383-3.

Chang, S. B. R., and J. L. Kirschvink (1989), Magnetofossils, the Magnetization of Sediments, and the Evolution of Magnetite Biomineralization, *Annu. Rev. Earth Planet. Sci.*, *17*, 169-195, doi:10.1146/annurev.earth.17.1.169.

Cisowski, S. (1981), Interacting Vs Non-Interacting Single Domain Behavior in Natural and Synthetic Samples, *Phys. Earth Planet. Inter.*, *26*, 56-62, doi:10.1016/0031-9201(81)90097-2.

Cisowski, S. M., D. W. Collinson, S. K. Runcorn, A. Stephenson, and M. Fuller (1983), A review of lunar paleointensity data and implications for the origin of lunar magnetism, *J. Geophys. Res.*, *88*, A691, doi:10.1029/JB088iS02p0A691.

Cisowski, S. M., J. R. Dunn, M. Fuller, Y. Wu, M. F. Rose, and P. J. Wasilewski (1976), Magnetic effects of shock and their implications for lunar magnetism. II, in *Proceedings of the Seventh Lunar Science Conference*, p. 3299-3320, Pergamon Press, Inc., New York.

Cisowski, S. M., and M. Fuller (1986), Lunar paleointensities via the IRMs normalization method and the early magnetic history of the moon, paper presented at Origin of the moon, 411-424, Lunar and Planetary Institute, 1986.

Crawford, D. A., and P. H. Schultz (1999), Electromagnetic properties of impact-generated plasma, vapor and debris, *Int. J. Impact Eng.*, *23*, 169-180, doi:10.1016/S0734-743x(99)00070-6.

Dunlop, D. J., and Ö. Özdemir (2001), *Rock magnetism: fundamentals and frontiers*, 3, Cambridge University Press.

Eiler, J. M., J. W. Valley, C. M. Graham, and J. Fournelle (2002), Two populations of carbonate in ALH84001: Geochemical evidence for discrimination and genesis, *Geochim. Cosmochim. Acta*, *66*, 1285-1303, doi:10.1016/S0016-7037(01)00847-X.

Fu, R. R., et al. (2017), Evaluating the paleomagnetic potential of single zircon crystals using the Bishop Tuff, *Earth Planet. Sci. Lett.*, *458*, 1-13, doi:10.1016/j.epsl.2016.09.038.

Fuller, M., S. Cisowski, M. Hart, R. Haston, E. Schmidtke, and R. Jarrard (1988), Nrm-Irm(S) Demagnetization Plots - an Aid to the Interpretation of Natural Remanent Magnetization, *Geophys. Res. Lett.*, *15*, 518-521, doi:10.1029/GL015i005p00518.

Gattacceca, J., M. Boustie, L. Hood, J. P. Cuq-Lelandais, M. Fuller, N. S. Bezaeva, T. de Resseguier, and L. Berthe (2010), Can the lunar crust be magnetized by shock: Experimental groundtruth, *Earth Planet. Sci. Lett.*, *299*, 42-53, doi:10.1016/j.epsl.2010.08.011.

Gattacceca, J., and P. Rochette (2004), Toward a robust normalized magnetic paleointensity method applied to meteorites, *Earth Planet. Sci. Lett.*, *227*, 377-393, doi:10.1016/j.epsl.2004.09.013.

Gibson, E. K., D. S. McKay, K. L. Thomas-Keprta, S. J. Wentworth, F. Westall, A. Steele, C. S. Romanek, M. S. Bell, and J. Toporski (2001), Life on Mars: evaluation of the evidence within Martian meteorites ALH84001, Nakhla, and Shergotty, *Precambrian Research*, *106*, 15-34, doi:10.1016/S0301-9268(00)00122-4.

Golden, D. C., D. W. Ming, R. V. Morris, A. Brearley, H. V. Lauer, A. H. Treiman, M. E. Zolensky, C. S. Schwandt, G. E. Lofgren, and G. A. McKay (2004), Evidence for exclusively inorganic formation of magnetite in Martian meteorite ALH84001, *American Mineralogist*, *89*, 681-695, doi:10.2138/am-2004-5-602.

Golden, D. C., D. W. Ming, C. S. Schwandt, H. V. Lauer, R. A. Socki, R. V. Morris, G. E. Lofgren, and G. A. McKay (2001), A simple inorganic process for formation of carbonates, magnetite, and sulfides in Martian meteorite ALH84001, *American Mineralogist*, *86*, 370-375, doi:10.2138/am-2001-2-321.

Halevy, I., W. W. Fischer, and J. M. Eiler (2011), Carbonates in the martian meteorite Allan Hills 84001 formed at 18±4 C in a near-surface aqueous environment, *Proc. Natl. Acad. Sci*, *108*, 16895-16899, doi:10.1073/pnas.1109444108.

Hart, M., and M. Fuller (1988), Magnetization of a Dolomite Bed in the Monterey Formation - Implications for Diagenesis, *Geophys. Res. Lett.*, *15*, 491-494, doi:10.1029/GL015i005p00491.

Hood, L. L. (1987), Magnetic field and remanent magnetization effects of basin-forming impacts on the Moon, *Geophys. Res. Lett.*, *14*, 844-847, doi:10.1029/GL014i008p00844.

Hood, L. L., and N. A. Artemieva (2008), Antipodal effects of lunar basin-forming impacts: Initial 3D simulations and comparisons with observations, *Icarus*, *193*, 485-502, doi:10.1016/j.icarus.2007.08.023.

Kirschvink, J. L., R. E. Kopp, T. D. Raub, C. T. Baumgartner, and J. W. Holt (2008), Rapid, precise, and high-sensitivity acquisition of paleomagnetic and rock-magnetic data: Development of a low-noise automatic sample changing system for superconducting rock magnetometers, *Geochemistry Geophysics Geosystems*, *9*, 1-18, doi:10.1029/2007gc001856.

Kirschvink, J. L., and H. A. Lowenstam (1979), Mineralization and Magnetization of Chiton Teeth - Paleomagnetic, Sedimentologic, and Biologic Implications of Organic Magnetite, *Earth Planet. Sci. Lett.*, *44*, 193-204, doi:10.1016/0012-821x(79)90168-7.

Kirschvink, J. L., A. T. Maine, and H. Vali (1997), Paleomagnetic evidence of a low-temperature origin of carbonate in the Martian meteorite ALH84001, *Science*, *275*, 1629-1633, doi:10.1126/science.275.5306.1629.

Kletetschka, G., M. H. Acuna, T. Kohout, P. J. Wasilewski, and J. E. P. Connerney (2004), An empirical scaling law for acquisition of thermoremanent magnetization, *Earth Planet. Sci. Lett.*, *226*, 521-528, doi:10.1016/j.epsl.2004.08.001.

Kobayashi, A., J. L. Kirschvink, C. Z. Nash, R. E. Kopp, D. A. Sauer, L. E. Bertani, W. F. Voorhout, and T. Taguchi (2006), Experimental observation of magnetosome chain collapse in magnetotactic bacteria: Sedimentological, paleomagnetic, and evolutionary implications, *Earth Planet. Sci. Lett.*, *245*, 538-550, doi:10.1016/j.epsl.2006.03.041.

Kopp, R. E., and J. L. Kirschvink (2008), The identification and biogeochemical interpretation of fossil magnetotactic bacteria, *Earth-Sci Rev*, *86*, 42-61, doi:10.1016/j.earscirev.2007.08.001.

Lima, E. A., and B. P. Weiss (2009), Obtaining vector magnetic field maps from single-component measurements of geological samples, *J. Geophys. Res.*, *114*, doi:10.1029/2008JB006006.

Lima, E. A., B. P. Weiss, L. Baratchart, D. P. Hardin, and E. B. Saff (2013), Fast inversion of magnetic field maps of unidirectional planar geological magnetization, *J. Geophys. Res.*, *118*, 2723-2752, doi:10.1002/jgrb.50229.

Lin, W., et al. (2017), Origin of microbial biomineralization and magnetotaxis during the Archean, *Proc Natl Acad Sci U S A*, *114*, 2171-2176, doi:10.1073/pnas.1614654114.

McKay, D. S., E. K. Gibson, Jr., K. L. Thomas-Keprta, H. Vali, C. S. Romanek, S. J. Clemett, X. D. Chillier, C. R. Maechling, and R. N. Zare (1996), Search for past life on Mars: possible relic biogenic activity in martian meteorite ALH84001, *Science*, *273*, 924-930, doi:10.1126/science.273.5277.924.

Mcneill, D. F., and J. L. Kirschvink (1993), Early Dolomitization of Platform Carbonates and the Preservation of Magnetic Polarity, *J. Geophys. Res.*, *98*, 7977-7986, doi:10.1029/93jb00353.

Romanek, C. S., M. M. Grady, I. P. Wright, D. W. Mittlefehldt, R. A. Socki, C. T. Pillinger, and E. K. Gibson, Jr. (1994), Record of fluid-rock interactions on Mars from the meteorite ALH84001, *Nature*, *372*, 655-657, doi:10.1038/372655a0.

Shea, E. K., B. P. Weiss, W. S. Cassata, D. L. Shuster, S. M. Tikoo, J. Gattacceca, T. L. Grove, and M. D. Fuller (2012), A long-lived lunar core dynamo, *Science*, *335*, 453-456, doi:10.1126/science.1215359.

Shearer, C. K., L. A. Leshin, and C. T. Adcock (1999), Olivine in Martian meteorite Allan Hills 84001: Evidence for a high-temperature origin and implications for signs of life, *Meteoritics & Planetary Science*, *34*, 331-339, doi:10.1111/j.1945-5100.1999.tb01343.x.

Srnka, L. J., G. Martelli, G. Newton, S. M. Cisowski, M. D. Fuller, and R. B. Schaal (1979), Magnetic field and shock effects and remanent magnetization in a hypervelocity impact experiment, *Earth Planet. Sci. Lett.*, *42*, 127-137, doi:10.1016/0012-821x(79)90198-5.

Sugiura, N. (1979), Arm, Trm and Magnetic-Interactions - Concentration-Dependence, *Earth Planet. Sci. Lett.*, *42*, 451-455, doi:10.1016/0012-821x(79)90054-2.

Tauxe, L. (1993), Sedimentary Records of Relative Paleointensity of the Geomagnetic-Field - Theory and Practice, *Rev. Geophys.*, *31*, 319-354, doi:10.1029/93rg01771.

Thomas-Keprta, K. L., D. A. Bazylinski, J. L. Kirschvink, S. J. Clemett, D. S. McKay, S. J. Wentworth, H. Vali, E. K. Gibson, Jr., and C. S. Romanek (2000), Elongated prismatic magnetite crystals in ALH84001 carbonate globules: potential Martian magnetofossils, *Geochim Cosmochim Acta*, *64*, 4049-4081, doi:10.1016/S0016-7037(00)00481-6.

Thomas-Keprta, K. L., S. J. Clemett, D. A. Bazylinski, J. L. Kirschvink, D. S. McKay, S. J. Wentworth, H. Vali, E. K. Gibson, Jr., M. F. McKay, and C. S. Romanek (2001), Truncated hexa-octahedral magnetite crystals in ALH84001: presumptive biosignatures, *Proc Natl Acad Sci U S A*, *98*, 2164-2169, doi:10.1073/pnas.051500898.

Treiman, A. H. (1998), The history of Allan Hills 84001 revised: multiple shock events, *Meteorit Planet Sci*, *33*, 753-764, doi:10.1111/j.1945-5100.1998.tb01681.x.

Treiman, A. H., and E. J. Essene (2011), Chemical composition of magnetite in Martian meteorite ALH 84001: Revised appraisal from thermochemistry of phases in Fe-Mg-C-O, *Geochim. Cosmochim. Acta*, *75*, 5324-5335, doi:10.1016/j.gca.2011.06.038.

Weiss, B. P., L. E. Fong, H. Vali, E. A. Lima, and F. J. Baudenbacher (2008), Paleointensity of the ancient Martian magnetic field, *Geophys. Res. Lett.*, *35*, doi:10.1029/2008gl035585.

Weiss, B. P., S. S. Kim, J. L. Kirschvink, R. E. Kopp, M. Sankaran, A. Kobayashi, and A. Komeili (2004), Magnetic tests for magnetosome chains in Martian meteorite ALH84001, *Proc Natl Acad Sci U S A*, *101*, 8281-8284, doi:10.1073/pnas.0402292101.

Weiss, B. P., J. L. Kirschvink, F. J. Baudenbacher, H. Vali, N. T. Peters, F. A. Macdonald, and J. P. Wikswo (2000), A low temperature transfer of ALH84001 from Mars to Earth, *Science*, *290*, 791-795, doi:10.1126/science.290.5492.791.

Weiss, B. P., E. A. Lima, L. E. Fong, and F. J. Baudenbacher (2007), Paleomagnetic analysis using SQUID microscopy, *J. Geophys. Res.*, *112*, doi:10.1029/2007jb004940.

Weiss, B. P., H. Vali, F. J. Baudenbacher, J. L. Kirschvink, S. T. Stewart, and D. L. Shuster (2002), Records of an ancient Martian magnetic field in ALH84001, *Earth Planet. Sci. Lett.*, *201*, 449-463, doi:10.1016/S0012-821x(02)00728-8.

Yu, Y. (2010), Paleointensity determination using anhysteretic remanence and saturation isothermal remanence, *Geochemistry Geophysics Geosystems*, *11*, Q02Z12, doi:10.1029/2009gc002804.

Chapter 5

POTENTIAL TRUE POLAR WANDER OBSERVED IN ALH84001

Jennifer Buz[1], Tristan G. Murphy[1], Joseph L. Kirschvink[1,2],
[1]Department of Geologic and Planetary Sciences, California Institute of Technology, Pasadena, CA 91125, U.S.A. [2]Earth-Life Science Institute, Tokyo Institute of Technology, Meguro, 152-8550 Tokyo, Japan.

Abstract

Martian meteorite ALH84001 has a long and varied history recording multiple shock events as well as an episode of carbonate deposition from a fluid. Each thermal, aqueous, or shock event allows the sample to record the ambient magnetic field present on Mars at the time. We have scanned the magnetization recorded within slices of ALH84001 and fit for any identifiable dipoles. We used Bingham statistics to fit the dipoles and found that they lie in a coplanar distribution. One possible interpretation for this distribution of dipoles is true polar wander (TPW) on Mars. Previous studies using a variety of techniques also find that TPW likely occurred on Mars.

1. Introduction

1.1 What we know about Mars' magnetic past

Mars does not have a global magnetic field (dipole moment < ~2 x 10^{18} Am^2) today, however Mars had a magnetic field generated by a core dynamo at some point in its past [*Acuna et al.*, 1998]. The presence of an ancient magnetic field has been established both through analyses of Martian meteorites, which preserve original magnetization [*Collinson*, 1997; *Kirschvink et al.*, 1997; *Weiss et al.*, 2002b; *Weiss et al.*, 2008], and by the observation that large portions of the ancient crust of Mars are magnetized [*Acuna et al.*, 1998; *Acuna et al.*, 1999]. These crustal anomalies are of comparable or greater strength to crustal anomalies on Earth [*Acuna et al.*, 1998; *Connerney et al.*, 1999; *Purucker et al.*, 2000]. The majority of these anomalies are present in the ancient cratered terrain, however, there is an absence of magnetization in/around large impact basins such as Hellas and Argyre [*Acuna et al.*, 1999]. The longevity and lifetime of the dynamo is less certain.

Following these crustal magnetization observations many studies were aimed at understanding the evolution of the Martian core and its effect on a Martian core dynamo [e.g., *Stevenson*, 2001]. Models which combine inferred geologic age of magnetized crustal material get ranges of core dynamo cessation as late as 3.6 Ga [*Milbury et al.*, 2012] or as early as 4.14 Ga [*Vervelidou et al.*, 2017]. However, results from the study the magnetization recorded in Martian meteorites requires an ambient magnetic field at the surface as late as 1.3 Ga (albeit very weak; [*Collinson*, 1997]). Geophysical models constraining the lifetime of the magnetic field and its strength indicate a maximum core lifetime of several hundred million years [*Stevenson*, 2001]. Despite the apparent strong magnetization observed from orbit [*Acuna et al.*, 1999; *Connerney et al.*, 1999], all previous estimates of the surface magnetic field strength place it as weaker or comparable to Earth's current field (~50 µT; [*Collinson*, 1997; *Kirschvink et al.*, 1997; *Stevenson*, 2001; *Antretter et al.*, 2003; *Weiss et al.*, 2008]. The strong magnetization observed may arise from the high concentration of magnetic phases in some geological terranes [*Gattacceca et al.*, 2014].

1.2 ALH84001

ALH84001 is a Martian meteorite of orthopyroxene that crystallized ~4.1 Ga [*Lapen et al.*, 2010] with accessory carbonates forming at ~3.9 Ga [*Borg et al.*, 1999]. Paleomagnetic studies on portions of ALH84001 revealed that it records a Martian magnetic field [*Collinson*, 1997; *Kirschvink et al.*, 1997; *Weiss et al.*, 2000; *Weiss et al.*, 2002b]. In addition to the geophysical implications for this magnetization, the fact that the magnetization exists after transfer from Mars to Earth means that the interior of the meteorite was not heated significantly during this process [*Kirschvink et al.*, 1997; *Weiss et al.*, 2000]. Additionally, paired thermochronology results indicate that the ALH84001 carbonates obtained their magnetization prior to 3.9 Ga and have been well below their blocking temperature (the temperature below which they lock in their magnetization) since their formation [*Weiss et al.*, 2002a; *Weiss et al.*, 2002b]. The shock history of the sample is extensive [*Treiman*, 1998], and paleomagnetic analysis of the sample can lead to information about magnetic fields present on Mars during alteration of the meteorite. A thorough review of the sample petrogenesis and history is given in the appendix.

1.3 Motivation

Because ALH84001 records a long a varied history on Mars and has the potential to record the ambient magnetic field during each thermal, shock, or alteration event in its past, we seek to assess the distribution of magnetization present within the sample. It has been previously established that the sample records a magnetization that does not appear to be unidirectional [*Kirschvink et al.*, 1997; *Weiss et al.*, 2002b], but does this magnetization fit into any other well-described distributions and if so what are the interpretations of these distributions?

2.0 Methods

We scanned each available slice of ALH84001 in our collection using the superconducting quantum interference device (SQuID) microscope in order to assess the distribution of directions of the individual magnetic anomalies present within the bulk rock. Although the magnetic field we measure is only in the vertical direction, it is possible to determine the three-dimensional orientation and magnitude of the magnetization measured using the dipole fitting routine modified from Lima and Weiss (2009. This routine randomly modifies the available parameters until the residual between the model and the data is minimized. Because the individual carbonate blebs are separated from the bulk rock and from each other, the background field can be assumed to be zero. However, in our thick sections the presence of neighboring dipoles complicates the model fitting. There is also noise associated external magnetic fields and thermal fluctuations present around our instrument. We estimate the error on each dipole fit to be several x 10^{-14} Am^2 and within several degrees in direction, based on reproducibility of scans. We then used Bingham statistics on the collection of dipoles to determine if there were any observable trends in the magnetization. We specifically test for uniformity against a bipolar alternative in which dipoles are distributed among two directions. We represent each dipole as a unit vector and multiply it by the principal direction for the set of dipoles. We then compare this to the critical value for the null hypothesis that they are uniformly distributed. The specific statistic used is given below:

$$S = \frac{1}{n}\sum_{i=1}^{n}(\mu x_i + \alpha y_i + \beta z_i)^2$$

where (μ, α, β) are the direction cosines of the principal axis, (x, y, z) are the individual dipole coordinates, and n is the number of dipoles. The critical values for rejecting the model of uniformity are found in Pearson and Hartley [1972]. We also tested for uniformity against a unimodal alternative. The specific statistic used is given below:

$$\chi^2 = \frac{3}{n}[(\sum x_i)^2 + (\sum y_i)^2 + (\sum z_i)^2]$$

and the critical values are from Stephens (1964).

3.0 Results

We measured a total of 96 dipoles within two series of ALH84001 slices. An example of one set of slices and their corresponding magnetic field maps is shown in Figure 1. The distribution of observed directions from both sets is seen in Figure 2. We applied the Bingham statistic on each set of dipoles. We find that we are able to reject the null hypothesis of uniformity against a bipolar alternative for both sets of dipoles. However, in the case of a test against a unimodal alterative we are only able to reject the null hypothesis for the larger dipole set. Our statistics are available in Table 1.

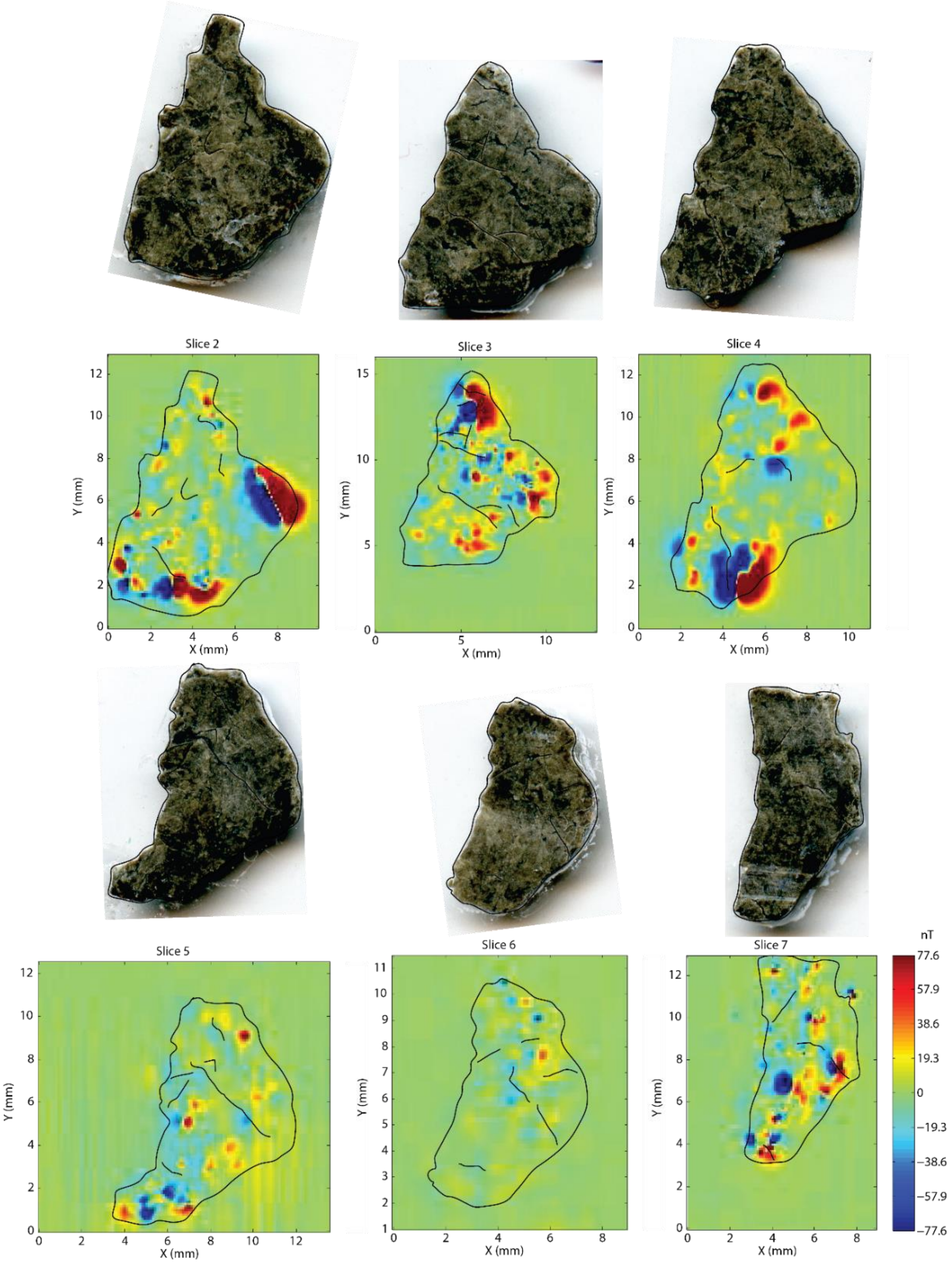

Figure 1. Progressive slices of ALH84001 and their corresponding magnetization maps.

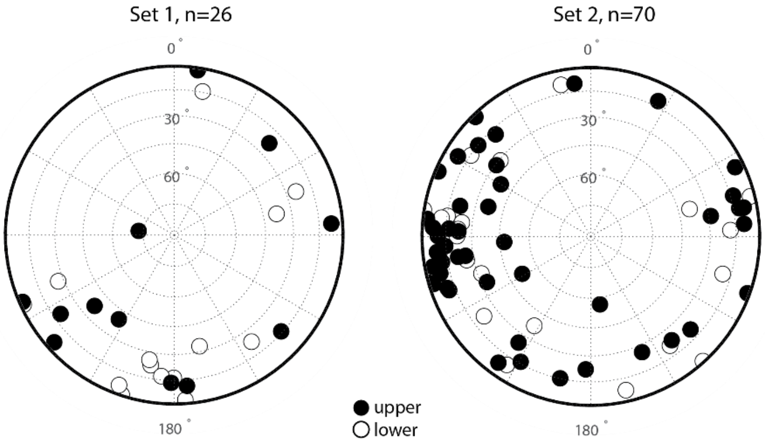

Figure 2. Stereographic projection showing distribution of dipole directions.

	Set 1	Set 2
n	26	70
Bimodal, S	0.1263	0.1193
Critical Value 99%	0.201	0.258
Reject Null?	Yes	Yes
Unimodal, χ^2	14.59	31.53
Critical Value 99%	12.2	45.44
Reject Null?	No	Yes

Table 1. Statistics used for test of uniformity against a bipolar and unimodal alternatives.

4.0 Discussion

A previous study on individual dipoles found within ALH84001 was unable to exclude the possibility of uniformly distributed directions [*Weiss et al.*, 2008] when the region surrounding the fusion crust was excluded (however, the sample size was limited to 23 dipoles after exclusion of the fusion crust). The possibility for a unimodal dipole distribution is interesting and consistent with previous studies showing a net magnetization within the meteorite [*Antretter et al.*, 2003]. The possibility for a bimodal distribution however, is even more intriguing because of the implications such a result could have. This distribution is associated with two unique directions and a distribution of dipoles within them. Such a phenomenon could be associated with slow movement of the sample during acquisition of the magnetization, or, movement of the background field during that same time. The latter scenario could be explained by true polar wander (TPW).

TPW is the solid body rotation of a mass about its rotation axis. When this occurs on a planet with a core dynamo, because the core dynamo maintains its orientation relative to the spin axis, the magnetic field found on the body's surface will change throughout the rotation. Mars, being a body with a varied topography (e.g., the northern lowlands, southern highlands, Tharsis volcanic province, and large impact basins such as Hellas) would have likely experienced TPW. Evidence for TPW has been presented before through the observation of potential polar deposits at low latitudes [*Schultz and Lutz*, 1988], through modeling of geoid deformation [*Sprenke and Baker*, 2000; *Perron et al.*, 2007], and through modeling of magnetic anomalies to determine paleopole positions [*Milbury et al.*, 2012; *Thomas et al.*, 2018]. The timing of TPW is not well constrained but has been predicted to have begun starting in the early Noachian [*Johnson and Phillips*, 2005] and lasting potentially until 2 Ga [*Perron et al.*, 2007]. Therefore, TPW occurring during magnetization of ALH84001 is possible.

There are two caveats associated with our study of dipole distributions. First, our study was conducted on thick sections of the meteorite and therefore some of the dipoles are found within the interior of the sample and their precise location is hard to determine. Furthermore, the additional material contributes to a strong observable magnetization present throughout the sample (i.e., a background field) which increases the error associated with dipole fitting. Second, we selected dipoles visually for analysis. Because horizontally oriented dipoles have a clear positive-negative pairing, there is a potential for sampling bias. Indeed, we find that in both slice sequences the dipoles appear to be roughly in the horizontal direction. At this time, we are unable to orient the two slice sequences relative to each other with respect to their declinations, however they were sliced relative to the same initial sawblade cut and therefore their inclinations are in common.

A third consideration for the potential of TPW preserved within ALH84001 is the timing of the magnetization of ALH84001. The sample would have needed to be actively recording the ambient field throughout any apparent TPW. We do know, through this study and prior analyses, that there is both magnetization observed associated with the orthopyroxenite and with the carbonates [*Weiss et al.*, 2008]. We also know that these two lithologies formed at separate times. Lastly, it has been observed through various methods that the sample has been shocked numerous times [*Treiman*, 1998]. It is therefore possible that ALH84001 may in fact sample multiple orientations of the Mars core dynamo throughout its lifetime on Mars.

5.0 Conclusions

The distribution of dipoles within several slices of ALH84001 is consistent with a bimodal distribution of magnetic directions. A bimodal distribution can be explained by the sample moving as it acquired a magnetization or by the ambient field changing relative to the sample. The latter explanation is consistent with TPW which is previously thought to occur on Mars. ALH84001, through its varied history and variety of magnetic minerals may record TPW. Further studies which distinguish the magnetizations observed and their associated mineralogies will elucidate the results presented here.

6.0 Appendix

6.1 ALH84001: Discovery and Classification

ALH84001 (Figure A1) was collected on December 27, 1984 in the Allan Hills of Antarctica as part of the US Antarctic meteorite survey program. It was initially classified as a diogenite (a deep crustal rock presumed to have originated from the asteroid Vesta) because of the abundance of orthopyroxene. However, the concentration of Fe^{3+}, the presence of pyrite and carbonate, and the large discrepancy in TiO_2/Al_2O_3 and FeO/MnO ratios between and ALH84001 and other diogenites made it a known outlier within this group [*Berkley and Boyton*, 1992; *Mittlefehldt*, 1994a; *Mittlefehldt*, 1994b].

Figure A1. ALH84001 prior to processing. The smooth black exterior covering the left half and top of the sample are a fusion crust, glassy material remaining from melting upon entering the Earth atmosphere. NASA photo #S85-39570.

6.2 Petrology

ALH84001 is a coarse grained, cataclastic, orthopyroxenite (>95% orthopyroxene, grains up to 6 mm in diameter) with chromite (~2%), maskelynite (~1%), carbonate (~1%), and minor Cr-spinel, olivine, augite, pyrite, whitlockite, pyrrhotite, and magnetite [*Berkley and Boyton*, 1992; *Mittlefehldt*, 1994b; *McKay et al.*, 1996; *Shearer et al.*, 1999]. Common carbonates on small fractures are absent to minor in other Martian samples. Two populations of carbonates exist: carbonate disks, and massive ankerite presumed to have formed from shock melted carbonate disks [*Eiler et al.*, 2002]. Carbonates in the former population range in size from ~10-300 μm in diameter and ~10-50 μm in thickness (Figure A2) and have a general disk or pancake-like shape [*McKay et al.*, 1996; *Eiler et al.*, 2002; *Thomas-Keprta et al.*, 2009]. These carbonates are zoned and typically surrounded by a black-white-black rim (Figure A2). Magnetite is found within the rim, contributing to its dark color, but also dispersed within the carbonate centers in lesser abundance [*Thomas-Keprta et al.*, 2009]. Some of these disks exhibit fractures indicating that they were formed prior to a shock event (e.g., nearby meteorite impact), while other carbonates lie upon shock fractures indicating their formation (or at least relocation) after a shock event [*Mittlefehldt*, 1994b]. The larger of the carbonates disks are zoned from Fe-rich centers, to Ca-rich, to nearly pure magnesite sometimes followed by a second sequence of thin bands of sequential Fe, Ca, and Mg rich carbonates, indicating possible fluid replenishment or temperature fluctuations during formation [*Mittlefehldt*, 1994b; *Romanek et al.*, 1994]. Although initial studies suggested a high temperature origin for the carbonate disks [*Mittlefehldt*, 1994b; *Harvey and McSween*, 1996], more recent isotope and magnetic analyses on the carbonate disks indicate formation in a near-surface aqueous environment at approximately 18 °C [*Romanek et al.*, 1994; *Kirschvink et al.*, 1997; *Valley et al.*, 1997; *Halevy et al.*, 2011].

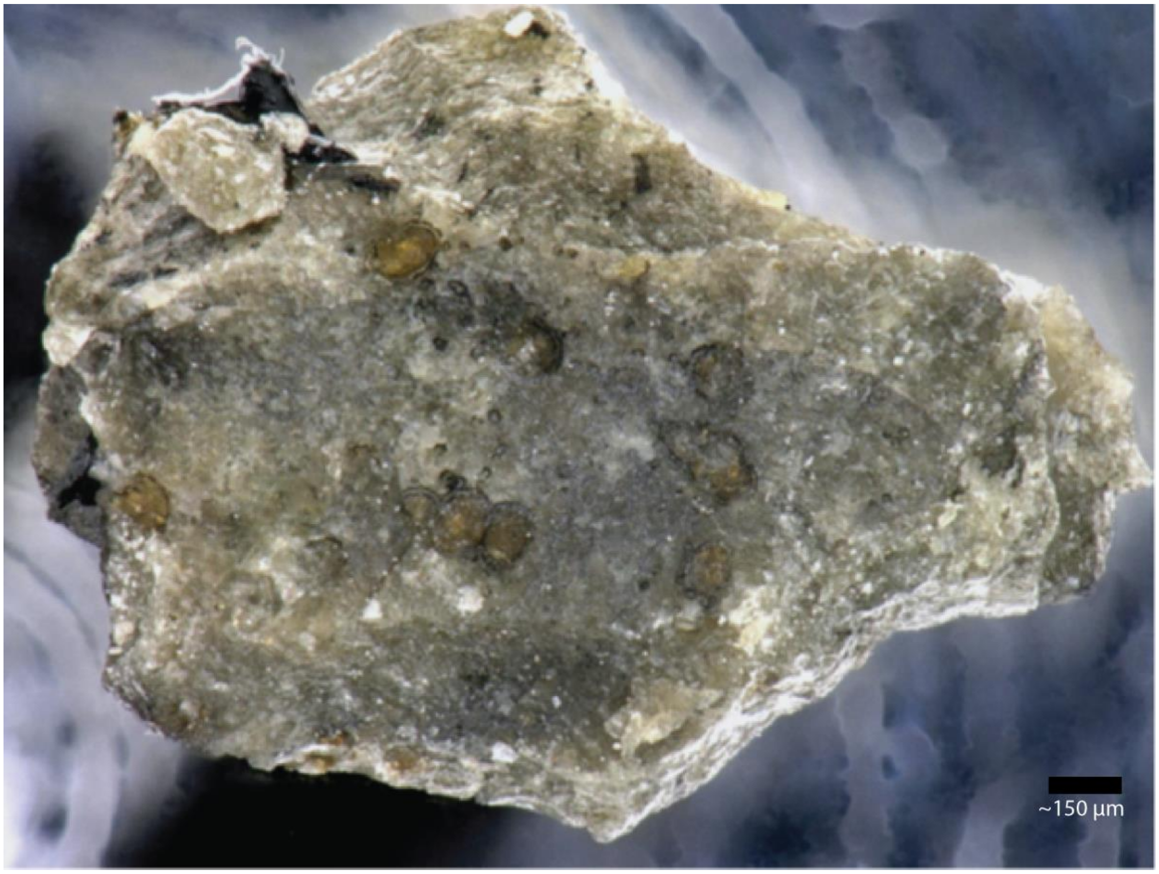

Figure A2. Optical image of fracture surface of ALH84001 taken by K. Thomas-Keprta. The carbonate disks with black-white-black rims are visible.

6.3 Thermal History

The varied textures, minerals, and their relationships to each other have enabled reconstruction of its thermal history [*Mittlefehldt*, 1994b; *Treiman*, 1995; 1998]. The large pyroxene grains and their composition lead to the common interpretation that ALH84001 originated as an igneous cumulate [*Mittlefehldt*, 1994b]. Several crushed zones within the meteorite have been identified and interpreted to have occurred during a shock event (or two, e.g. Treiman [1998]). These crushed zones are annealed indicating that the rock underwent thermal metamorphism, enough to cause recrystallization, after the shock event (and maybe associated with it). On some of the fracture surfaces the carbonate disks have been emplaced, which as previously mentioned must have occurred in a wet, low-temperature, near-surface environment, representing an alteration event for the sample [*Mittlefehldt*, 1994b; *Romanek et al.*, 1994; *Treiman*, 1995; 1998; *Halevy et al.*, 2011]. Finally, some of these carbonates themselves exhibit shock fractures indicating at least a second shock event [*Mittlefehldt*, 1994b; *Treiman*, 1995; 1998]. The meteorite has therefore undergone at least two shock events (potentially up to five [*Treiman,* 1998]) and at least one episode of fluid interaction prior to its arrival at Earth.

The age of ALH84001 has been of considerable interest due to its clear separate petrogenesis from the other Martian meteorites and because of its recording of at least two shock events, indicating a likely ancient age. Many studies have been aimed at dating both the orthopyroxene component and the later carbonate deposit(s) (see Nyquist et al. [2001] and references therein). The original age determinations using Sm-Nd and Rb-Sr resulted in a formation age ~4.5 Ga [*Jagoutz et al.*, 1994; *Nyquist et al.*, 1995]. However, recent work using Lu-Hf and Pb-Pb have yielded a much younger age of ~4.1 Ga [*Bouvier et al.*, 2009; *Lapen et al.*, 2010]. Some interpretations include the older formation age with some chronometers reset at ~4.0 Ga during later impact processes (e.g. Nyquist et al [2001]). A large range in age estimates has also been the case for the carbonates with an ages as young as 1.41 Ga [*Wadhwa and Lugmair*, 1996] and as old as ~4.0 Ga [*Borg et al.*, 1999]. The 3.9 Ga Rb-Sr age for the carbonates [*Borg et al.,* 1999] is generally accepted because of the ability through this method to isolate the carbonate itself (i.e. Nyquist et al. [2001]). This age is relevant to the zoned carbonate disks, however, and does not imply an age for the second population of carbonates (discussed prior) interpreted to have been a product of melting of the disks (e.g. Eiler et al. [2002]). Many cosmic ray exposure ages have been determined for the sample using ^{3}He, ^{31}Ne, ^{81}Kr, and ^{38}Ar and all lie between 14-18 Ma [*Miura et al.*, 1995; *Swindle et al.*, 1995; *Eugster et al.*, 1997; *Nyquist et al.*, 2001; *Eugster et al.*, 2010]. Finally, 14C has been used to determine the residence time on Earth as ~13 ka [*Jull et al.*, 1995].

7.0 References

Acuna, M. H., et al. (1999), Global distribution of crustal magnetization discovered by the mars global surveyor MAG/ER experiment, *Science*, *284*, 790-793, doi:10.1126/science.284.5415.790.

Acuna, M. H., et al. (1998), Magnetic field and plasma observations at Mars: Initial results of the Mars global surveyor mission, *Science*, *279*, 1676-1680, doi:10.1126/science.279.5357.1676.

Antretter, M., M. Fuller, E. Scott, M. Jackson, B. Moskowitz, and P. Solheid (2003), Paleomagnetic record of Martian meteorite ALH84001, *J Geophys Res-Planet*, *108*, 5049, doi:10.1029/2002je001979.

Berkley, J. L., and N. J. Boyton (1992), Minor/major element variation within and among diogenite and howardite orthopyroxenite groups, *Meteoritics*, *27*, 387-394, doi:10.1111/j.1945-5100.1992.tb00220.x.

Borg, L. E., J. N. Connelly, L. E. Nyquist, C. Y. Shih, H. Wiesmann, and Y. Reese (1999), The age of the carbonates in martian meteorite ALH84001, *Science*, *286*, 90-94, doi:10.1126/science.286.5437.90.

Bouvier, A., J. Blichert-Toft, and F. Albarede (2009), Martian meteorite chronology and the evolution of the interior of Mars, *Earth Planet. Sci. Lett.*, *280*, 285-295, doi:10.1016/j.epsl.2009.01.042.

Collinson, D. W. (1997), Magnetic properties of Martian meteorites: Implications for an ancient Martian magnetic field, *Meteoritics & Planetary Science*, *32*, 803-811, doi:10.1111/j.1945-5100.1997.tb01571.x.

Connerney, J. E., M. H. Acuna, P. J. Wasilewski, N. F. Ness, H. Reme, C. Mazelle, D. Vignes, R. P. Lin, D. L. Mitchell, and P. A. Cloutier (1999), Magnetic lineations in the ancient crust of mars, *Science*, *284*, 794-798, doi:10.1126/science.284.5415.794.

Eiler, J. M., J. W. Valley, C. M. Graham, and J. Fournelle (2002), Two populations of carbonate in ALH84001: Geochemical evidence for discrimination and genesis, *Geochim. Cosmochim. Acta*, *66*, 1285-1303, doi:10.1016/S0016-7037(01)00847-X.

Eugster, O., H. Busemann, S. Lorenzetti, and D. Terribilini (2010), Ejection ages from krypton-81-krypton-83 dating and pre-atmospheric sizes of martian meteorites, *Meteoritics & Planetary Science*, *37*, 1345-1360, doi:10.1111/j.1945-5100.2002.tb01033.x.

Eugster, O., A. Weigel, and E. Polnau (1997), Ejection times of Martian meteorites, *Geochim. Cosmochim. Acta*, *61*, 2749-2757, doi:10.1016/S0016-7037(97)00115-4.

Gattacceca, J., P. Rochette, R. B. Scorzelli, P. Munayco, C. Agee, Y. Quesnel, C. Cournede, and J. Geissman (2014), Martian meteorites and Martian magnetic anomalies: A new perspective from NWA 7034, *Geophys. Res. Lett.*, *41*, 4859-4864, doi:10.1002/2014gl060464.

Halevy, I., W. W. Fischer, and J. M. Eiler (2011), Carbonates in the martian meteorite Allan Hills 84001 formed at 18±4 C in a near-surface aqueous environment, *Proc. Natl. Acad. Sci*, *108*, 16895-16899, doi:10.1073/pnas.1109444108.

Harvey, R. P., and H. Y. McSween, Jr. (1996), A possible high-temperature origin for the carbonates in the martian meteorite ALH84001, *Nature*, *382*, 49-51, doi:10.1038/382049a0.

Jagoutz, E., A. Sorowka, J. D. Vogel, and H. Wanke (1994), ALH 84001: alien or progenitor of the SNC family?, paper presented at Meteoritics 29, 478-479.

Johnson, C. L., and R. J. Phillips (2005), Evolution of the Tharsis region of Mars: insights from magnetic field observations, *Earth Planet. Sci. Lett.*, *230*, 241-254, doi:10.1016/j.epsl.2004.10.038.

Jull, A. J. T., C. J. Eastoe, S. Xue, and G. F. Herzog (1995), Isotopic Composition of Carbonates in the Snc Meteorites Allan-Hills-84001 and Nakhla, *Meteoritics*, *30*, 311-318, doi:10.1111/j.1945-5100.1995.tb01129.x.

Kirschvink, J. L., A. T. Maine, and H. Vali (1997), Paleomagnetic evidence of a low-temperature origin of carbonate in the Martian meteorite ALH84001, *Science*, *275*, 1629-1633, doi:10.1126/science.275.5306.1629.

Lapen, T. J., M. Righter, A. D. Brandon, V. Debaille, B. L. Beard, J. T. Shafer, and A. H. Peslier (2010), A younger age for ALH84001 and its geochemical link to shergottite sources in Mars, *Science*, *328*, 347-351, doi:10.1126/science.1185395.

McKay, D. S., E. K. Gibson, Jr., K. L. Thomas-Keprta, H. Vali, C. S. Romanek, S. J. Clemett, X. D. Chillier, C. R. Maechling, and R. N. Zare (1996), Search for past life on Mars: possible relic biogenic activity in martian meteorite ALH84001, *Science*, *273*, 924-930, doi:10.1126/science.273.5277.924.

Milbury, C., G. Schubert, C. A. Raymond, S. E. Smrekar, and B. Langlais (2012), The history of Mars' dynamo as revealed by modeling magnetic anomalies near Tyrrhenus Mons and Syrtis Major, *J Geophys Res-Planet*, *117*, n/a-n/a, doi:10.1029/2012je004099.

Mittlefehldt, D. W. (1994a), ALH84001, a cumulate orthopyroxenite member of the martian meteorite clan, *Meteoritics*, *29*, 214-221, doi:10.1111/j.1945-5100.1994.tb00673.x.

Mittlefehldt, D. W. (1994b), The Genesis of Diogenites and Hed Parent Body Petrogenesis, *Geochim. Cosmochim. Acta*, *58*, 1537-1552, doi:10.1016/0016-7037(94)90555-X.

Miura, Y. N., K. Nagao, N. Sugiura, H. Sagawa, and K. Matsubara (1995), Orthopyroxenite Alh84001 and Shergottite Alh77005 - Additional Evidence for a Martian Origin from Noble-Gases, *Geochim. Cosmochim. Acta*, *59*, 2105-2113, doi:10.1016/0016-7037(95)00130-1.

Nyquist, L. E., B. M. Bansal, H. Weisman, and C.-Y. Shih (1995), Martians young and old: zagami and ALH 84001, paper presented at Lunar and Planetary Sciences Conference XXII, 1065-1066, 1995.

Nyquist, L. E., D. D. Bogard, C.-Y. Shih, A. Greshake, D. Stöffler, and O. Eugster (2001), Ages and Geologic Histories of Martian Meteorites, in *Chronology and Evolution of Mars*, p. 105-164, Springer, Dordrecht.

Pearson, E. S., and H. O. Hartley (1972), *Biometrika Tables for Satisticians*, 2, Cambridge University Press, Cambridge.

Perron, J. T., J. X. Mitrovica, M. Manga, I. Matsuyama, and M. A. Richards (2007), Evidence for an ancient martian ocean in the topography of deformed shorelines, *Nature*, *447*, 840-843, doi:10.1038/nature05873.

Purucker, M., D. Ravat, H. Frey, C. Voorhies, T. Sabaka, and M. Acuna (2000), An altitude-normalized magnetic map of Mars and its interpretation, *Geophys. Res. Lett.*, *27*, 2449-2452, doi:10.1029/2000gl000072.

Romanek, C. S., M. M. Grady, I. P. Wright, D. W. Mittlefehldt, R. A. Socki, C. T. Pillinger, and E. K. Gibson, Jr. (1994), Record of fluid-rock interactions on Mars from the meteorite ALH84001, *Nature*, *372*, 655-657, doi:10.1038/372655a0.

Schultz, P. H., and A. B. Lutz (1988), Polar Wandering of Mars, *Icarus*, *73*, 91-141, doi:10.1016/0019-1035(88)90087-5.

Shearer, C. K., L. A. Leshin, and C. T. Adcock (1999), Olivine in Martian meteorite Allan Hills 84001: Evidence for a high-temperature origin and implications for signs of life, *Meteoritics & Planetary Science*, *34*, 331-339, doi:10.1111/j.1945-5100.1999.tb01343.x.

Sprenke, K. F., and L. L. Baker (2000), Magnetization, paleomagnetic poles, and polar wander on Mars, *Icarus*, *147*, 26-34, doi:10.1006/icar.2000.6439.

Stevenson, D. J. (2001), Mars' core and magnetism, *Nature*, *412*, 214-219, doi:10.1038/35084155.

Swindle, T. D., J. A. Grier, and M. K. Burkland (1995), Noble-Gases in Orthopyroxenite Alh84001 - a Different Kind of Martian Meteorite with an Atmospheric Signature, *Geochim. Cosmochim. Acta*, *59*, 793-801, doi:10.1016/0016-7037(94)00359-T.

Thomas-Keprta, K. L., S. J. Clemett, D. S. McKay, E. K. Gibson, and S. J. Wentworth (2009), Origins of magnetite nanocrystals in Martian meteorite ALH84001, *Geochim. Cosmochim. Acta*, *73*, 6631-6677, doi:10.1016/j.gca.2009.05.064.

Thomas, P., M. Grott, A. Morschhauser, and F. Vervelidou (2018), Paleopole Reconstruction of Martian Magnetic Field Anomalies, *J. Geophys. Res.*, *123*, doi:10.1002/2017JE005511.

Treiman, A. H. (1995), A petrographic history of martian meteorite ALH84001: Two shocks and an ancient age, *Meteoritics*, *30*, 294-302, doi:10.1111/j.1945-5100.1995.tb01127.x.

Treiman, A. H. (1998), The history of Allan Hills 84001 revised: multiple shock events, *Meteorit Planet Sci*, *33*, 753-764, doi:10.1111/j.1945-5100.1998.tb01681.x.

Valley, J. W., J. M. Eiler, C. M. Graham, E. K. Gibson, C. S. Romanek, and E. M. Stolper (1997), Low-Temperature Carbonate Concretions in the Martian Meteorite ALH84001: Evidence from Stable Isotopes and Mineralogy, *Science*, *275*, 1633-1638, doi:10.1126/science.275.5306.1633.

Vervelidou, F., V. Lesur, M. Grott, A. Morschhauser, and R. J. Lillis (2017), Constraining the Date of the Martian Dynamo Shutdown by Means of Crater Magnetization Signatures, *J Geophys Res-Planet*, *122*, 2294-2311, doi:10.1002/2017je005410.

Wadhwa, M., and G. Lugmair (1996), The formation age of carbonates in ALH84001, *Meteoritics & Planetary Science*, *31*, A145.

Weiss, B. P., L. E. Fong, H. Vali, E. A. Lima, and F. J. Baudenbacher (2008), Paleointensity of the ancient Martian magnetic field, *Geophys. Res. Lett.*, *35*, doi:10.1029/2008gl035585.

Weiss, B. P., J. L. Kirschvink, F. J. Baudenbacher, H. Vali, N. T. Peters, F. A. Macdonald, and J. P. Wikswo (2000), A low temperature transfer of ALH84001 from Mars to Earth, *Science*, *290*, 791-795, doi:10.1126/science.290.5492.791.

Weiss, B. P., D. L. Shuster, and S. T. Stewart (2002a), Temperatures on Mars from 40Ar/39Ar thermochronology of ALH84001, *Earth Planet. Sci. Lett.*, *201*, 465-472, doi:10.1016/s0012-821x(02)00729-x.

Weiss, B. P., H. Vali, F. J. Baudenbacher, J. L. Kirschvink, S. T. Stewart, and D. L. Shuster (2002b), Records of an ancient Martian magnetic field in ALH84001, *Earth Planet. Sci. Lett.*, *201*, 449-463, doi:10.1016/S0012-821x(02)00728-8.

Chapter 6

SUMMARY, OUTSTANDING QUESTIONS, AND FUTURE DIRECTIONS

The major results of this thesis have only been possible by combining observations at differing spatial scales and incorporating measurements from a variety of data sources. This approach, from the microscopic to macro-scale, enables new research providing insights into Mars and supports future exploration.

Integrating the results of our studies with other published works about Gale crater we now know that the greater Gale region hosts a predominantly mafic bedrock and contains phyllosilicates of varying compositions (Fe/Mg, Al, Fe-Al smectites) and proportions. The presence of olivine in many of the spectroscopic scenes precludes the detection of felsic material, and so any feldspathic or high-Si lithologies also present in the region must be small and/or intermingling with mafic minerals within the spatial resolution of the CRISM instrument. Although both Gale and Sharp/Knobel craters were fed initially from the same watershed at Herschel crater, key mineralogical differences exist between the adjacent valleys and downstream from Herschel [*Ehlmann and Buz*, 2015]. The inclusion of Al-substituted nontronite within Mt. Sharp's higher sedimentary units further demonstrates a changing aqueous environment in the region's history. Fe/Mg phyllosilicates are alteration products of a mafic bedrock, so precise timing of the Gale floor phyllosilicates is hard to determine, but the geomorphological features surrounding Gale and the active landscape modification observed lead to the interpretation that some portion of the Gale floor materials are sourced from the crater's wall and rim. Lastly, lake related features and potential lake sediments observed outside of the MSL region expand the lake stratigraphy backward in time, to strata older than those that the rover can access. Questions that remain for Gale crater include (1) what is the source for the felsic float rocks observed on the floor of Gale? (2) how did the chemistry of the alteration fluids change as materials were transported from the walls of Gale to the interior lakes? (3) what is the nature of the capping unit overlying the lake sediments? (4) How did the sediment sources around Gale evolve? (5) Over what time interval did lake Gale exist and how many distinctive episodes of the presence of a lake can be identified? Answers to these questions can only be achieved with further high resolution imaging paired with spectroscopy or through additional rovers/landers. While it may not be possible to answer these questions in the near future, ongoing rover observations will continually put our greater-Gale work in context.

A full understanding of the photometric properties of calibration target materials is imperative for proper data analysis and correction of rover data. Through our analysis of the candidate target materials for the Mars-2020 rover we have determined that the photometric properties of the materials are quantifiable and correctable and will be adequate calibration targets. Further work will be necessary for a high resolution model of the scattering properties of the samples. It will also be important to observe how the samples collect dust when on the Martian surface. The products of our study will be direct input into the data analysis pipeline for future multispectral observations from the Mars-2020 mission. As the characterized standards are also the most commonly available commercial color standards, we also expect that the photometric corrections enabled by our work will be useful to other investigators.

Analysis of the magnetization of the ALH84001 carbonates gives constraints both on the formation of the magnetite crystals within the carbonate and the ambient magnetic field at the time of carbonate formation. We know from the Fuller test of NRM that the process by which the carbonates were magnetized was highly efficient (i.e., external forces played a minor role). Because the Fuller test is calibrated for Earth-strength fields we use geophysical modeling to interpret these results. We also find that the magnetic particles within the carbonate are highly interacting which could be because the magnetite crystals were entrained after formation or because the carbonate experienced significant shock fields. The Lowrie-Fuller test shows us that the magnetization within the carbonates is carried primarily by low coercivity grains which is consistent with either a viscous process or a shock process. Combining all of the available test results our analysis indicates the most likely method of magnetization for the ALH84001 carbonates is from a shock process. Shock processes are highly efficient, cause alteration, and primarily effect low coercivity grains. Typically a shock field can be applied in the laboratory and directly compared with the NRM. However, given the microscopic nature of the samples and their necessary sample holders, it would not be possible to conduct this test. An alternative enlightening experiment would be the progressive shock, demagnetization, and rock magnetism analysis of natural siderite samples. This test was not in the realm of our study but would be straightforward and would validate our assumptions about the distribution of magnetic particles within a shocked sample, the size of the particles, and the coercivity range of the resulting magnetization.

A non-random distribution of dipoles in ALH84001 signifies that the meteorite sample is recording a magnetic field, and the distribution of the directions along a great-circle arc (a girdle distribution) argues for at least two primary directional components. If the sample were recording the magnetic field during a true polar wander event the magnetization at various points would be stored in different populations of grains. Because we did not want to destroy the magnetization within our slices of ALH84001 we did not do a paired mineralogical investigation, however, such an investigation could be conducted using an SEM or similar instrument. Separating the magnetization directions based on mineralogy and grain size can possibly give constraints on how quickly the magnetic field was changing relative to the orientation of the sample. A progressive demagnetization of all of the slices would also rule out biases from any secondary components. Lastly, the fitting procedure which currently requires each dipole be fit individually could be improved if a fit of all the dipoles could be conducted at the same time. These three tests could shift the magnetization within ALH84001 from being consistent with TPW to being evidence of TPW.

Consideration of what we know about Mars' magnetic past from geophysical modeling and satellite data provides the framework for interpretation of our magnetic measurements on ALH84001. Without key satellite observations of Mars and constraints placed on the strength of an ancient magnetic field [*Acuna et al.*, 1998; *Stevenson*, 2001], we would either misinterpret or have a limited understanding of our laboratory analyses (specifically the interpretation of the magnetization efficiency and paleointensity results would not be possible). Further, geophysical modeling allows us to contemplate the possibility of phenomena such as true polar wander as an explanation for the distribution of the observed magnetization [*Sprenke et al.*, 2005; *Perron et al.*, 2007; *Milbury et al.*, 2012; *Thomas et al.*, 2018].

Each of the studies presented here has future directions in the continued integration of datasets. As the MSL Curiosity rover mission persists, surely new lithologies will be observed, and our regional work will provide context for these measurements. Studies investigating past and future landing sites would gain insight by expanding their region of interest by an order of magnitude. Laboratory measurements will certainly continue to elucidate remote sensing observations. Lastly, the improvement of magnetic field modeling on Mars, including through hoped for inclusion of a magnetometer on a rover, will significantly aid in understanding the global variability in surface magnetizations.

References

Acuna, M. H., et al. (1998), Magnetic field and plasma observations at Mars: Initial results of the Mars global surveyor mission, *Science*, *279*, 1676-1680, doi:10.1126/science.279.5357.1676.

Ehlmann, B. L., and J. Buz (2015), Mineralogy and fluvial history of the watersheds of Gale, Knobel, and Sharp craters: A regional context for the Mars Science Laboratory Curiosity's exploration, *Geophys. Res. Lett.*, *42*, 264-273, doi:10.1002/2014gl062553.

Milbury, C., G. Schubert, C. A. Raymond, S. E. Smrekar, and B. Langlais (2012), The history of Mars' dynamo as revealed by modeling magnetic anomalies near Tyrrhenus Mons and Syrtis Major, *J Geophys Res-Planet*, *117*, n/a-n/a, doi:Artn E10007
10.1029/2012je004099.

Perron, J. T., J. X. Mitrovica, M. Manga, I. Matsuyama, and M. A. Richards (2007), Evidence for an ancient martian ocean in the topography of deformed shorelines, *Nature*, *447*, 840-843, doi:10.1038/nature05873.

Sprenke, K. F., L. L. Baker, and A. F. Williams (2005), Polar wander on Mars: Evidence in the geoid, *Icarus*, *174*, 486-489, doi:10.1016/j.icarus.2004.11.009.

Stevenson, D. J. (2001), Mars' core and magnetism, *Nature*, *412*, 214-219, doi:10.1038/35084155.

Thomas, P., M. Grott, A. Morschhauser, and F. Vervelidou (2018), Paleopole Reconstruction of Martian Magnetic Field Anomalies, *J. Geophys. Res.*, *123*, doi:10.1002/2017JE005511.